論文 / 著書情報
Article / Book Information

題目(和文)	
Title(English)	Stability improvement of small-molecular organic solar cells
著者(和文)	CaoHuanqi
Author(English)	Huanqi Cao
出典(和文)	学位:博士(工学), 学位授与機関:東京工業大学, 報告番号:甲第9278号, 授与年月日:2013年9月25日, 学位の種別:課程博士, 審査員:石川 謙,森 健彦,ﾊﾞﾊ ﾏｰﾃｨﾝ,松本 英俊,早水 裕平
Citation(English)	Degree:Doctor (Engineering), Conferring organization: Tokyo Institute of Technology, Report number:甲第9278号, Conferred date:2013/9/25, Degree Type:Course doctor, Examiner:,,,,
学位種別(和文)	博士論文
Type(English)	Doctoral Thesis

Stability improvement of small-molecular organic solar cells

Department of Organic and Polymeric Materials

Tokyo Institute of Technology

Cao Huanqi

August 2013

Abstract

The aim of this work is the investigation of stability of small-molecular organic solar cells (OSCs) based on CuPc and C_{60}. We observed various degradation patterns of OSCs under different light irradiation conditions. To explain the divergence among experimental observations, two models were built in which oxygen was considered as the dominating factor of degradation. Based on the degradation study, we designed an aluminum-titanium bilayer cathode to improve the stability of an unencapsulated OSC. Devices using such bilayer cathodes were degradation-free in air in three months. We further studied the stability of bilayer-cathode OSCs with various buffer layers, and finally proposed stabilization mechanisms of the bilayer cathode based on detailed experimental observations. Our findings will hopefully advance the understanding and development of OSCs.

Abbreviations

AFM	atomic force microscope
ALD	atomic layer deposition
AM	air mass
BHJ	bulk heterojunction
C-T	charge-transfer
CVD	chemical vapor deposition
D-A	donor-acceptor
DFM	dynamic force microscope
eLbL	electrical Layer-by-Layer
EQE	external quantum efficiency
ETL	electron transport layer
FEM	finite element method
FF	fill factor
HOMO	highest occupied molecular orbital
HTL	hole transport layer
IQE	internal quantum efficiency
IR	infrared
ISC	inorganic solar cell
I_{SC}	short-circuit current
J_{SC}	short-circuit current density
LB	Langmuir-Blodgett
LUMO	lowest unoccupied molecular orbital
MPP	maximum power point
OFET	organic field effect transistor
OLED	organic light emitting diode
OPV	organic photovoltaic
OSC	organic solar cell
PAL	photoactive layer
Pc	phthalocyanine
PCE	power conversion efficiency
P_{in}	incident power
P_{max}	maximum power
r.t.	room temperature
RH	relative humidity
R_s	series resistance
R_{sh}	shunt resistance
RTD	resistance temperature detector
SEM	scanning electron microscope
SPM	scanning probe microscope
SWNT	single-wall carbon nanotube
THM	time of half maximum PCE
TMP	turbomolecular pump

TOF-SIMS	time of flight-secondary ion mass spectrometry
UV	ultraviolet
V_{OC}	open-circuit voltage
XRD	X-ray diffraction

Contents

Chapter 1. Introduction

We humans are facing many urgent global issues today, most of which are directly related with our activities. The most serious one is the global warming, the major cause of which is generally believed to be the over-exhausted carbon dioxides from the combustion of fossil fuels. Air pollution is another critical issue directly resulted from human activities. The major source of the pollutants is also the combustion of fossil fuels in power plant and vehicles.

Finding the way out of the destructive energy consumption becomes necessary and critical. One promising direction should be the development of renewable-energy sources. Renewable-energy sources, mainly including biomass, hydropower, wind, ocean (tidal) and solar (thermal and photovoltaic, PV) energy, accounted for 16.7% of the global final energy consumption in 2010. [1]

Solar cells grew fast among the renewable-energy sources in recent years. One advantage of solar cells is that they generate electricity directly from the massive solar energy. Depending on the active materials usually of two different semiconductors, solar cells are further divided into inorganic solar cells (ISCs), organic solar cells (OSCs), and some organic-inorganic hybrid solar cells.

The first *p-n* junction ISC with a power conversion efficiency (PCE) of 6% was developed at Bell Laboratories in 1954. [2] More than 600 elemental and compound semiconductors were known by 2007. [3] PCE of element ISCs was improved to 25% for crystalline silicon ones by 2012. [4]

Compound semiconductors include III-V compounds such as GaAs and InSb, and many metal oxides and sulfides such as TiO_x and PbS. Even higher PCE has been achieved for compound ISCs (28.8% for single junction GaAs thin film solar cells in 2012 [4]). Compound ISCs have been predominated in aerospace applications.

Besides the high efficiency, another advantage of ISCs is their durability. The crystalline silicon solar cells merely degrade 0.5% per year on average, [5] thereby sustaining a lifetime of decades of years. However, ISCs have many drawbacks at the same time, including the rigidity of PV panels, the environmental pollution of doping elements, and the high fabrication cost. As the thickness of ISC is usually much thicker than that of OSCs, the purity of the inorganic semiconductors used in ISCs needs to be extremely high. The purification of the composing semiconductors consumes tremendous energy, which inevitably increases the production cost and thereby limits wide applications of inorganic solar cells.

OSCs become increasingly attractive in recent years, as they can be fabricated from various organic compounds with modifiable structures. Besides, OSCs have other advantages, like the flexibility, the high PCE under low light irradiation, [6] and the

promising application of see-through power-generation windows, etc. However, the low stability of OSCs decreases the value (yield over cost) of an OSC system as its energy production is currently largely limited by its low durability. This thesis focuses on the degradation dynamics and how to improve the stability of OSCs.

1.1. Photovoltaics

1.1.1. Solar energy

The earth receives a total amount of about 8.9×10^{16} W on the surface from the sun. This is thousands of times higher than the average total power consumption of the human world, 1.6×10^{13} W in 2010. Most of the above mentioned renewable-energy sources are virtually converted from the light radiation from the sun.

People from the ancient have already known how to passively receive the solar thermal energy by orienting their dwellings. Since the 20th century, several active ways to harvest the solar energy have emerged, including the solar water heating or cooling, concentrated solar power, and solar cells. The former two use the thermal effect of sunlight, while the last one outputs electricity directly from the solar light irradiated on semiconductors.

Sunlight propagating in the atmosphere of the earth is attenuated by scattering and absorption. On the surface of the earth, the angle between sunlight and the surface normal determines the received light intensity. Air mass (AM) is used to depict the tilting-angle dependent intensity of solar light radiated on the earth surface, given by

$$\mathrm{AM} = 1/\cos\theta \qquad 1\text{-}1$$

where θ is the zenith angle (the angle of incident light from overhead)

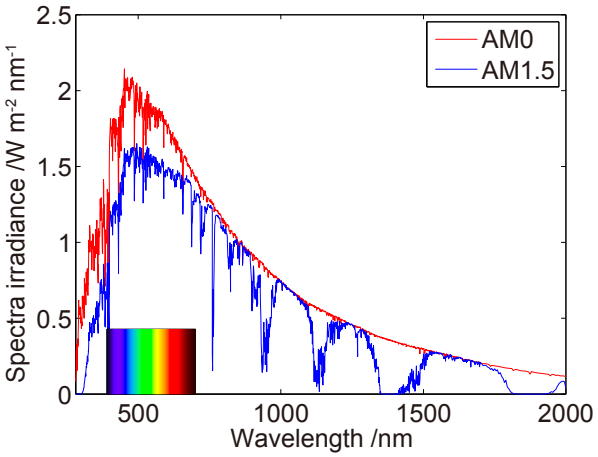

Figure 1–1 Spectral distribution of sunlight.[7] Shown are the cases of AM0 and AM1.5 radiation. Inset shows the visible region (390-700 nm) of human eyes.

The standard spectra for testing PV devices is AM = 1.5 (often noted as AM1.5), corresponding to $\theta = 48.2°$. The total irradiance of AM1.5 is approximately 1000 W cm^{-2}. Both AM0 (solar spectrum outside the atmosphere) and AM1.5 are plotted in Figure 1–1. Solar cells mainly harvest the visible and near-infrared regions.

1.1.2. Photoelectric effect

When light encounters with bulk matter, it might be either scattered, or absorbed if the energy accords with some gap between two different energy levels of electron in the irradiated matter. Along with the absorption of light, the outermost-shell electron absorbs the energy of light, and possibly overcomes the Coulomb attraction of the surrounding nucleuses and escapes from the surface. This phenomenon is called the photoelectric effect.

The maximum kinetic energy of the emitted electrons is linear with the frequency of the incident light. This dependence not only evidences the quantum nature of light, but also provides a method to measure the energy levels of occupied electronic states as well as the Fermi level, E_F. Each quantity that can be absorbed once is a photon, which has both energy and momentum, similarly as other free particles. The maximum kinetic energy of the emitted electron E_k from a metal surface is linear to the frequency of the incident photon υ:

$$E_k = h\nu - \varphi \qquad \text{1-2}$$

where h is the Planck constant, ν the frequency of the incident photon, and φ the work function of the metal that is defined as the energy difference between the vacuum level and the Fermi level. On the surface of a semiconductor, φ in Equation 1-2 is replaced with the topmost valence energy E_v.

Electrons in a crystal automatically fill energy bands that are formed by the degenerated atomic orbitals. For inorganic materials, the highest occupied band at $T = 0\mathrm{K}$ is called a valence band, and the lowest unoccupied band at $T = 0\mathrm{K}$ is called a conduction band. At $T \neq 0\mathrm{K}$, some valence electrons are thermally excited to the conduction band.

In metals, the statistics of the valence electrons are usually treated with a free-electron gas model. The possibility of finding an electron at an energy level E follows Fermi–Dirac distribution function

$$f(E) = \frac{1}{e^{(E-\mu)/kT} - 1} \qquad \text{1-3}$$

where μ is a temperature-dependent value called (electro) chemical potential, and k the Boltzmann constant. The Fermi level (Fermi energy) is then defined by $E_F \equiv \mu_{(T=0)}$, i.e. the energy of the topmost filled orbital at absolute zero. [8] In semiconductor literature, μ and E_F are usually not distinguished. In this case, E_F refers to the energy level at which one have half a chance to find an electron, and is also called electro-

chemical potential. [9] Without applied bias, E_F depends only on the electron density n in a crystal:

$$E_F = \frac{\hbar^2 {k_F}^2}{2m},\ k_F = (3\pi^2 n)^{1/3} \qquad \text{1-4}$$

where the reduced Planck constant $\hbar = h/(2\pi)$, m the mass of an electron, k_F the Fermi wavevector. The electron density n is generally in an order of 10^{29} m^{-3}, and accordingly E_F is several electron volts. [8] In semiconductors, however, the electron and hole populations will be increased under light irradiation. Therefore, the quasi-Fermi levels, E_p and E_n, are used in Equation 1-3, to calculate the population of electrons and holes, respectively.

1.1.3. Semiconductor

According to whether there is a partly filled energy band at $T = 0\mathrm{K}$, a crystal is categorized as either a metal (including semimetal) or an insulator. When there is at least one partly filled valence band, i.e. the uppermost valence band overlaps with the lowest conduction band, or in a particular case, the lowest conduction and uppermost valence band 'touch' each other but not overlap, we have a metal (or semimetal). When electrons just fill the valence band, we have an insulator. [3, 10]

For an insulator (including semiconductor), there is an energy gap between the conduction band edge E_c, and the valence band edge E_v, where the Bloch function solution $\psi_{\mathbf{k}}(\mathbf{r}) = e^{i\mathbf{k}\cdot\mathbf{r}} u_{\mathbf{k}}(\mathbf{r})$ of wave equations in the periodic crystal lattice[1] does not exist. [8] The gap forms a forbidden gap of electron states, and is denoted by E_g. This energy gap determines not only the absorption edge of light, but also the electric conductivity. If $4\mathrm{eV} \geq E_g > 0$, the crystal is normally a semiconductor. If $E_g > 4\mathrm{eV}$, the crystal is normally an insulator.

For organic semiconductors, HOMO and LUMO (highest-occupied/lowest-unoccupied molecular orbitals, respectively) are used to describe the electronic properties of the materials. The interaction between neighboring molecules in organic semiconductors is the van der Waals' force, which is weaker than the valence bonding in inorganic semiconductors. Accordingly, HOMO and LUMO are localized on each discrete molecule. There exists an energy gap between the HOMO and LUMO, which leads to the absorption of light. This energy gap decreases with the increase of length of a π-conjugated molecule. This energy gap also depends on the molecular stacking pattern. [11]

A semiconductor has an electric resistivity at room temperature within the range of 10^{-6} to $10^{12}\ \Omega \cdot \mathrm{cm}$ (not strictly). The electric conductivity of a semiconductor includes both intrinsic and extrinsic conductivity. A pure semiconductor without any defect has only intrinsic conductivity, which is exponentially dependent on $-E_g/(2kT)$. A bulk

[1] This requires $u_{\mathbf{k}}(\mathbf{r}) = u_{\mathbf{k}}(\mathbf{r} + \mathbf{R})$. Here $\mathbf{R}$ is a translation vector of the lattice.

semiconductor always contains doping impurities and lattice defects, both of which contribute to the extrinsic conductivity.

Devices based on semiconductors include transistors, light-emitting diodes (LED) and solar cells, etc. Both LED and solar cells involve the separation and recombination of excited charges.

1.1.4. Photovoltaic

Photovoltaic means the method converting light into electric current using semiconductors. During the absorption of light in a semiconductor, the optical transition of electrons can be either direct or indirect, depending on whether the global E_{v} and the global E_{c} occur at the same point of the first Brillouin zone in a reduced E-$\boldsymbol{k}$ scheme. The direct transition is accomplished merely by the absorption (or emission) of a photon, while the indirect transition involves not only a photon, but also a thermal phonon for momentum conservation.

Electrons preferentially fill the lower energy levels in a crystal. Once a valence electron is excited to the conduction band, it leaves an empty state which can be filled by a neighboring valence electron. This empty state can be well described as a positively-charged 'defected-electron' hole. The movement of the holes in the valence band, and the movement of the electrons in the conduction band contribute to the electric conductivity of a semiconductor. A donor-doped semiconductor in which the electron conduction is dominant is an n-type semiconductor (acceptor), and oppositely a p-type semiconductor (donor).

A photo-excited electron is attracted by the geminate hole in a solid, forming an exciton, which lowers the binding energy of the electron and hole. Depending on the material in which an exciton is formed, the exciton can be categorized into Wannier, Frenkel, and charge-transfer (C-T) exciton. The Wannier exciton exists in inorganic semiconductors with relatively large dielectric constants ε and relatively light effective exciton masses. The diameter of a Wannier exciton is usually several nanometers. The binding energy between opposite charges in a Wannier exciton (exciton Rydberg energy) is only 1—100 meV. Therefore, the photo-excited charges and holes in an inorganic semiconductor can be thermally dissociated. [3]

On the contrary, the Frenkel exciton has a relatively small radius and mainly exists in organic semiconductors where the dielectric constant ε is relatively small, and the effective mass of an exciton is relatively heavy due to a small electronic overlap between neighboring molecules. Consequently, the excited electron and hole in organic semiconductors are usually confined in one molecule, and transported together in the bulk. The C-T exciton also mainly exists in organic semiconductors, in which the opposite carriers reside in adjacent molecules. Opposite charges in C-T excitons are also strongly

bonded by the Coulomb force.

Excitons are prone to being annihilated by recombination. The process that an excited electron combines with a hole in a semiconductor is called recombination. The photo-excited carriers are expected to do work before they recombine with opposite carriers. During the recombination, the energy of an excited electron is released in the form of either a photon (luminescence) or a phonon (heat, either Auger or trap-induced relaxation). Specific impurities in semiconductors can exchange charge carriers with both the conduction and valence bands. The trap-induced recombination is significant when the energy level of the recombination center locates at the middle of the forbidden gap. In inorganic semiconductors, atoms forming recombination centers are often those from the same column of the periodic table as the one they substitute. [3]

Excitons generated in organic solar cells need to be dissociated to generate a photo voltage. One common way of dissociating these excitons is to create a D-A heterojunction interface with a donor (D) and an acceptor (A). After arriving at the D-A interface, one type of charge in an exciton will be transferred from D (or A) to A (or D), forming an interfacial C-T exciton, as a result of the selective transport of charges in D and A. Opposite charges in the interfacial C-T exciton are still tightly bonded by a Coulombic force.

Two ways may facilitate the dissociation of the interfacial C-T excitons. One way is to form an energy level cascade which mimics the situations of the photo-synthesis in plants. [12] Another way involves the absorption of IR light by the excited molecules. [13] The latter was proposed by Bakulin et al. with a finding that the infrared light promotes the delocalization of charges in interfacial C-T excitons, and accordingly enhances the photocurrent dramatically.

1.1.5. p-n junction diode

Although working principles of ISCs and OSCs are different from a quantum perspective, theories and concepts developed previously in ISCs have already been widely used to interpret observations in OSCs. To keep consistent with literature, we do not distinguish them in the next sections.

The concentrations of electrons and holes in a semiconductor are denoted by n and p, respectively. In thermal equilibrium, the mass-action law reads $np = {n_i}^2$. Here n_i is an intrinsic parameter of a semiconductor, given by ${n_i}^2 = N_{\mathrm{C}} N_{\mathrm{V}} \exp(-E_g/kT)$ where N_{C} and N_{V} are the effective density of states in the conduction band and valence band, respectively. It states that for a non-degenerate semiconductor, the product of concentrations of electrons and holes are independent of dopants, or Fermi level. In an n-type semiconductor, the concentration of holes will be much reduced due to the abundance of electrons. As a consequence, electrons, less attracted by holes, will find it easy to diffuse in the *n*-type semiconductor, and vice versa.

At the interface, holes preferentially diffuse into the p-type side, and electrons into the *n*-type side. An interfacial C-T exciton is then formed, which with the help of an infrared photon can overcome the trapping effect of the sequentially formed polaron. [13] The separated charge carriers (or polarons in polymers) continue to diffuse towards the connected electrodes and do work if the circuit is closed. This is the principle of most modern OPV devices.

Shockley equation of the current-voltage characteristic of an illuminated *p-n* diode reads

$$I = I_0(e^{qV/\mathrm{n}kT} - 1) - I_{\mathrm{ph}} \qquad 1\text{-}5$$

where

I is the current across a diode in the dark,

I_0 the reverse (bias) saturated (recombination) current, which is a temperature-dependent parameter,

V the voltage across the diode,

k the Boltzmann constant,

T the absolute temperature of the p–n junction,

q the magnitude of charge on an electron,

n the ideal factor, typically 1—2 for ISCs, and 2—3 for typical OSCs,

I_{ph} the photo-current.

The first term on the right of Equation 1-5 states the dark current through a diode in the dark (I_D). The second term indicates that the light illumination merely downshifts the rectifying current-voltage (*I-V*) curve to the fourth quadrant in a linear Cartesian coordinate, as illustrated in Figure 1–2(a). The current is sometimes plotted in a logarithmic scale to show a wide range of current, as shown in Figure 1–2(b).

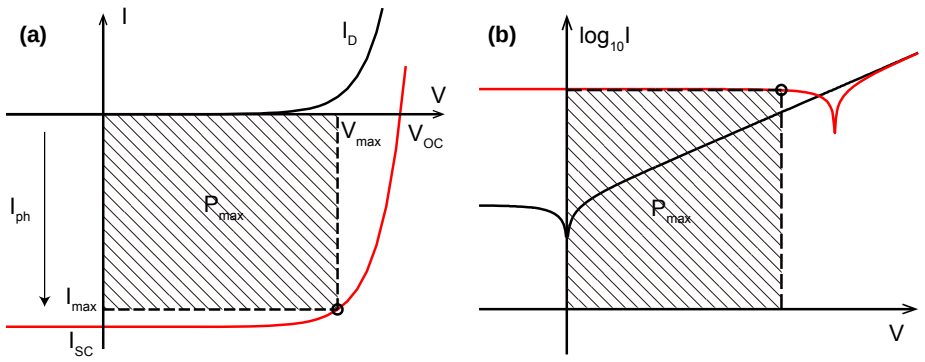

Figure 1–2 Illuminated current-voltage curves of an ideal diode with $n = 1$: (a) with respect to a linear current axis, and (b) with respect to a logarithmic current axis.

1.1.6. Photocurrent-voltage curve

Light-induced electric current (I_{ph}) generated in a solar cell may be shunted not only by the recombination inside the semiconductors (I_0), but also by the leakage current

through shorted connections between electrodes (I_{sh}). The ideal I_{sh} is zero when the shunt resistance R_{sh} (also known as parallel resistance noted by R_p) is infinite. Another parasitic resistance in a solar cell is the series resistance (R_s), originating from the resistance of bulk semiconductors and connections of electrodes. R_s should ideally be zero. Too high R_s or too low R_{sh} will cause the failure of a solar cell. A widely used one-diode equivalent circuit of an irradiated solar cell, including these resistances is shown in Figure 1–3. [14]

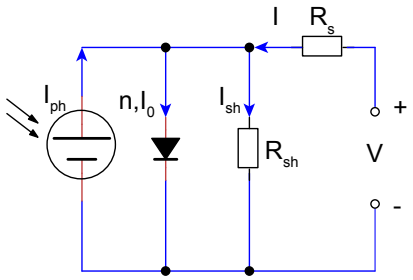

Figure 1–3 Equivalent circuit of a single-diode solar cell under light irradiation.

A generalized Shockley equation depicting the photocurrent in Figure 1–3 reads

$$I = I_0 \left[\exp\left(\frac{q(V - IR_s)}{nkT} \right) - 1 \right] + \frac{V - IR_s}{R_{sh}} - I_{ph} \qquad 1\text{-}6$$

where the parameters are defined either in Equation 1-5 or in Figure 1–3. This is a transcendental equation, and has an analytic solution for I as following

$$I = \frac{nk_BT}{qR_s} W\left[\frac{qR_sI_0R_{sh}}{(R_s + R_{sh})nk_BT} \exp\left(\frac{R_{sh}q(R_sI_{ph} + R_sI_0 + V)}{nk_BT(R_s + R_{sh})} \right) \right] + \frac{V}{R_s} - \frac{R_{sh}(R_sI_{ph} + R_sI_0 + V)}{R_s(R_{sh} + R_s)} \qquad 1\text{-}7$$

where the Lambert W function is the solution of $W(x)\exp[W(x)] = x$. [15, 16]

The short-circuit current (I_{SC}), defined as the current at $V = 0$, corresponds to the intersection of the *I-V* curve with the current-axis in Figure 1–2(a). Following Equation 1-6, the ideal I_{SC} equals $-I_{ph}$, which is proportional to the photon flux within the absorbance range. I_{SC} is also determined by other factors like R_s of the circuit which is mainly decided by electrode contacts and the doping levels of photoactive layers (PALs). The short-circuit current density (J_{SC}) that is I_{SC} on a unit area, is more often used.

The open-circuit voltage (V_{OC}), defined as the voltage at $I = 0$, corresponds to the intersection of the *I-V* curve with the voltage-axis in Figure 1–2(a). V_{OC} depends on the quality of electrodes. A small R_{sh} (e.g., <1000 Ω), caused by the shortage between electrodes, will significantly decrease V_{OC}. Other factors determining V_{OC} of organic solar cells are discussed in Section 1.2.5.

The maximum power P_{max} corresponds to the maximum area of the square in the fourth quadrant in Figure 1–2(a). After obtaining the value of P_{max}, the fill factor *FF* is commonly

calculated according to Equation 1-8. Another rarely used definition of *FF* may be found in literature. [17] *FF* describes the deflation of the *I-V* curve in the fourth quadrant.

$$P_{\max} = V_{\mathrm{OC}} \times I_{\mathrm{SC}} \times FF \qquad 1\text{-}8$$

Factors influencing V_{OC}, I_{SC}, or *FF* will influence P_{max}. The PCE of a solar cell is defined by the ratio of P_{max} to the total power of the incident light beam P_{in}: $\mathrm{PCE} = P_{\max}/P_{\mathrm{in}}$.

The above mentioned parameters n, R_{sh}, R_s I_0 and I_{ph} may be extracted by fitting an *I-V* curve obtained in the dark. [18] However, the conductivity of a semiconductor will be influenced by light irradiation, which makes it suggestive to extract these parameters from *I-V* curves obtained under light irradiation. Some parameter extraction approaches often result in unexpected or unreasonable parameters. Therefore, it is necessary to discuss the parameter extraction method before these parameters are discussed.

The method introduced by Ishibashi et al. is one of the simplest methods. It needs only one single *I-V* curve obtained under illumination to extract all the necessary parameters. [19] In this method, a new term Δ is defined in Equation 1-10 and is assumed to be much less than unity. As this assumption is the prerequisite of this extraction method, we shall call this method the *Delta approximation method* hereinafter. The *Delta approximation method* is described in the following.

First, write down the differential form of Equation 1-6 as Equation 1-9.

$$\frac{dV}{dI} = \frac{nk_BT/q}{I_{\mathrm{ph}} + I_0 + I - (V - R_{\mathrm{s}}I - nk_BT/q)/R_{\mathrm{sh}}} + R_{\mathrm{s}} \qquad 1\text{-}9$$

The Delta assumption is

$$\Delta \equiv \exp\left\{-\frac{q(V_{\mathrm{oc}} - R_{\mathrm{s}}I_{\mathrm{sc}})}{nk_BT}\right\} \ll 1 \qquad 1\text{-}10$$

Table 1 shows the value of Δ calculated with different R_sA (A is the active area of the device). Other parameters are, $\mathrm{n} = 3, T = 298\ \mathrm{K}, V_{OC} = 0.5\ \mathrm{V}$ and $J_{SC} = 4\ \mathrm{mA\ cm^{-2}}$. The results indicate that the *Delta approximation method* could hold for R_sA < 50 Ω cm^2.

Table 1 Calculated values of Delta as a function of R_sA.

R_sA / Ω cm^2	0.1	1	10	50	100	200
Δ	0.0016	0.0017	0.0027	0.021	0.28	48

After obtaining an *I-V* curve from a solar cell under light illumination, I_{SC} and V_{OC} are calculated according to the definitions. With assumption 1-10, I_0 and I_{ph} in Equation 1-6 and Equation 1-9 can then be expressed in terms of V_{oc}, I_{sc}, n, R_s and R_{sh} as

$$I_0 \approx (I_{\mathrm{SC}} + \frac{R_{\mathrm{s}}I_{\mathrm{SC}} - V_{\mathrm{OC}}}{R_{\mathrm{sh}}}) \exp(\frac{-qV_{\mathrm{OC}}}{nk_BT}) \qquad 1\text{-}11$$

$$I_{\mathrm{ph}} + I_0 \approx I_{\mathrm{SC}}(1 + R_{\mathrm{s}}/R_{\mathrm{sh}}) \qquad \text{1-12}$$

At this step, only three unknowns R_s, R_{sh} and n are necessitated for describing the experimental *I-V* curve, and Equation 1-9 becomes

$$\frac{dV}{dI} \approx \frac{nk_BT/q}{I_{\mathrm{SC}} + I - V/R_{\mathrm{sh}} + nk_BT/(qR_{\mathrm{sh}}) + (I + I_{\mathrm{SC}})R_{\mathrm{s}}/R_{\mathrm{sh}}} + R_{\mathrm{s}} \qquad \text{1-13}$$

Assumption 1-14 is further used for estimating the initial values of n, R_s and R_{sh}.

$$R_{\mathrm{s}}/R_{\mathrm{sh}} \ll 1 \qquad \text{1-14}$$

It is then feasible to estimate the initial value of R_{sh} using Approximation 1-15. R_{sh} are usually estimated by the dynamic shunt resistance R_{sho} [20], which corresponds to the slope of the *I-V* curve at the short circuit condition.

$$R_{\mathrm{sho}} = \left.\frac{dV}{dI}\right|_{I=I_{\mathrm{SC}},V=0} \approx R_{\mathrm{sh}} + R_{\mathrm{s}} \approx R_{\mathrm{sh}} \qquad \text{1-15}$$

The other two unknowns n and R_s are correlated and can be found by fitting the experimental data in the V_{oc} region iteratively using a trail-and-error approach. [19]

The *Delta approximation method* was further advanced by Zhang et al., [14] who combined this method with the Lambert W function fitting method which had been previously used to determine the ideal factor *n*. [20, 21] All parameters can also be estimated from one single *I-V* curve, by fitting the experimental curve with the analytic solution of *I* given in Equation 1-7. The initial value of R_{sh} is also assumed to be equal to R_{sho}. The only difference is that, they use approximation 1-16 to estimate the initial value of *n* and R_s.

$$\left.\frac{dV}{dI}\right|_{V=V_{\mathrm{OC}},I=0} \approx \mathrm{n}\left[\frac{k_BT/q}{I_{\mathrm{SC}} + I - V/R_{\mathrm{sh}}}\right] + R_{\mathrm{s}} \qquad \text{1-16}$$

Comparing approximation 1-13 with approximation 1-16, two terms in the denominator on the right of approximation 1-13 are omitted. It can be shown that this only leads to a less than 10% erroneousness in the denominator for $R_{sh}A$ > 390 Ω cm^2 and R_sA < 10 Ω cm^2. In many cases, these conditions are satisfied. Approximation 1-16 is then satisfied and as a result, the slope of a plot of *dV/dI* as a function of $k_BT/q/(I_{\mathrm{SC}} + I - V/R_{\mathrm{sh}})$ at $V \rightarrow V_{oc}$ yields the ideal factor n, and the intercept yields the series resistance R_s. These two estimated values are then used as the initial values of *n* and R_s for further fittings. For simplicity, the approximated expressions of I_0 and I_{ph} given in 1-11 and 1-12 are used to simplify Equation 1-7 and Equation 1-9. A non-linear least square fitting is finally executed to optimize the estimated n and R_s.

We employed the *Delta approximation method* to extract parameters from experimental results. Instead of using the approximated solution of *I*, we used the accurate solution of *I* with I_0 and I_{ph} not approximated, to extract parameters by fitting an *I-V* curve obtained under illumination. The same method has probably already been used in literature. [15]

The above introduced *Delta approximation method* is simple and effective. For an *I-V* curve with a high *FF*, this method works well (Figure 1–4). However, the application of this method to a device with a low *FF* demands a lot of caution. The reason is that a low *FF* invalidates both the assumption 1-10 and assumpation 1-14. In this case, there exists an inflection point at 0 < V < V_{OC} where the second derivative d^2I/dV^2 becomes negative. Therefore, the reliability of extracted parameters by this method from a device strongly depends on *FF*.

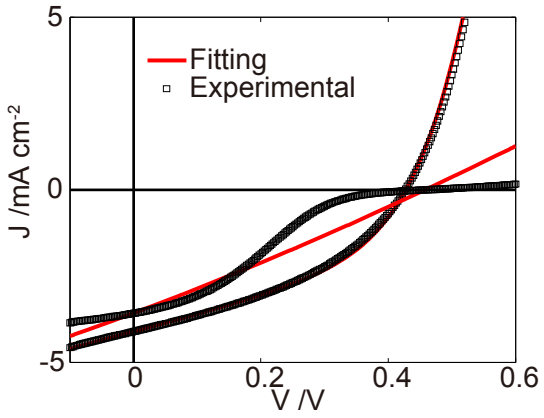

Figure 1–4 Fittings of two experimental curves with the method explained in the text. The well fitted curve was tested from a fresh Ti-Al cell, while the S-shape curve was recorded after exposing the cell in air for one day.

The origin of such an S-shape curve is perhaps the charge accumulation at the electrode interfaces. [22] The accumulated charges deviate the solar cell from a standard diode device and accordingly, Equation 1-6, which is derived from a single diode, is no longer valid.

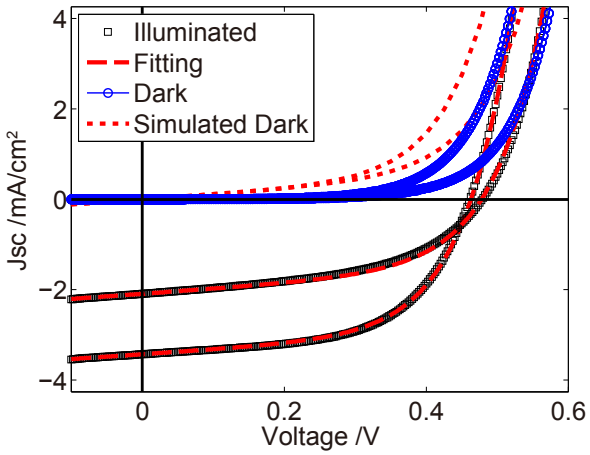

Figure 1–5 Comparison of calculated (dotted) and measured (circled) dark current density – voltage curves with parameters n, R_s and R_{sh} extracted from the related illuminated curves (squared). The fitting curves (dashed) prove the high accuracy of the Delta approximation method.

Figure 1–5 shows another limitation of this extraction method, which is related with the light intensity. The calculated dark *I*-*V* curve, according to Equation 1-6 ($I_{\mathrm{ph}} = 0$), does not agree with the measured dark *I*-*V* curve. Zhang et al. have shown that the light intensity profoundly changes the fitted parameters. [14] Another possible explanation may be related with the voltage-dependent I_{ph}. [23] Therefore, parameters extracted from an illuminated *I*-*V* curve cannot directly be used to predict the *I*-*V* characteristic of a device in the dark. However, the extracted parameters from different *J*-*V* curves obtained under the same light intensity can be compared between devices.

1.2. Organic solar cells

1.2.1. Brief history

OSCs discussed hereinafter specifically refer to the photovoltaic devices with both donor and acceptor materials comprised by organic materials. The dye-sensitized solar cells (DSSCs, also called photochemical cells [24]) are not discussed. This is because electron acceptors in DSSCs are usually inorganic semiconductors like ZnO or TiO_2, and different theories have been built. Other organic-inorganic hybrid *p*-*n* heterojunction solar cells are also not discussed for the same reason.

Brief history of OSCs was summarized by Chamberlain in 1983 [25], by Spanggaard and Krebs in 2004 [26], and recently by Mishra and Bäuerle in 2012 [27].

The study of photovoltaic effect of organic semiconductors began in the 1950s. [28] The first *p*-*n* heterojunction organic solar cell could be traced to a report by Meier and Haus in 1960. [29] A *p*-*n* heterojunction OSC giving a PCE of 0.05% under a 75 mW cm^{-2} Xe lamp was reported by Kudo and Moriizumi in 1981. [30] A milestone efficiency of 0.95% for heterojunction OSCs consisting of CuPc and a perylene derivative under simulated AM2 was patented in 1979 and reported in 1986 by Tang. [31]

The early study of OSCs did not draw much attention before the participation of fullerene. The finding of the photovoltaic properties of fullerene C_{60} in the 1980s accelerates the developments of OSCs with efficiencies higher than 1% since the 1990s. Another allotrope of carbon cluster fullerene C_{70} has drawn even more attention as it has stronger absorption in the visible range compared to C_{60}. OSCs with and without fullerene have gone a similar way: initially thermally deposited small-molecular planar OSCs, and then polymer-blending OSCs.

1.2.2. Common materials

A conventional OSC comprises six layers stacked on the surface of a supporting substrate which is normally a piece of glass or transparent plastic. These six layers include a

transparent conductive anode (normally indium-tin-oxide, ITO), a hole-transport layer (HTL), an electron donor, an electron acceptor, an electron-transport layer (ETL), and a metal cathode (normally Al or Ag). Sometimes an extra encapsulation film is finally applied on the top of the fabricated device to protect the device from a rapid decay in air. In some cases, PALs (donor and acceptor) are doped or modified with functional dopants. A review over 211 different organic semiconductors used in OSCs has been reviewed. [27]

The determination of which electrode acts as the anode (or cathode) in a *p-n* junction device depends on the type of the adjacent buffer layer. A buffer layer may have at least two functions on the nearby electrode. First, the buffer layer may act like a heavily doped large-bandgap semiconductor, and thereby eliminating a rectifying junction between the PAL and the adjacent electrode. In this case, if the buffer layer is an ETL, the adjacent electrode acts as the cathode. An electrode acts as the anode if the adjacent buffer layer is an HTL. Second, an ultrathin layer which contains atoms from the halogen or nitrogen groups will substantially change the surface work function of the nearby electrode by the formation of a surface dipole moment. [32, 33]

For the anode, high work function conductors are commonly used. ITO, with a work function of 4.7 eV, is often used as the anode of OSCs in laboratory researches. However, due to the rigidity of the ITO as well as the scarcity of indium, a variety of candidates of the ITO anode have been reported in recent years. For example, Ag (or Au)-grid PEDOT:PSS or even only PEDOT:PSS [34] has been used as the anodes (including HTLs) to fabricate inverted-structure OSCs. Another attractive candidate is a transparent MoO_x (40nm)/Ag (13 nm)/MoO_x (5nm) sandwich structure. This anode has been used to fabricate organic PV sub-modules, which demand a low resistant electrode to reduce the drop of *FF* with the increase of active area. [35] Another similar anode made up of MoO_3 (5 nm)/Ag (< 30 nm) has been used to fabricate the so-called see-through power-generation window, which might see possible applications in decoration. [36] Other novel anodes like the single-wall carbon nanotube (SWNT) [37], the chemical vapor deposited (CVD) graphene [15] have also been used as the anodes of OSCs in literature.

For the HTL, PEDOT:PSS and MoO_3 are commonly used. PEDOT:PSS composes of a polyelectrolyte sodium poly(styrene sulfonate) (Na^+PSS^-) and a transparent conductive polymer Poly(3,4-ethylenedioxythiophene) (PEDOT). PEDOT is featured by its electrical and thermal stability, but it agglomerates readily. Na^+PSS^- can disperse PEDOT in an aqueous solution or on a substrate. The electric conductivity of a PEDOT:PSS film can be dramatically improved by adding polar additives or by a hot-rinsing treatment of spin-coated films with polar solvents. [38] However, when PEDOT:PSS is used as the HTL, the improvement of its electric conductivity rarely contributes to the performance of OSCs. [39] As pointed out by Forrest et al., the big series resistance of a PEDOT:PSS device does not originate from the bulk resistance of the PEDOT:PSS layer. MoO_3, having a p-type doping characteristic, [40] has also been used in organic solar cells as an HTL.

Common donors used in polymeric BHJ-OSCs include poly[(3-hexylthiophene)-2,5-diyl]

(P3HT), or poly(4,8-di(2-ethylhexyloxyl)benzo[1,2-b:4,5-b']dithiophene-2,6-diyl)-alt-(5-octylthieno[3,4-c]pyrrole-4,6-dione-1,3-diyl) (PBDTTPD). The latter has a low bandgap, thereby giving a high V_{OC} and PCE. The most commonly used small-molecular donors in OSCs are metal phthalocyanines (MPc). The molecular structure of copper phthalocyanine (CuPc) is shown on the left of Figure 1–6.

Most Pcs have polymorphism, leading to different molecular stacking patterns on the surface of a substrate. For example, CuPc has at least eight different crystalline forms while α-CuPc and β-CuPc are two common forms. CuPc precipitated from concentrated sulfuric acid is usually α-CuPc, the red shade blue pigment, while CuPc sublimated in vacuum is usually β-CuPc, the green shade and more stable pigment. Pcs have two strong absorption bands in the visible spectra. The bluish color comes from a strong absorption at 650 nm, which is called a Q-band, while the other absorption at 370 nm is called a B-band (also called a Soret-band). The absorption peaks of the Q-band are usually used to tell the form the Pc. As a rule of thumb, the β-form Pc has a stronger absorption at the longer wavelength side, while the α-form has a stronger absorption at the shorter wavelength side. Molecular orbital theory shows that both the Q band and B band originate from the electron transition from the center to the periphery of the molecule (π-π* transition). Substitution of the peripheral hydrogen atoms with electron-withdrawing elements like F will lower these bands.

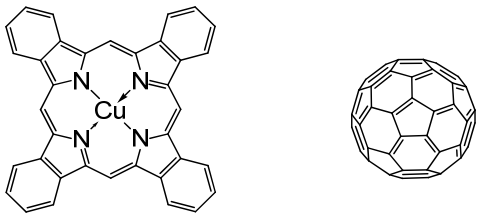

Figure 1–6 Molecular structure of copper phthalocyanine CuPc on the left, and fullerene C_{60} (side view) on the right.

For the acceptor, fullerene C_{60}, C_{70} and their derivatives are most commonly used. The molecular structure of C_{60} is shown on the right of Figure 1–6. Fullerene has a high electron affinity, and is prone to forming charge-transfer excitons with donor molecules under light irradiation. Its molecular frame is very stable under normal conditions. One special feature of this cage-shape molecule is that it rotates freely in three dimensions at room temperature. [41] Fullerene undergoes a phase transition (face-centered cubic at room temperature to simple cubic below 260 K) during which the swift rotation of the molecular cages in two directions becomes frozen.

For the ETL, BCP and LiF are two common choices. Although the ETL layer is usually very thin, it essentially influences the stability of fabricated devices. Aluminum is very sensitive to oxygen and water at room temperature. However, the existence of fullerene on the surface of aluminum will significantly passivate the surface of the aluminum due to the hydrophobic nature of fullerene, and therefore, the resistance of aluminum cathode to water vapor is dramatically improved. [42]

For the cathode, aluminum and silver are two common choices. Two advantages of aluminum are the low weight and the good match of its work function with the electron affinity of fullerene.

An ultrathin functional metal layer is sometimes used to reduce the work function of the cathode. For example, samarium (1 nm) and aluminum (80 nm) bilayer cathodes are sometimes used as the cathode. [43] An ultrathin layer (1 nm) of lithium fluoride (LiF) can reduce the work function of aluminum through an interfacial reaction between aluminum and lithium fluoride. [44] One effect of the active metals on the fullerene is perhaps the doping of fullerene during which the metals improve the electric conductivity of fullerene at a low doping level. It notes that this doping will be dedoped by air. [45]

For the encapsulation materials, glass plates with UV curing epoxy resins are the most common and effective method. [46] Polymeric like PDMS plates with a high transparency in the visible spectra, has also been used to encapsulate OSCs. [47]

1.2.3. Thin-film fabrication methods

Vacuum deposition and solution coating are two main fabrication methods of OSCs. The former includes thermal evaporation, chemical vapor deposition, radio frequency sputtering and electron beam sputtering, etc. By controlling the deposition speed and substrate temperature, etc, the vacuum methods are able to control the morphology and even the crystalline orientation of the deposited films. Therefore, the vacuum deposition gives a high repeatability, which reflects the high reliability of these methods. Nevertheless, the sophisticated vacuum equipment will no doubt increase the cost of fabrication.

The solution processes used in the research of OSCs include spin-coating, Langmuir-Blodgett (LB), sol-gel, chemical self-assembly, electrical Layer-by-Layer (eLbL) assembly, stamp-transfer, inkjet-printing, and roll-to-roll processing, etc. [48] Schmidt-Mende et al. use self-assembly discotic liquid crystals to fabricate BHJ-OSCs. [49] Krebs et al. use all aqueous media to print OSCs including the anode. They use ITO as the cathode, and other materials either being dissolved or dispersed in water-contained media, to fabricate OSCs. The introduction of ether groups onto both active materials facilitates the water solubility as well as the removal of the side chains during heat treatments. [50]

1.2.4. Three types of organic solar cells

1.2.4.1. Schottky-junction organic solar cells

As mentioned above, a Schottky junction in a metal-semiconductor-metal structure rectifies the photocurrent. Therefore, a monolayer OSC is capable of converting light illumination into the electric current. However, PCE of a monolayer OSC is relatively low,

as the separation of excitons occurs merely at the interface of the electrode.
A PCE of 0.7% under 78 mW cm^{-2} light illumination area in a Schottky-junction OSC with a metal-oxide-organic semiconductor-metal structure: Al/Al_2O_3/merocyanine dye/Ag was reported by Morel et al. in 1978. [51] The significance of forming an oxide layer in the junction was also emphasized in their report.

1.2.4.2. Planar heterojunction organic solar cells

Most organic solar cells employ D-A heterojunction structures to separate opposite charges in excitons. Small-molecular solar cells offer greater flexibility in the device stack over polymer solar cells due to the easier deposition of multiple layers. [52]

Many small-molecular organic semiconductors have been synthesized and used to absorb light in OSCs. Two popular structures are phthalocyanines (Pcs, green to blue color) and perylene derivatives, e.g. diindenoperylene (DIP, a red pigment). Examples of Pcs will be discussed in Chapter 2. DIP has been used by Brütting et al. to fabricate planar heterojunction OSCs with a high *FF* of 74.3%, a V_{OC} of 0.93 V and a final PCE of 3.9 %. [53]

Forrest et al. report planar OSCs based on CuPc and C_{60} giving a PCE as high as 4.2% under 4–12 suns simulated AM1.5G illumination. [18] Such a high performance is partially attributed to the significantly reduced series resistance (0.1 Ω cm^2) without using HTL, as the common HTL PEDOT:PSS sometimes leads to an R_sA as large as 400 Ω cm^2. They also point out that the large R_sA of the devices with PEDOT:PSS perhaps comes from a poor interfacial contact between CuPc and PEDOT:PSS, rather than the bulk resistance of the PEODT:PSS layer.

Nevertheless, one drawback of the planar heterojunction OSCs is the relatively short diffusion length of singlet excitons L_{ex}, which is generally 5—30 nm. [54] Meanwhile the optical absorption length, given by 1/α (reciprocal of the absorption coefficient), is usually 0.1—1 μm for most organic semiconductors. [55] $L_{ex} < 1/\alpha$, and therefore, only a small fraction of photons can be harvested in a planar configuration.

1.2.4.3. Bulk-heterojunction organic solar cells

A prototype of the blending bulk-heterojunction (BHJ) OSCs was first reported by Loutfy and Sharp in 1979. In that report, x-form H_2Pc and polyvinyl alcohol mixed in methylene chloride were ball-milled and then coated onto a semitransparent plate (coated with SnO_2/Sb) forming a PAL with a thickness of 1.8—4.5 μm, and an aluminum cathode was finally deposited. [56] Minami et al. later showed that the polymers having polar groups such as halogen or cyano give larger J_{sc} in this type of BHJ-OSCs in 1983. [57]

Hiramoto et al. reported the so-called *p-i-n* BHJ-OSCs by codepositing a blend layer between the donor (H_2Pc) and the acceptor (perylene tetracarboxylic derivative, Me-PTC) in 1991. [58] They found that the internal quantum efficiency is improved about twice by the *p-i-n* structure, in spite of the fact that the recombination in the blend layer is much likely to occur.

Wudl et al. reported a photoinduced charge transfer from a conducting polymer onto fullerene C_{60} in 1992. [59] This finding essentially opened a brand new window for organic solar cells. One year later, they reported the first polymeric BHJ-OSCs with fullerene as the acceptor, and poly(2-methoxy-5-(2'-ethyl-hexyloxy)-1,4-phenylene vinylene) (MEH-PPV) as the donor, which was the prototype of the majority of modern OSCs. [60]

A soluble fullerene derivative [6,6]-phenyl C_{61}-butyric acid methyl ester ($PC_{61}BM$) which has similar energy levels with C_{60}, was synthesized by Wudl et al. in 1995. [61] Simultaneously, they blended the fullerene derivatives in the bulk of PPV, and reported the first PCBM based polymeric BHJ-OSC. [17]

A new soluble C_{60} derivative, indene−C_{60} bisadduct (ICBA), with a LUMO energy level 0.17 eV higher (smaller absolute value) than that of $PC_{61}BM$ was synthesized by He et al. in 2010. [62] Devices based on this acceptor show an improved V_{OC} of 0.84 V and PCE of 5.44% under AM1.5.

Compared with the above C_{60} derivatives, analogous C_{70} derivatives are more thermally stable and show stronger absorption in the visible range of the solar spectra, owing to its lower symmetry compared to C_{60}. $PC_{71}BM$ is currently widely used to fabricate OSCs with PCE higher than 6%, and internal quantum efficiency close to 100%. [63]

Besides the polymeric BHJ-OSCs, small-molecular BHJ-OSCs also have a promising future. A record PCE of 6.7% under AM 1.5G irradiation (100 mW cm^{-2}) for single-junction organic solar cells has been achieved for small-molecular BHJ-OSCs using 5,5'-bis{(4-(7-hexylthiophen-2-yl)thiophen-2-yl)-[1,2,5]thiadiazolo[3,4-c]pyridine}-3,3'-di-2-ethylhexylsilylene-2,2'-bithiophene, $DTS(PTTh_2)_2$, as the donor material, $PC_{71}BM$ as the acceptor, and 1,8-diiodooctane (DIO) as an additive which improves the phase separation of the blend. [64]

One indispensable step in the fabrication of solution processed BHJ-OSCs is an annealing of the blending organic layer prior to the deposition of the top electrode. The annealing has two functions. The first one is to remove residue solvents, and the second one is to improve carrier mobilities by crystallization. [65]

One drawback of solution-processed polymeric BHJ-OSCs is the segregation of components due to a limited miscibility, which in turn affects the overall device's efficiency in a long term. [66]

1.2.5. Efficiency

The generation of photocurrent in heterojunction OSCs needs to overcome obstacles in steps 1—5 as shown in Figure 1–7:

1. The forbidden band gap E_g (the energy gap between HOMO and LUMO);

2. The low diffusion length of excitons in organic semiconductors with a relatively low

dielectric constant (the dielectric constant ε is 11.79 in crystalline silicon at room temperature, whereas about 3 in organic semiconductors [67]);

3. The recombination of excited charges at the D-A interface;

4. For polymeric semiconductors: the relaxation of hot charge-transfer states, forming localized polarons (charges together with the geometrical deformation of polymeric chains); [13] For small-molecular semiconductors: the Coulomb attraction between oppositely charged ions;

5. The low or imbalanced carrier mobility in semiconductors, or charge traps, or the formation of polarons mainly in polymeric semiconductors.

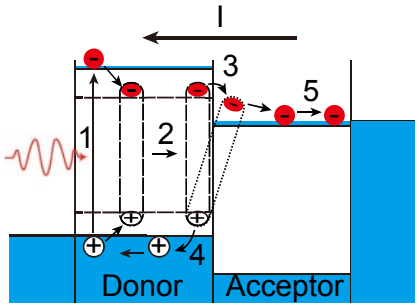

Figure 1–7 Scheme of the photocurrent generation in an organic solar cell. 1) A photon excites an electron to the higher-energy level (LUMO), during which an exciton is simultaneously formed; 2) Diffusion of the exciton towards the D-A interface; 3) Charge transfers at the interface, forming a geminate electron-hole pair; 4) Delocalization of the cooled excited states; 5) Separated charges diffuse in the semiconductor towards electrodes, driven either by the field formed by the difference between the electrode work functions, or by the selectively transporting buffer layers.

For organic solar cells, the fill factor may decrease due to the buildup of space charges caused by the imbalance of the mobilities between holes in the donor and electrons in the acceptor. [22] The consequential S-shape curve gives a small *FF* (Figure 1–4). The maximum ratio allowed for these two mobilities is suggested to be two orders of magnitude. Otherwise, a buildup of space charges will be formed, and both the photocurrent and fill factor will be impaired. [65]

Usually, R_{sh} is large enough, and V_{OC} depends on the potential drop at the interface where excitons are separated. If the charge separation interface is a Schottky junction interface, V_{oc} depends on the difference between the work functions of electrodes. [68] Or if the charge-separation interface is a D-A heterojunction interface with no Schottky interface in the device, V_{OC} depends on the difference between the E_V of the donor (HOMO) and the E_C of acceptor (LUMO). In this latter case, an empirical formula for estimating the V_{OC} of an OSC is

$$V_{\mathrm{OC}} = (1/q)(|E_{\mathrm{HOMO}}^{\mathrm{Donor}}| - |E_{\mathrm{LUMO}}^{\mathrm{Acceptor}}|) - 0.3\ \mathrm{V} \qquad 1\text{-}17$$

where *q* is the elementary charge. The value of 0.3 V in Equation 1-17 is an empirical factor (0.24 V is also given in another reference [69]). This formula is summarized upon 26 OSCs with an identical stack of the same fullerene and different donors having different HOMO levels. The blending PALs are doctor-bladed onto PEDOT:PSS. [70]

External quantum efficiency (EQE) is defined as the ratio of the short-circuit current to the incident photon flux. It composes of the absorption and the internal quantum efficiency (IQE). The former is determined by the thickness, the distribution of light intensity in the PALs and the absorption coefficient α of the PALs (suppose no scattering occurs). The IQE is defined by the ratio of the short-circuit current to the absorbed photon flux, and is reported to be close to 100% in fullerene based bulk-heterojunction organic solar cells.

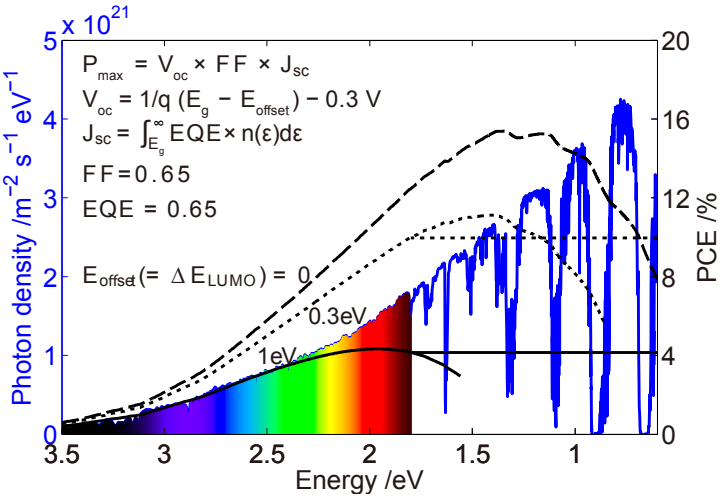

Figure 1–8 Energy density of AM1.5 (blue curve) solar light, as well as the calculated efficiency of solar cells with different E_g of different donor materials, and different energy offsets E_{offset} (0, 0.3, 1.0 eV). Each incident photon is assumed to have a 65% chance of successfully generating an electron which can then flow in the external circuit (EQE = 0.65). *FF* is set to 0.65. The colored patch is cut off at 1.8 eV.

Figure 1–8 shows the energy distribution of the AM1.5 solar light. It also shows the estimated PCE of a fullerene-based OSC with donors having different energy levels under AM1.5. The excitons generated in fullerene is not considered because of its low absorption in the visible range. The 0.3 eV loss of voltage in the second equation comes from Equation 1-17. An energy offset between the LUMO of the donor and the LUMO of the donor fullerene (4.2 eV) is indispensable for separating the excited charges at the *p*-*n* interface.

Figure 1–8 suggests that a material with an E_v of 5.4 eV, and a bandgap of 1.4 eV is most suitable for coupling with fullerene to make high-efficiency heterojunction OSCs. [70] A small-molecular OSC with a V_{OC} of 0.86 V and PCE of 6.3% is fabricated by co-depositing 2,4-bis[4-(N,N-diisobutylamino)-2,6-dihydroxyphenyl] squaraine (DIB-SQ) and C_{70}. The squaraine derivative has a bandgap of 1.7 eV and an HOMO of 5.3 eV. [71]

1.3. Stability of organic solar cells

Although a certificated PCE of 10.6% has been achieved for tandem organic solar cells by 2012. [72] Their stability still demands to be deeply studied. To make OSCs work efficiently and durably simultaneously is an urgent technical issue ahead of researchers.

Just as the electronic properties of semiconductors change dramatically with the presence of impurities, the performance, repeatability and stability of organic solar cells are generally low. Efficiency, manufacturing feasibility and stability constitute three major issues in OSCs. [73] In this section, the degradation occurring in OSCs is discussed.

1.3.1. Degradation

The stability of OSCs currently falls behind their analogue OLEDs. It falls even farther behind their inorganic counterparts ISCs. Improvements of the stability of OSCs are urgently demanded before they can be commercialized. Many efforts have been endeavored to the study of stability of OSCs in recent years, and a consensus on the scientific reports of stability of OSCs between different laboratories has been reached in 2011. [74]

The degradation of OSCs includes both intrinsic and extrinsic degradation. The intrinsic degradation of OSCs usually refers to the degradation inside the devices. It occurs even when the devices are stored in an air-free environment. The extrinsic degradation of OSCs normally refers to the degradation caused by exterior factors. It mainly includes the degradation triggered by the intrusion of oxygen and water.

The intrinsic degradation originates from the thermal diffusion of comprising materials at interfaces, including the phase separation at interfaces of the cathode where exists an intrinsic stress [46, 75], the phase segregation at the interface of semiconductors [76] and the inter-diffusion at the interfaces of buffer layers [77]. Heating [75] or intense irradiation (also its thermal effect) will accelerate the intrinsic degradation. The metal/organic interface is a significant source of degradation of BHJ-OSCs stored in an inert atmosphere. [78] Morphological evolution inside the BHJ-OSCs is reviewed, [79] and the intrinsic degradation due to the phase-segregation of the active materials in BHJ-OSCs is physically modelled. [76]

For small-molecular OSCs, the interdiffusion of buffer layers plays a role in the intrinsic degradation. [77] Metal phthalocyanines and fullerene are intrinsically (thermally) stable materials, and are suggested to be suitable for fabricating OSCs stable on a time scale of thousands of hours with proper protection from air. [52] Besides, the etching of ITO anode by the PEDOT:PSS buffer layer perhaps also plays a role during the intrinsic degradation. [80]

Intrusions of oxygen and water are two main causes of the extrinsic degradation. There

has been an argument on the relative significance between these two factors in literature. One indisputable fact is that although OSCs and OLEDs are based on similar materials and working with almost opposite mechanisms, OSCs are usually less stable than OLEDs. The divergence between their stability is presumably related with the special acceptor material used in OSCs, the fullerene. The electron-transport properties of fullerene suffer much from the exposure to oxygen in air.

Most of the reported air-stable OSCs are either fabricated with an inverted structure with cathode and ETL layer inside the device or stored on the shelf in the dark. The reported half-shelf-lives of unencapsulated OSCs in literature reached three months (about 2000 h), as reported separately by Ferreira et al. in 2011 [81] and by Worfolk et al. in 2012 [82]. The former group reported BHJ-OSCs with an ETL of sol-gel ZnO nanoparticles, whereas the latter group reported inverted-structure polymeric BHJ-OSCs with modified ITO as the cathode. One interesting deduction from these two reports is that although aluminum cathodes were exposed in air in both cases, the devices still showed such high shelf stability. This suggests that the oxidization of the aluminum cathode during the extrinsic degradation of OSCs is perhaps not as serious as it may be suspected to be. When comparing the stability of encapsulated devices with ETLs of ZnO or Cs doped TiO_2, You et al. suggest that devices based on the former have better stability. [83]

1.3.2. Oxygen

Oxygen is normally a p-type dopant (trapping electrons) in organic semiconductors. Therefore, the electronic properties of layers in which holes are the majority carriers may possibly be enhanced by oxygen. On the contrary, the layers in which electrons are the majority carriers will suffer from the existence of oxygen. The latter includes the ETL, the acceptor and the active cathode.

One early example showing the beneficial effect of oxygen on the photovoltaic performance of OSCs was reported by Fan and Faulkner in 1978. [84] The cell has a structure of Al-H_2Pc-Au. In this mono-PAL structure, the Schottky junction between Pc and Al separates the photo-excited carrier pairs. Its photocurrent increases in air over the first several days after exposure to air. This increase is explained by the increase of hole charges in the p-type semiconductor H_2Pc in the presence of oxygen.

Another evidence showing the enhancement effect of oxygen on inorganic-organic hybrid solar cells was reported by Krebs et al. in 2006, with the help of time-of-flight secondary ion mass spectrometry (TOF-SIMS). [85] They showed that the exposure of OSCs to oxygen is crucial for a good function of the devices, although it slowly ages devices in a long term.

More often is a normal structure in which the acceptor/ETL/cathode is outside of the device (close to air). And for this stacking order, oxygen is generally considered as an unwanted substance. Besides the possible photo-oxidation of unsaturated

semiconductors, the destructive effects of oxygen on the electronic properties of the common acceptor fullerene are also well-known. One counter example of this is reported by Wang et al., [86] who show that the shelf lives of fabricated small-molecular OSCs can be greatly improved to about 950 h in air by reversely stacking CuPc and C_{60}. In this case, the ambient oxygen takes a long time to arrive at the acceptor fullerene layer.

The deteriorating effect of oxygen on the photovoltaic performance of OSCs has been comprehensively studied quantitatively by probing the oxygen contents at cathode-acceptor interfaces along with the degradation of a series of OSCs by Krebs's group in 2012. [87] Their results show that oxygen accumulates in the organic layers during the extrinsic degradation of OSCs, especially when the devices are subjected to intense illuminations.

The effect of oxygen on the cathodes of OSCs may vary at different degradation stages depending on the thicknesses and conductivities of the formed oxides. If the oxide layer is (semi-) conducting, or if it is insulating but is thin enough (e.g. < 3 nm), electron can pass readily this layer (by tunneling in the latter case). However, if the oxide is insulating and thicker than 4 nm, the electron tunneling will significantly diminish at this interface. [84] The charge blocking effect of the aluminum oxides formed in air has been suggested. [88]

1.3.3. Water

In some cases, the effect of oxygen is not as significant as water on the extrinsic degradation of OSCs (as the case in OLEDs [46]). One example was reported by Krebs et al. in 2008. [89] They introduced a polymeric donor having ester groups on the side chain, and found that the organic solar cells with this polymer show a very high resistance toward oxygen, but very low resistance toward water.

Unlike the double effects of oxygen on photovoltaics, almost no beneficial effect of water on the stability of OSCs has ever been suggested. The effect of humidity has been suggested to play a role in the degradation of OSCs, particularly in those with hydrophilic buffer layers, like an HTL of PEDOT:PSS [90] or an ETL of BCP or BPhen [91]. The physical swelling of these materials, as well as the corrosion of the active cathodes in the presence of water may accelerate the degradation of OSCs. The ratio of partial pressure of water to the saturated vapor pressure is described as the relative humidity (RH). Exposure in a high RH (over 90%) for a long period may cause a serious rupture of the cathode of an OSC, as shown in Chapter 5.

The diffusion of water in the aluminum cathode was suggested to proceed through the grain-boundaries by Krebs et al. in 2008, using isotope-labelled $H_2{}^{18}O$. [90] They showed that 90% RH induces the rapid degradation of BHJ-OSCs, and further concluded that water passes the grain boundaries in the aluminum cathode even in the dark, and the penetrated water continues diffusing vertically throughout the PALs until the ITO layer.

The vertical diffusion of water in the PALs was found to be accelerated by light irradiation. A model based on the vertical diffusion of water through the encapsulation film and aluminum film in encapsulated OSCs with various encapsulation films was then reported. [92]

It should be noted that humidity generally affects OSCs seriously at a relatively high RH (>80% for example [47]), which suggests that the effect of humidity is perhaps not linear to RH.

1.3.4. Light irradiation

Light irradiation may cause the photo-degradation of organic semiconductors, which contains unsaturated chemical bonds. The photochemical stability of organic solar cells has been reviewed in reference. [93]

For the extrinsic degradation, light irradiation accelerates the diffusion of oxygen and water in the bulk of organic PALs. [94, 95] The short-wavelength part further accelerates the photochemical oxidation of the organic materials.

Besides accelerating extrinsic degradation, the thermal effect of light irradiation may also accelerate the intrinsic degradation of OSCs. The interdiffusion of buffer layers into organic layers in small-molecular OSCs will be accelerated by intense light illuminations.

1.4. Aim of this study

Stability is the biggest issue in organic semiconductor devices, including organic light-emitting diodes, [46] and organic solar cells, etc. Serious degradation in air limits wide applications of these flexible, light-weight and low-cost devices. Studying the stability of organic solar cells will help us understand degradation mechanisms and improve the stability of these devices.

Organic solar cells are considered as one of the green ways to harvest the massive solar energy. Over the course of the past few years, organic solar cells have been extensively studied with thousands of scientific papers published each year. The manufacturing aim of organic solar cells is to realize an avenue of harvesting solar energy. The total energy output of a fabricated solar cell equals the product of its efficiency and lifetime. In the past two decades, the efficiency has been remarkably improved through many approaches like broadening the absorption ranges in the solar spectra. Stability is another important indicator of how good a solar cell is. The shelf-lives of organic solar cells exposed in air have been substantially improved to thousands of hours in the past few years. [73] These efforts have made organic solar cells both scientifically attractive, and technologically important.

Organic solar cells convert photo-energy to electric energy in air. Under light irradiation,

the unsaturated organic semiconductors in the cells are prone to photolysis and photo-oxidation. To prevent the photo-oxidation, fabricated solar cells need to be perfectly encapsulated with thick glass plates, which are stiff. Even in the encapsulated devices, slow penetration of air often occurs. It demands that the fabricated devices should be highly resistant to air under light irradiation. In other words, organic solar cells need to be both intrinsically and extrinsically stable. Therefore, it is extremely important to understand the degradation mechanisms of the unencapsulated organic solar cells under light irradiation in air.

One ultimate challenge in studying the degradation of organic solar cells is to quantify the contribution from each degradation mechanism to the overall degradation of the photovoltaic performance. [87] A simple degradation model is the key of both understanding and preventing the degradation of organic solar cells. However, the ordinarily various and intricate fabrication procedures of organic solar cells and the lack of an accurate control of storage conditions make it extremely challenging to build a simple and systematical model of the degradation of organic solar cells in air. Until now, few studies have investigated the dynamical degradation models of organic solar cells.

Small-molecular organic solar cells with PALs composed of CuPc and C_{60} represent the simplest planar structure of a heterojunction organic solar cell. Both materials have already been widely studied in many areas for many years, and their physical and chemical properties have been well established. These well-established properties make physical modelling the extrinsic degradation of this system feasible, reliable and widely applicable. Another important feature of these two materials is that both of them are environmentally friendly. In this study, we have built a simple model for the extrinsic degradation of small-molecular organic solar cells, based on detailed experimental observations. Experimental observations over decades of devices agree well with this model.

Besides the quantitative analysis of the extrinsic degradation of OSCs, it is also important to prevent the extrinsic degradation with some simple and economical method. Several approaches have been reported to be capable of stabilizing unencapsulated organic solar cells. Referring to the commercialized OLEDs, a minimum shelf-life on a time scale of a year is necessitated.

Using metal oxides as the ETL has been the most effective way to fabricate the so-called air-stable organic solar cells which usually refer to the unencapsulated devices with half-shelf-lives exceeding several weeks. This method could have improved the half-shelf-lives of unencapsulated organic solar cells to about three months in the dark. From a practical point of view, such a life time is far from sufficient. The shelf stability needs to get greatly improved before the organic solar cells are capable of genuinely harvesting energy from the massive solar radiation. Besides, these metal oxides are usually solution-processed in several steps, thereby consuming much time. Their applications to the fast vacuum-processed devices are limited.

To overcome the above issues, we need to find a material that could scavenge oxygen but not block the electron transport in devices and more importantly, it should be processed easily and economically. In this study, we could have realized an average half-shelf-life of a year for unencapsulated small-molecular organic solar cells by inserting an ultrathin titanium layer beneath the widely-used aluminum cathode.

Organic solar cells are supposed to work stably under solar light. Therefore, air-stable OSCs are expected to withstand continuous light irradiation, under which the weathering stability is more important than the aforementioned shelf stability. The weathering tests reflect the real stability of fabricated devices under a relatively harsh condition. We have tested the weathering stability of the bilayer-cathode devices in this thesis.

The stabilization mechanisms of metal oxides buffer layers have been suggested to be an oxygen-scavenging effect. Devices with bilayer cathodes show superior shelf stability than the devices with metal oxides. By probing the mechanisms behind these really air-stable bilayer-cathode devices, we improve our understanding of the degradation of unencapsulated small-molecular organic solar cells. This improved understanding makes us believe that the stability of organic solar cells in air can be finally improved to a practically usable level with an economic, efficient and simple method. The stability of organic solar cells will not necessarily be an insurmountable problem for commercialization.

1.5. Contents of this thesis

The content of this thesis is composed of six chapters. The first chapter describes the background, and the second chapter describes the experimental. The 3rd chapter describes the experimental results, and the 4th chapter discusses several models for fitting various experimentally recorded degradation curves. The 5th chapter discusses a novel Ti-Al bilayer cathode, which improves the stability of organic solar cells. The 6th chapter is the conclusion chapter. The following explains the main contents in each chapter.

Chapter 1. Introduction

This chapter includes motivation and aim of this study, general principles of photovoltaic, milestones in the history and core terms widely used in organic solar cells. Important factors influencing the stability of unencapsulated organic solar cells, including oxygen, water and light, are also discussed.

Chapter 2. Experiments

Functionality and purification of materials, and vacuum equipment used in this study are discussed. Fabrication procedures of devices with a structure of ITO/PEDOT:PSS (or MoO_3)/CuPc/C_{60}/BCP (or LiF)/Al are explained in detail. Several techniques used for characterizing organic solar cells are demonstrated, including sheet resistivity, crystalline

form, UV-visible absorption, surface morphology, and the spatial distribution of elements, etc. We also comment on the aperture method that is considered as the accurate photovoltaic measurement method of organic solar cells.

Chapter 3. Light-induced degradation

In this chapter, we show effects of light on the degradation of unencapsulated organic solar cells in different degradation stages stored either in air or in vacuum. In air, among devices fabricated in one batch, those stored in a dark box degrade relatively slowly than those stored under fluorescent lamps. In vacuum, organic solar cells reach equilibrium after consuming adsorbed oxygen under light irradiation, and this equilibrium will be broken by exposure to air. The synergistic effect of oxygen and light irradiation on the degradation of organic solar cells is accordingly evidenced. Detailed experimental results show that the light-induced degradation in small-molecular organic solar cells is related with the photo-aging of the acceptor layer, i.e. the fullerene layer.

Chapter 4. Modeling of degradation curves

In this chapter, we propose models to explain extrinsic degradation curves of unencapsulated organic solar cells stored on the shelf. When oxygen is considered as the major cause of the extrinsic degradation, a lateral diffusion model of oxygen in fullerene layers agrees the best with experimental observations. According to simulations with this diffusion model, microscopic pinholes in the aluminum cathode are insufficient to cause the rapid degradation of an unencapsulated OSC in the initial few hours. Instead, we hypothesize that oxygen can also pass parts of grain-boundaries in the cathode that are wide enough. Combined this model with experimental observations, we propose that the diffusion constant of oxygen in fullerene is increased at least sevenfold under fluorescent lamps.

Chapter 5. Titanium-aluminum bilayer cathode

In this chapter, we systematically examine novel bilayer cathodes. As discussed in previous chapters, intrusion of air from pinholes and grain-boundaries in the cathode causes the main short-term degradation. To eliminate the intrusion of air, we replace the traditional aluminum cathode with a titanium-aluminum bilayer cathode. This novel bilayer cathode dramatically improves the life time of an unencapsulated organic solar cell stored in air by three orders of magnitude, i.e. from a few hours to thousands of hours. We compare effects of different buffer layers on the stability of both aluminum and aluminum-titanium devices. Bilayer-cathode devices with BCP as the electron transport layers and PEDOT:PSS as the hole transport layers perform the best. Effects of humidity on the stability of devices with different cathodes or different buffer layers are discussed. Aluminum devices cannot resist RH > 50%. On the contrary, aluminum-titanium devices are highly resistant to ordinary humidity, although the bilayer cathodes are ruptured under RH > 90%. In order to investigate the stabilization mechanisms of the bilayer cathode, we check both surface morphology with AFM and elemental depth

profiles with TOF-SIMS of devices with different cathodes. According to the experimental results, the stabilization mechanisms of bilayer cathode are proposed as:

- The titanium layer eliminates microscopic pinholes in the aluminum cathode;
- The titanium layer hinders the interdiffusion of LiF and aluminum to organic layers;
- The aluminum layer improves the oxygen scavenging capability of the titanium layer, during which aluminum gets passivated and suppresses further oxygen intrusion.

Besides, we speculate that the titanium layer also protects aluminum from corrosion.

Chapter 6: Conclusions

In this chapter, we summarize our experimental observations and proposed theories.

Chapter 2. Experiments

In this Chapter, we discuss materials and techniques used in this study.

2.1. Materials

2.1.1. Photoactive materials

Metal phthalocyanines (MPcs) and fullerene (C_{60}) were used as the photoactive materials. The term of phthalocyanine was coined by R. Linstead in 1933. The central hydrogen atoms of H_2Pc can be substituted by more than 70 metal atoms. By further substituting the peripheral hydrogen atoms, over 5000 phthalocyanine compounds had been prepared by 1990. Copper phthalocyanine (CuPc) is the most sought after phthalocyanine. It can be synthesized in two ways, either from copper and o-dicyanobenzene, [96] or from urea, phthalic anhydride, cuprous chloride and ammonium molybdate, either in or without solvent, with reaction at 200 ^oC. [97]

When used in OSCs, Pcs usually give a relatively low V_{OC}. Nevertheless, many researchers have proven that Pcs are promising components of OSCs due to their high thermal stability and strong absorption in the visible part of solar spectra. Besides the CuPc, non-metal phthalocyanine (H_2Pc) or Zinc phthalocyanine (ZnPc) are also very popular Pcs and have been widely used in OSCs. These two Pcs are usually used to fabricate the so-called *p-i-n* OSCs. [58, 98] Hiramoto et al. have made OSCs with a PCE of 5.3% using a very thick (960 nm) blending *i*-interlayer of H_2Pc:C_{60}. [99] They annealed the device during the codeposition to enhance the device performance. High purities of these two source materials are also indispensable to the increased thickness of the blending interlayer. Interestingly, CuPc:C_{60} blend was suggested to be not suitable for such a *p-i-n* structure. [53]

The term of fullerene was coined by Kroto and Smalley in 1985. [100] It is used to denote the whole class of closed-cage carbon allotropes. The structure of C_{60} and C_{70} satisfies both the Euler's theorem and the isolated pentagon rule. The former confines the number of hexagons of a cage composed of only pentagons and hexagons to be 12, while the latter confines the pentagons not adjacent to one another. Abundant C_{60} can be formed in vaporized graphite because the C_{60} molecule can withstand collisions with species in the energy range of hundreds of eV and heating to above 1000 ^oC. [101]

C_{60} is usually extracted from the soot produced from electric arcs between two graphite electrodes that are mounted in an inert atmosphere. In another thermal preparation approach, source graphite is first vaporized by heating at 1300 ^oC, and then C_{60} is generated upon quenching (e.g. > 100 Torr He). [102] Fullerene C_{60} has a characteristic

Raman shift at 1467 cm^{-1}, [45] and four lines in IR absorption spectra at 527, 577, 1183, 1428 cm^{-1}. [103]

Both Pcs and C_{60} have been suggested to have no adverse effects on human health. [97, 101] Therefore, devices made from these two materials normally cause no environmental problems. They are also exceptionally chemically stable under a normal storage condition.

2.1.2. Electrode and buffer layer materials

Indium tin oxide (ITO) and aluminum were used as the electrodes. ITO has a very high transparency in the visible spectra, and at the same time a high electric conductivity at room temperature. Besides, it is stable under normal storage conditions. Therefore, it has dominated transparent electrodes of thin-film electronic devices.

PEDOT:PSS and molybdenum trioxide (MoO_3) were two HTLs used in this study. It notes that MoO_3 is not transparent to visible light, as shown in Figure 2–9. PEDOT:PSS is prone to absorbing water in air. By substituting PSS^- in PEODT:PSS with a neutral polymer poly(ethylene glycol), a hydrophobic conductive polymer PEDOT:PEG can be dispersed in a mixture of nitromethane and ethanol (PEDOT-block-PEG, Aedotron P-NM). We found that a device with PEDOT:PEG (45 nm) as the HTL showed little photovoltaic capability. The reason was probably that PEDOT:PEG has a work function (4.3 eV [104]) mismatching that of either ITO or CuPc.

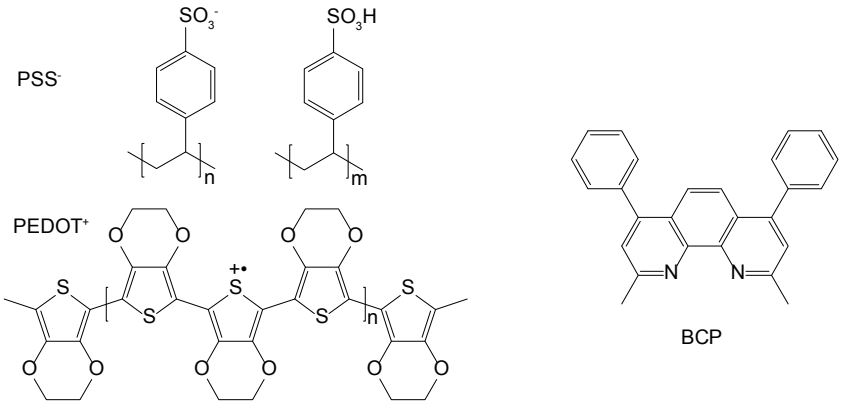

Figure 2–1 Chemical structure of (left) PEDOT:PSS (BAYTRON P VP AI 4083) and (right) BCP.

LiF and BCP were two ETLs used in this study. LiF has been used beneath the aluminum cathodes of BHJ-OSCs to enhance the fill factor and stabilizes high open circuit voltage. [105] The reason of such an enhancement is perhaps that LiF lowers the work function of aluminum (4.16 eV → 2.75 eV). [106]

BCP (2,9-Dimethyl-4,7-diphenyl-1,10-phenanthroline, chemical structure on the right of Figure 2–1) has been widely used as the ETL in small-molecular OSCs based on CuPc and fullerene. A BCP layer not only blocks the transport of holes, but also facilitates the

transport of electrons. On the other hand, several nanometers of BCP may also hinder the interdiffusion between aluminum and fullerene. [77] Finally, a BCP layer could possibly slow down the vertical diffusion of oxygen into the beneath fullerene layer. Nevertheless, one drawback of BCP is that it is prone to recrystallization in a high humid environment. [69]

Aluminum has been widely used as the cathodes of OSCs. The deposition rate of the aluminum cathode substantially influenced the efficiency of a fabricated device. PCE of a device increases with the deposition rate of the cathode. Kim et al. attributes it to the formation of a flat interface between aluminum and organic layers at a relatively high deposition rate. They observe an intermixing layer of about 4 nm existing in the device with a slowly deposited cathode. [107]

The interdiffusion between cathode and adjacent organic layers may not only hinder the electron transport, but also increase the possibility of an electric shortage between electrodes inside the device. There are two possible ways to overcome such an interdiffusion problem. One way is to cool down the substrate (with the organic layer already deposited) during the deposition of metal, under which the metal-organic interface has a high thermal stability. [108] Another possible way is to pre-deposit a layer of amorphous metal oxides, which interdiffuse much slower than metals upon organic layers. [109]

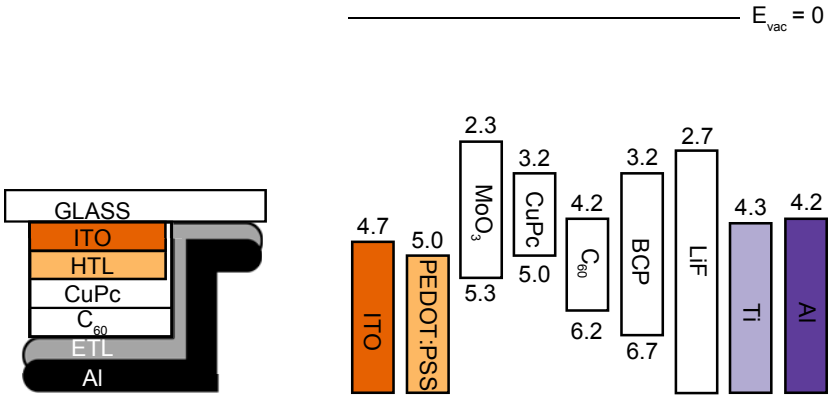

Figure 2–2 (left) schematic diagram of the stack structure of the devices mentioned in this study. (Right) Energy levels of materials before contact.

2.2. Fabrication

Small-molecular organic solar cells with a stack structure shown on the left of Figure 2–2 were fabricated with the following procedures. The hole transport layer (HTL) was PEDOT:PSS or MoO_3. The electron transport layer (ETL) was LiF or TiO_x or BCP. The cathode was Al or Ti or Al-Ti. Energy levels of these materials are shown on the right of *Figure 2*–2. They were averaged over reported values found in literature.

2.2.1. Equipment

A vacuum deposition system (Eiko, OLED deposition system), referred to as EL chamber hereinafter, was used as the main vacuum-deposition apparatus, with a diagram illustrated on the left of Figure *2*–3. It has a main chamber (C1) in which the base pressure could be reduced to 5×10^{-6} Pa. A sample transporting chamber (C2) with a base pressure of about 10^{-5} Pa is connected to the main chamber for changing deposition masks. It allows us to consecutively deposit all films sequentially without breaking the vacuum. The main chamber is connected to two sub-chambers for organic materials (2 and 3) and one sub-chamber for high-temperature materials (1). In sub-chamber 1, there are a 3kW electron-beam gun (illustrated in the middle of Figure *2*–3) for depositing high melting point metals, and a K-cell type evaporator with a maximum temperature of 1700 ^{o}C for evaporating either LiF or MoO_3. Organic materials, including CuPc, C_{60}, and BCP, etc. were evaporated in sub-chamber 2 or 3.

Another bell-shape chamber (on the right of Figure *2*–3) with a base pressure of 5×10^{-4} Pa was also used for depositing both Al and LiF of devices discussed in Chapter 3 and Chapter 4, whereas aluminum and titanium mentioned in Chapter 5 was mainly deposited in the EL system. It notes that the base pressure of the cathode-deposition chamber was found to influence the stability of fabricated devices. [110]

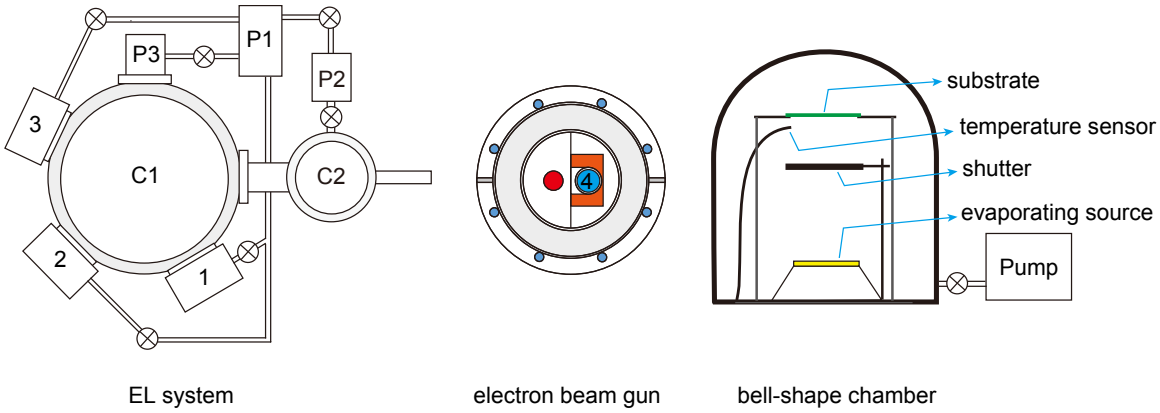

Figure 2–3 Simplified scheme of the deposition systems used in this thesis. (Left) top view of the EL system; (middle) top view of the electron-beam gun mounted in chamber 1 of the EL system with the deposited metal set in the crucible at position 4. Pumps 1—3 mean: a rotary pump (P1), a turbomolecular pump (TMP, P2), and a cryogenic pump (P3); (right) side view of the bell-shape chamber.

The deposition rate Γ (nm/s) of a thermally deposited material is related with the source temperature T following Equation 2-1. The $1/\sqrt{T}$ term comes from the Langmuir expression, [111] while the exponential term comes from the exponential relation of vapor pressure with temperature.

$$\Gamma = A \cdot \frac{1}{\sqrt{T}} \cdot 10^{-B/T} \qquad \text{2-1}$$

where *A* and *B* are constants. It notes that the deposition rate at a given temperature also depends on other factors like the target-source distance and the remained amount of sample in the evaporation crucible, etc.

On the other hand, the thickness of a spin-coated film can be estimated by the following equation

$$d = \sqrt{\frac{\eta}{4\pi\rho\omega^2}} \cdot \sqrt{\frac{1}{t}} \qquad \text{2-2}$$

where η is the viscosity coefficient of the solution, ρ the density, ω the angular velocity in circle per minute, and t the time.

2.2.2. Purification

The purity influences the electronic properties of organic semiconductors. Although some impurities in the source materials may enhance the performance of an OSC, [112] according to literature, 2—3 times purifications from raw materials are usually needed. [99, 113] Both CuPc, ZnPc and C_{60} were purified with a train sublimation system (the main part is illustrated in Figure 2–4). Similar sublimation system has been widely used in literature. [114] A glass or quartz tube with raw materials in one side was set into a copper tube. The end of the copper tube where raw materials were placed was then heated to a high temperature. Inside the tube was formed a temperature gradient.

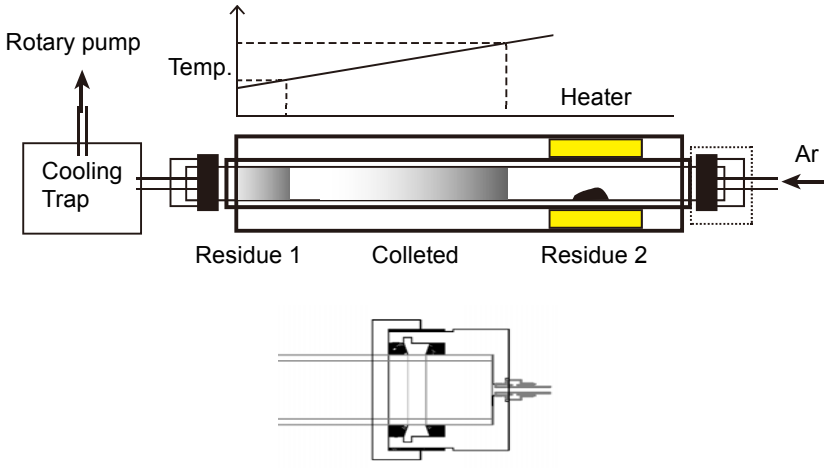

Figure 2–4 Diagram of the gradient sublimation system. Three ingredients are separated by the temperature gradient in the tube. Some gas molecules are trapped in the cooling trap immersed in liquid nitrogen. The lower diagram shows the cross-section of the zoomed adapter between the glass tube and Ar inlet tube in the dotted frame. Two O-rings (black parts) were used to seal the adaptor.

The working principle of this system is that different materials having different sublimation temperatures (generating a certain vapor pressure) will condense at different regions inside the tube. The main ingredient can be separated by properly setting a heating temperature.

In a routine experiment, fullerene (2 g, 99%, Frontier Carbon) was set into a cleaned quartz tube (72 cm, Φ4 cm) using a glassine scoop. After sealing both sides with the adapters, the tube was pumped with a rotary pump to 5 Pa in one hour. Then Ar (> 99.999%, O_2 < 0.2 ppm) was used to remove the adsorbed oxygen overnight at a rate of 10 ml min^{-1}. Then the heater was heated up to 700 ^oC in 4 h and kept at this temperature for 8 h, while Ar continued to flow at a rate of 30 ml/min. The working pressure was 200–350 Pa. It notes here that this pressure influences the size of the formed single crystal. [99] After the tube cooled down to room temperature, shiny crystalline sample condensed on the inner wall of the cooler part of the tube was collected with a plastic spatula. The yield of C_{60} increased with the number of sublimation. Generally, it was more than 70% for the 1st sublimation starting from as-purchased soot. The purified C_{60} was stored in Ar before usage.

For CuPc (> 90%, β form, Tokyo Chemical Industry Co., Ltd., TCI) and ZnPc (> 95%, TCI), the temperatures of the heater were set to 550 ^oC and 570 ^oC, respectively. Both materials were twice purified by sublimation.

After obtaining twice purified organic materials, we fabricated OSCs with procedures described below.

2.2.3. ITO

The ITO layer was patterned by etching commercial ITO glass using concentrated nitric acid and hydrochloric acid. A glass substrate with 150 nm ITO (GEOMATEC, 9 Ω/square) was cut to 1.5×1.5 cm^2 pieces and etched into designed patterns with acids. A stripe of adhesive tape with a specific width was attached onto the ITO surface. The size of the tape, with a width of either 1.05 cm or 0.3 cm, determined the ITO size. After exposing the ITO glass pieces in the acid atmosphere for 20 min, they were rinsed with tap water.

The patterned ITO glass pieces were sequentially cleaned with distilled water, acetone and isopropanol in an ultrasonic bath in 15 min for each solvent and then blown dry with high pressure nitrogen.

2.2.4. PEDOT:PSS or MoO_3

PEDOT:PSS solution (Baytron P VP AI 4083, structure in Figure 2–1) was treated in an ultrasonic bath for 60 min before being filtered through a 0.45 μm PVDF membrane. PEDOT:PSS wets a hydrophilic surface. Therefore, the patterned ITO substrates were

pretreated with UV/O_3 for 20 min to increase the surface hydrophilicity. Then spin-coating was done in a clean room. For depositing a 60 nm PEDOT:PSS film, the rotating speed increased gradually from 2000 rpm to 4000 rpm in 45s (5s—2000 rpm × 10s—3000 rpm × 10s—4000 rpm × 20s).

The peripheral part of the PEDOT:PSS film was then wiped away with wet tissues, leaving only the central PEDOT:PSS on ITO. And then they were baked on a 150 ^oC hot plate in an Ar glove box or in a 120 ^oC oven in air for 30 min, and cooled down naturally over several hours. Thickness of the PEDOT:PSS film was measured with a DEKTAK surface profiler. Increasing ω from 4000 to 5000 rpm and 8000 rpm leaded to thicknesses of about 50 nm and 30 nm, respectively.

For devices with MoO_3 as the HTL, MoO_3 (5 nm, Wako, 99.9%) was thermally deposited at 300—500 ^oC in the EL chamber.

2.2.5. CuPc and C_{60}

CuPc was deposited at 0.01—0.1 nm/s in the EL chamber. Upon the CuPc film, C_{60} (40 nm) was sequentially deposited at 0.03—0.1 nm/s in the same chamber without breaking the vacuum.

Organic films were then annealed in an Ar glove box at 155 ^oC for 10 min. After cooling down, they were transferred to the bell-shaped chamber for depositions of the ETL and the cathode. During the transfer, the organic layers were exposed in air twice for about 20 s.

2.2.6. LiF or BCP

LiF (1—2 nm, Sigma Aldrich, 99.995%) was deposited at 0.02 nm s^{-1} either in the bell-shape chamber or in the EL chamber. BCP (8 nm, TCI, > 99.0%) was deposited at 0.1 nm s^{-1} (200—220 ^oC) in the EL chamber.

2.2.7. Cathode

For cathodes of devices discussed in Chapter 3 and Chapter 4, Al (75 nm, Sigma Aldrich, 99.999%) was deposited at 0.02—0.15 nm s^{-1} in the bell-shape chamber. Aluminum cathodes of 75 nm were deposited in the bell-shape chamber.

For most devices discussed in Chapter 5, cathodes composed of Al (100 nm, Sigma Aldrich, 99.999%) or Ti (2 to 100 nm, Nilaco, 99.5%) were deposited with the EB gun in the EL chamber. Aluminum cathodes of 100 nm were deposited with the EB gun in the EL chamber.

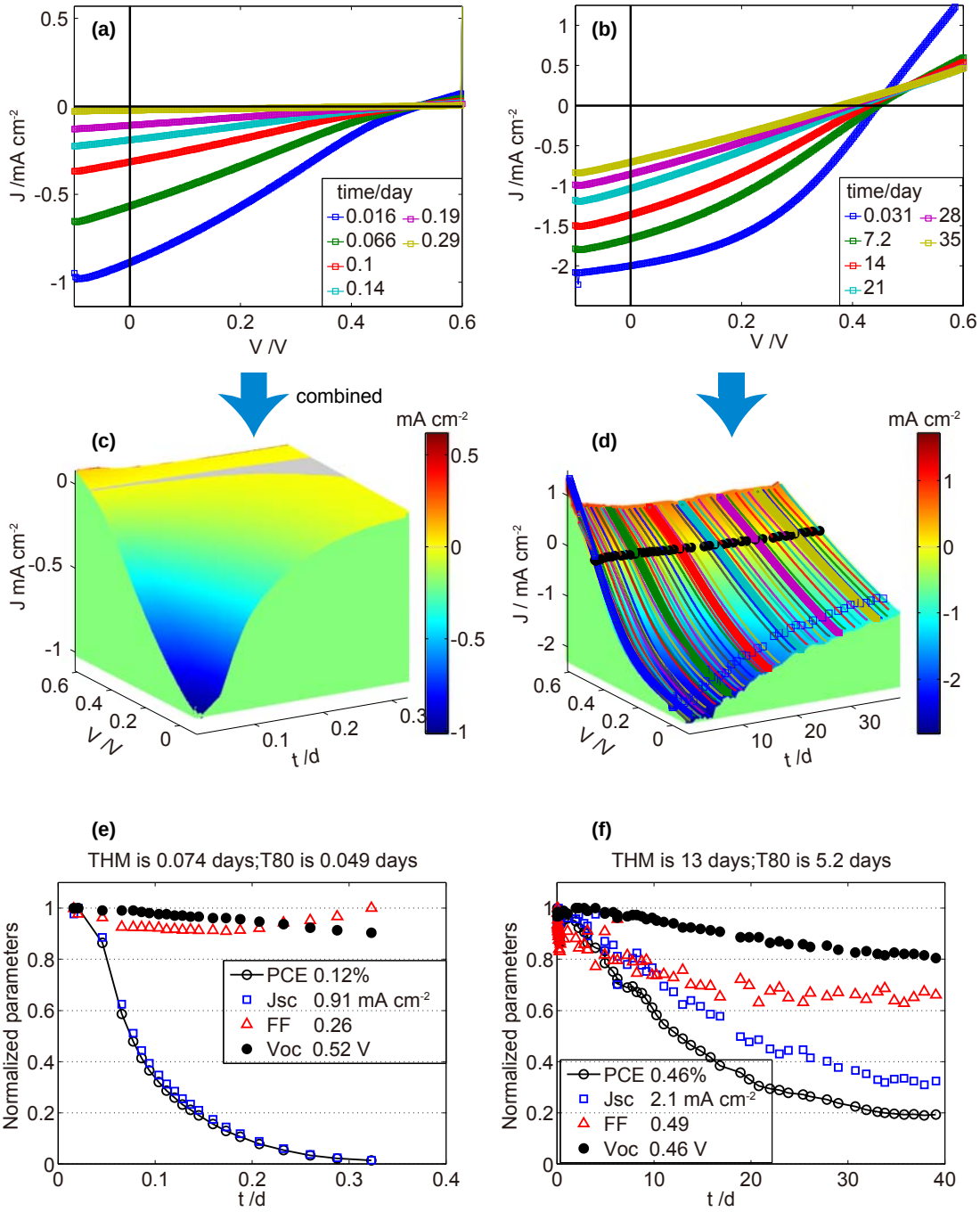

Figure 2–5 Effect of the encapsulation on Al-OSCs stored in air. *J-V* curves of (a) the unencapsulated Al-OSC and (b) the encapsulated Al-OSC; (c, d) *J-V-t* valleys of the unencapsulated device and the encapsulated device respectively, plotted by combining J-V curves with the corresponding time calculated according to the creation time of the related data files. The gray patch indicates the evolution of V_{OC}. Blackish solid circles and bluish hollow squares show evolutions of V_{OC} and J_{SC}, respectively; (e, f) evolution of key parameters of cells in (c) and (d), respectively. Values corresponding to the normalization unity are noted in legends.

2.2.8. Encapsulation

Some fabricated OSCs were encapsulated with glass pieces sealed with UV-curing resin in an Ar glove box before being tested in air. During the UV curing the active area was covered with a patch of polyimide tape, which is opaque to UV light. The resin was cured in five minutes under UV light.

Comparison of an encapsulated device and an unencapsulated device from the same batch is shown in Figure 2–5. These results were measured with a halogen lamp with a light intensity of 80 mW cm^{-2}.

In literature related with the shelf stability of organic solar cells, intermittently recorded *J-V* curves were usually plotted in a single figure, as shown in *Figure 2*–5(b). However, such a 2-D plotting becomes indecipherable when the number of *J-V* curves exceeds five. In order to show decades of *J-V* curves in a single decipherable figure, we plotted them with the corresponding time in a 3-D *J-V*-time coordinate, in a way shown in *Figure 2*–5(d). Similar figures shown hereinafter were plotted in this way, without further showing separate *J-V* curves. One can consider the left front cross-section as the initial *J-V* curve, and the right front cross-section as the evolution of current density at V = -0.1 V, which resembles that of J_{SC}. The evolution of V_{OC} is marked with the gray patch on the valley. The volume of the valley visually indicates the cell's integral quality.

The half-shelf-life (T50) and T80 have been defined as the time for PCE reaching 50% and 80% of the initial value, respectively. [74] However, the maximum efficiency of a fabricated solar cell may be several times the initial value, especially for some of the bilayer-cathode devices discussed in Chapter 5. In this case, T50 no longer reflects the actual shelf stability of a cell, and the time of half-maximum (THM, the time for a fabricated device reaching half of the maximum instead of the initial) PCE was more suitable for comparing shelf lives between devices. The time for PCE reaching 80% of the maximum value was defined similarly and denoted as T80 hereinafter. The encapsulation elongated the T80 of a device by about two orders of magnitude. Meanwhile, the encapsulation seemed to have improved the performance of the encapsulated device as well.

2.3. Optimization

In this section, we discuss the effects of fabrication variables on OSCs. It notes that for devices with cathodes deposited in different chambers, conclusions applicable to one may be inapplicable to another.

2.3.1. HTL

J-V curves of two devices with a structure of ITO (150 nm)/[MoO_3 (5 nm) or PEDOT:PSS

(50 nm)] /CuPc (20 nm)/C_{60} (40 nm)/BCP (8 nm)/Al (100 nm) are shown in Figure 2–6. They were measured under simulated AM1.5 (100 mW cm^{-2}). Extracted parameters with units of Ω cm^2 for R_sA and R_{sh}A, mA cm^{-2} for J_{SC}, V for V_{OC}, and % for PCE were used hereinafter without further notification. V_{OC} of a MoO_3 device is about 0.03 V lower than the that of a PEDOT:PSS device (with same other layers) on average.

Besides the divergence of V_{OC}, the series resistance R_sA of the MoO_3 device (0.9 Ω cm^2) is much lower than that of the PEDOT:PSS device (6 Ω cm^2). This suggests that the contact between CuPc and MoO_3 is better than that between PEDOT:PSS and CuPc. [18]

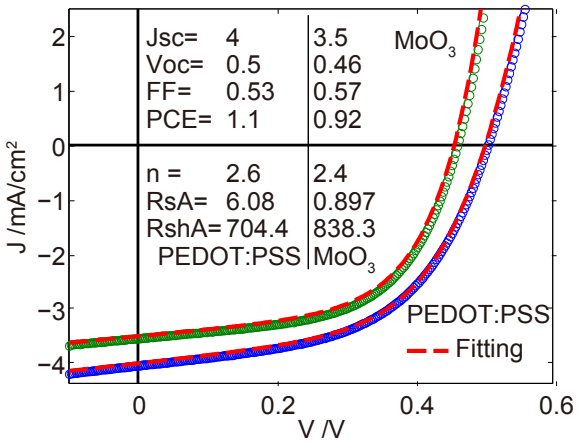

Figure 2–6 J-V curves of devices with different HTLs. The green one is the J-V curve of the device with MoO_3, and the blue one is the J-V curve of a device with PEDOT:PSS. Also noted were the extracted parameters with the *Delta-approximation method*.

For devices with an HTL of PEODT:PSS, we checked the influence of thickness and baking condition on the performances of fabricated devices. Devices with a structure is ITO/PEDOT:PSS (x nm)/CuPc (20 nm)/C_{60} (40 nm)/BCP (8 nm)/Al (100 nm), with x equals to 30, 50, 60 nm were fabricated. After the fabrication, *J-V* curves of a fabricated device were measured under simulated AM1.5 (100 mW cm^{-2}). The results are shown on the left of Figure 2–7 and summarized in Table *2*. The thickness of the PEDOT:PSS film did not significantly influence the performance. We used either 50 nm or 60 nm of PEDOT:PSS to fabricate devices in this study.

Table 2 Summary of averaged R_sA, THM and PCE of devices with PEDOT:PSS films of different thicknesses

Thickness / nm	**R_sA / Ω cm^2**	**THM / h**	**PCE / %**
30	14	0.80	0.92
50	12	1.06	1.03
60	11	0.80	0.98

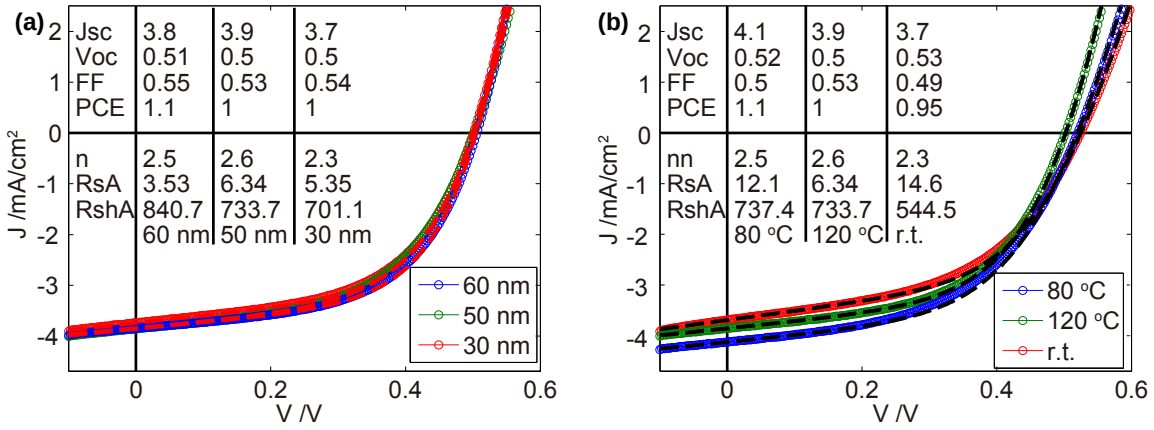

Figure 2–7 (left) J-V curves of devices with PEDOT:PSS films of different thicknesses. Three curves almost overlap with each other. (Right) J-V curves of OSCs with the PEDOT:PSS film baked at 120 °C for 30min (green), at 80 °C for 15 min (blue), and without baking (red). Also noted are the extracted parameters as well as the related fitting curves (dashed).

To check the effects of the baking temperature of PEDOT:PSS films on the performance of a fabricated device, we compared performances of three groups of devices fabricated in one batch: group 1 were not baked; group 2 were baked in an 80 °C oven for 15 min in air; group 3 were baked in a 120 °C oven for 30 min in air. *J-V* curves of typical devices from these three groups are shown on the right of Figure *2*–7. The baking seemed to have slightly improved PCE, *FF* and THM, but noticeably reduced R_sA of devices (see also Table *3* and Figure *2*–8).

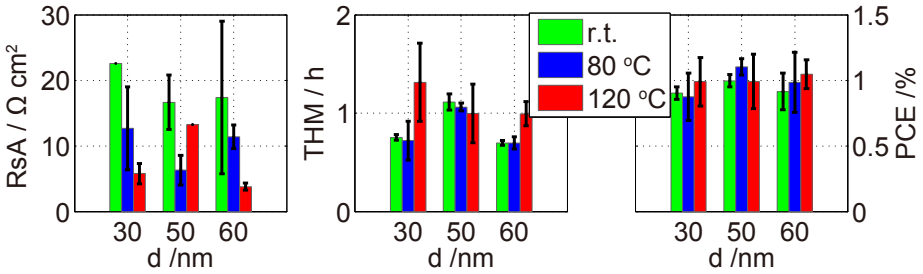

Figure 2–8 Bar charts of R_sA, THM, and PCE of cells with PEDOT:PSS layers of different thicknesses and with different baking treatments. Each error bar was averaged over two devices. Two values of R_sA are not extractable (30 nm r.t. and 50 nm 120 °C). For extraction methods, see Chapter 1.

Effects of thicknesses and baking conditions of PEDOT:PSS films on the performances of devices are shown in Figure *2*–8. We attributed the reduced R_sA (left of Figure *2*–8) of the 120 °C baked devices to a reduced amount of water in the PEDOT:PSS films.

Table 3 Summary of averaged R_SA, THM and PCE of devices with PEDOT:PSS films baked under different conditions

Baking conditions	R_SA / Ω cm^2	THM / h	PCE / %
No-baking	18	0.85	0.94
80 °C, 15 min	10	0.83	0.99
120 °C, 30 min	8	1.1	1.00

2.3.2. Donor

The absorption of light by the composing dyes is the first step of power generation in organic solar cells. The absorption coefficients α of ITO, PEDOT:PSS, C_{60}, ZnPc and CuPc used in OSCs were estimated from the related absorption spectra tested in air at room temperature (Figure 2–9).

UV-vis absorption spectra of ZnPc and CuPc are very close, as shown in *Figure 2*–9. We fabricated several devices with ZnPc as donors. *J-V* curves of devices from the same batch with different donors are shown in Figure 2–10. They were tested under a halogen lamp (80 mW cm^{-2}, spectra shown in Figure 2–21), after exposed in air for 40 min due to technical reason. As both devices suffered much from the air exposure, their half-shelf-lives were only 1.5 h (ZnPc) and 1.9 h (CuPc). Therefore, it is difficult to make a conclusion from these results. Nevertheless, as this layer is not the layer causing the extrinsic degradation of devices, we only discussed the stability of devices with CuPc as donors in this study.

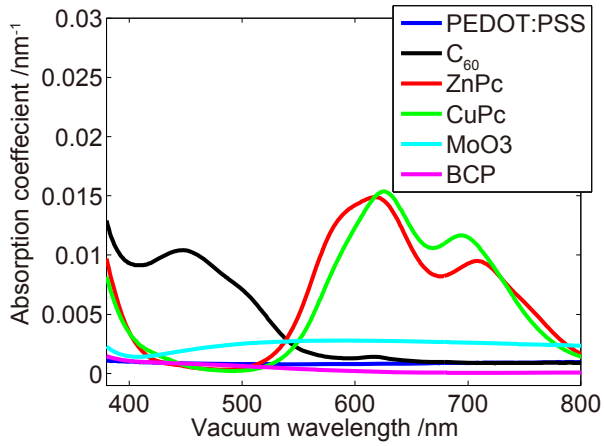

Figure 2–9 Absorption coefficients of materials deposited on glass for C_{60} and ZnPc, and on quartz for others.

The thickness of the CuPc layer seemed to affect the device performance and stability, as shown in the following experiment. We compared four devices with CuPc layers of

different thicknesses. Two chambers were used to deposit LiF and Al: for cell A (25 nm CuPc), the bell-shape chamber was used, whereas for cells B (25 nm, 20 nm, 12.5 nm CuPc) the EL chamber was used. After fabrication, *J-V* curves were tested under a halogen lamp (80 mW cm^{-2}, spectra in Figure 2–21), beyond which the devices were stored in the dark. The initial *J-V* curves are shown in *Figure 2*–11(a). Degradation curves of these devices are shown in *Figure 2*–11(b).

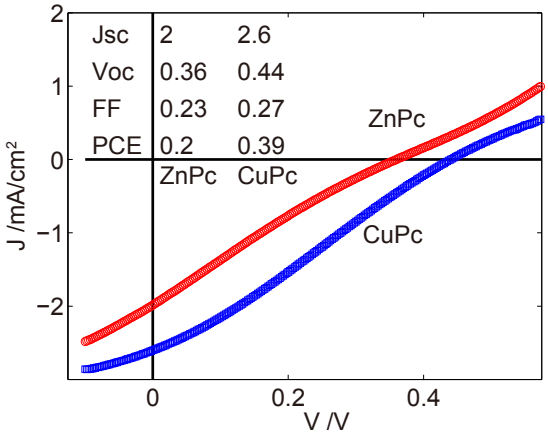

Figure 2–10 J-V curves of two OSCs with a structure of ITO (150 nm)/PEDOT:PSS (60 nm)/CuPc (blue curve) or ZnPc (red curve) (25 nm)/C_{60} (40 nm)/LiF (2 nm)/Al (75 nm) after exposed in air for 40 min.

Cell A (red circles) showed an S-shape *J-V* curve, and its THM was about three days. On the contrary, cells B showed relatively squared *J-V* curves and their THMs were several hours. Interestingly, for devices fabricated in the same chamber (cells B), V_{OC} increased with the thickness of CuPc, whereas J_{SC} was less influenced. *FF* was highest at 20 nm (green triangles), presumably resulting from balanced charge mobilities in CuPc and in C_{60}. We used 20 nm or 25 nm CuPc in this study.

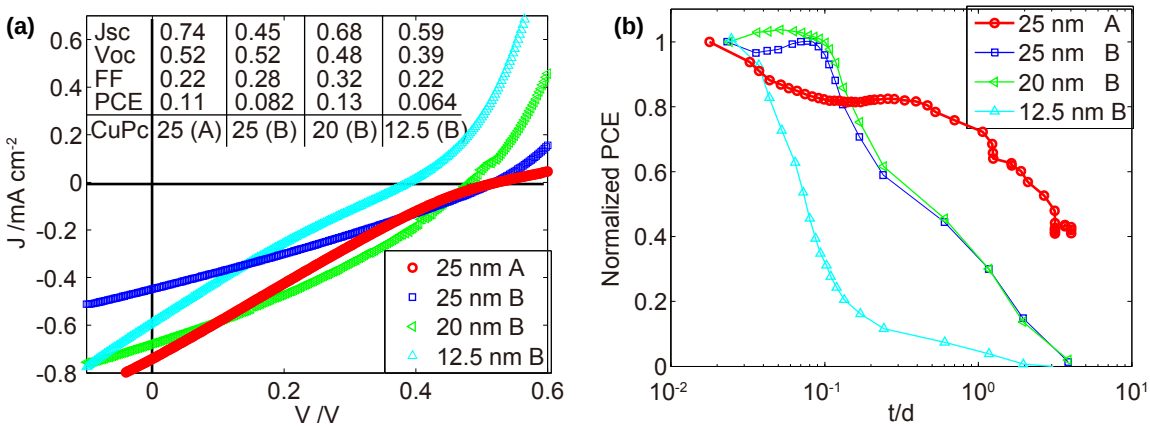

Figure 2–11 (a) initial performance of four devices with a structure of ITO (150 nm)/PEDOT:PSS (60 nm)/CuPc (A: 25 nm; B: 12.5/20/25 nm)/C_{60} (40 nm)/LiF (1.5 nm)/Al (80 nm). (b) Evolution of normalized PCEs (to the initial values) of these devices.

2.3.3. ETL

Generally, devices with BCP as ETLs showed better performances, both efficiently and durably, than devices with LiF as ETLs. Comparison of performances of devices with LiF and BCP is discussed in Chapter 5. It has been reported that a BCP layer over 10 nm reduces the performance of an OSC due to charge accumulation at the cathode interface. [22] We used 8 nm BCP for devices mentioned in this study.

2.3.4. Temperature in chamber

We found that the temperature inside the bell-shape chamber after deposition (T_{final}) or before opening (T_{open}) influenced the performance and stability of devices. T_{final} varied from 150 ^{o}C to 190 ^{o}C, under which the organic layers might have been annealed as shown in Section 2.3.6. In general, devices showed relatively high initial performances when T_{final} was lower than 170 ^{o}C.

Divergence of T_{final} was probably related with the horizontality of the evaporation crucible in such a way that when the crucible was inclined, melted aluminum would flow towards one end of the crucible, leading the applied bias to over-heat the other end. Accordingly, T_{final} as well as performances of fabricated devices varied a lot.

On the other hand, T_{open} seemed to influence the stability of devices. As a rule of thumb, the higher T_{open}, the lower the stability (*Figure 2*–12). This temperature might influence the oxidation of cathode or the contact between donor and cathode.

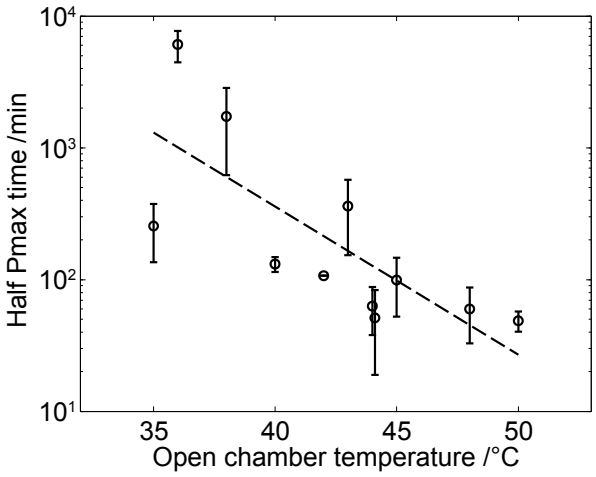

Figure 2–12 Half-shelf-lives of several batches of OSCs with respect to T_{open}. The oblique dashed line is the fitting curve.

2.3.5. Other cathodes

Besides Al, Ti and Al/Ti cathodes, Al/Ca was also used as the cathode. Devices with such a bilayer cathode have been suggested to show better performances, both initially and durably in an inert atmosphere. [115] Both Ca and Al were thermally evaporated in the bell-shape chamber. According to two preliminary experiments, devices with such cathodes performed much worse than Al-cathode devices. Therefore, we mainly used aluminum as the cathodes.

2.3.6. Annealing

2.3.6.1. *Performance*

The effect of annealing on polymeric OSCs has been mentioned in the introduction chapter. For small-molecular OSCs, there are two types of annealing, the pre- and the post-annealing. The effect of post-annealing on the performance of small-molecular OSCs depends on the stacking pattern of organic layers.

For the *p-i-n* structure, the post-annealing improves the performances of OSCs by creating an interpenetrating network of the donor and acceptor materials. During the post-annealing, a silver cathode (100 nm) functioning as a confining cap which prevents the formation of a rough surface while allowing for the formation of an interpenetrating donor-acceptor network is indispensable. [116]

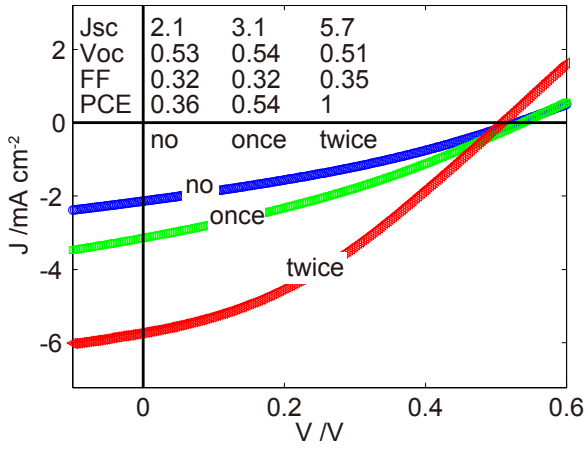

Figure 2–13 Comparison of the performance of three organic solar cells with the same structure, but with different times of pre-annealing treatments.

For the planar *p-n* structure, the post-annealing had no significant effect on the performance of a device. Post-annealing sometimes resulted in wrinkles on the surfaces of solar cells, especially for those cells once tested in air. The cause for the formation of wrinkles was probably the buckling effects of different films. Formation of wrinkles completely inactivated the post-annealed cell.

Pre-annealing means the annealing that is done before the deposition of the cathode. We found that twice pre-annealing of the organic film generally led to a better performance. Effects of different annealing treatments, i.e. no pre, once pre, and twice pre-annealing on performances of devices are shown in Figure 2–13. These devices had the same structure of ITO/PEDOT:PSS (60 nm)/CuPc (25 nm)/C_{60} (40 nm)/LiF (2 nm)/Al (75 nm). *J-V* curves were measured under the halogen lamp (80 mW cm^{-2}, spectra in Figure 2–21).

To probe the effects of pre-annealing on properties of the constituting organic films (CuPc and C_{60}), we compared the surface morphology, hardness and crystallization of the organic films before and after pre-annealing.

2.3.6.2. *Surface morphology*

We examined the surface morphology by comparing four cells with the same structure of ITO (150 nm)/PEDOT:PSS (60 nm)/CuPc (25 nm)/C_{60} (40 nm) without annealing or after 30 minutes of annealing on a 100 °C, 150 °C, or 200 °C hot plate in an Ar glove box.

The results in Figure 2–14 show that the unannealed film was composed of small domains of fullerene (maybe inherited from beneath CuPc domains). Upon annealing, the surfaces of films became coarse. We may infer that the contact between CuPc and C_{60} could have been increased after the pre-annealing.

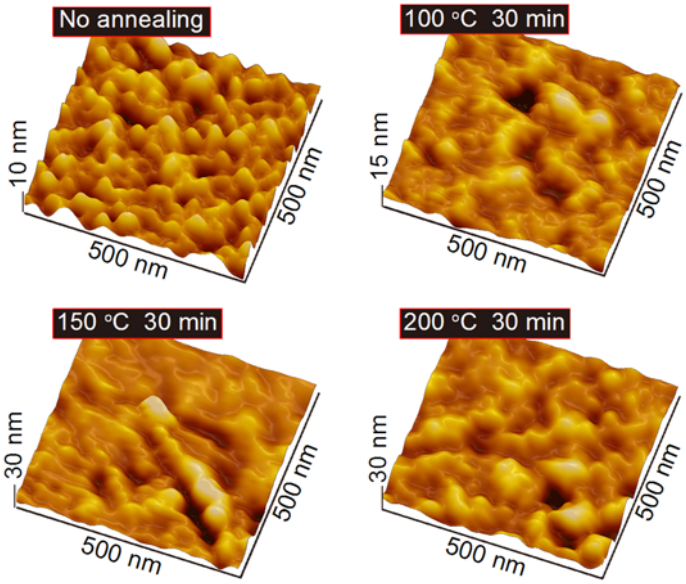

Figure 2–14 Surface morphology (500 × 500 nm^2) of organic layers upon annealing. The annealing temperature and time were noted on the top of each figure.

2.3.6.3. *Film hardness*

Organic solar cells sometimes fail due to the bombardment of the cathode during deposition. [117] Thermal annealing is an effective approach to improve the physical strength of organic films. We confirmed this by measuring the Brinell scale hardness

which is usually represented by the indentation of materials through the scale of penetration of an indenter loaded on a material test-piece. The pre-annealing hardened the surface of the organic layer (C_{60}) as shown below.

Two cells with a laminated structure of ITO (150 nm)/PEDOT:PSS (60 nm)/CuPc (25 nm)/C_{60} (40 nm) were fabricated as normal. One cell was taken to an Ar glove box and annealed on a 160 ^{o}C hot plate for 15 min. Then its surface was notched under a DEKTAK 3ST surface profiler with a constant force and moving speed: 1 mN and 20 µm s^{-1}. Decades of parallel lines with an average distance of about 200 µm were notched (Figure 2–15). The force on the tip was estimated to be in the order of 10^8 Pa. The depth and hardness of the notches were characterized with a dynamic mode AFM (DFM). The Resonance frequency of the cantilever was 348 kHz, and the amplifier reference was -0.150. By comparing the depth of notches on the annealed surface and that on an unannealed surface, we could compare the relative hardness of the organic films. The results are shown in Figure 2–16.

The notches on the surface of the unannealed film are as deep as 40 nm and extended to the end of the depressed paths. This depth corresponds to the thickness of the C_{60} layer which meant the CuPc layer is harder than the unannealed C_{60} layer. The phases at the bottom of the trapezoid cross-sections are different from the peripheral part (top two figures in Figure 2–16). We can conclude that the changed phase shift came from the CuPc layer.

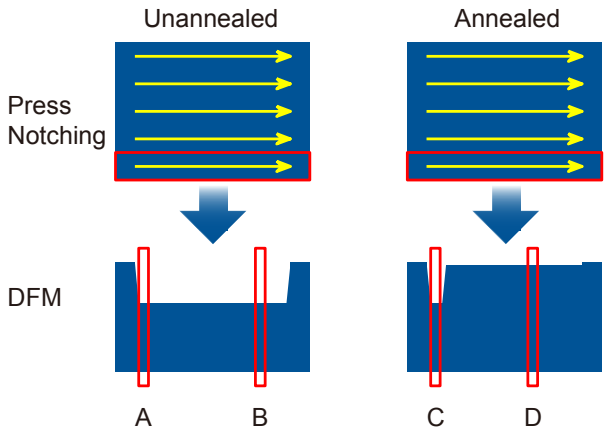

Figure 2–15 Diagram of the experimental procedures for measuring the relative Brinell hardness of organic films. The DFM images at positions A, B, C and D are shown in Figure 2–16.

On the other hand, the annealed cell was found to be too hard to be deep scratched. The notching only compressed the C_{60} film, rather than pierced it. On the surface of the C_{60}, very short notches were observed at the starting position (bottom left of Figure 2–16). Along with the scratching, wide depressions were observed. The phase shift images suggest that the compressed region is harder than the uncompressed region (bottom right of Figure 2–16).

The strengthened C_{60} film might originate from the refinement effects of recrystallization by heat treatment. Besides, grains also grow at elevated temperatures to reduce the boundary energy. Aluminum is a metal with a recrystallization temperature of only 80 °C. [118] Furthermore, rapid cooling through the freezing temperature favors the formation of an amorphous solid, since little time is allowed for the ordering process. The surface-enhanced C_{60} film mitigated the impact of aluminum clusters during the deposition of aluminum, thereby reducing the intermixing of the aluminum cathode during deposition.

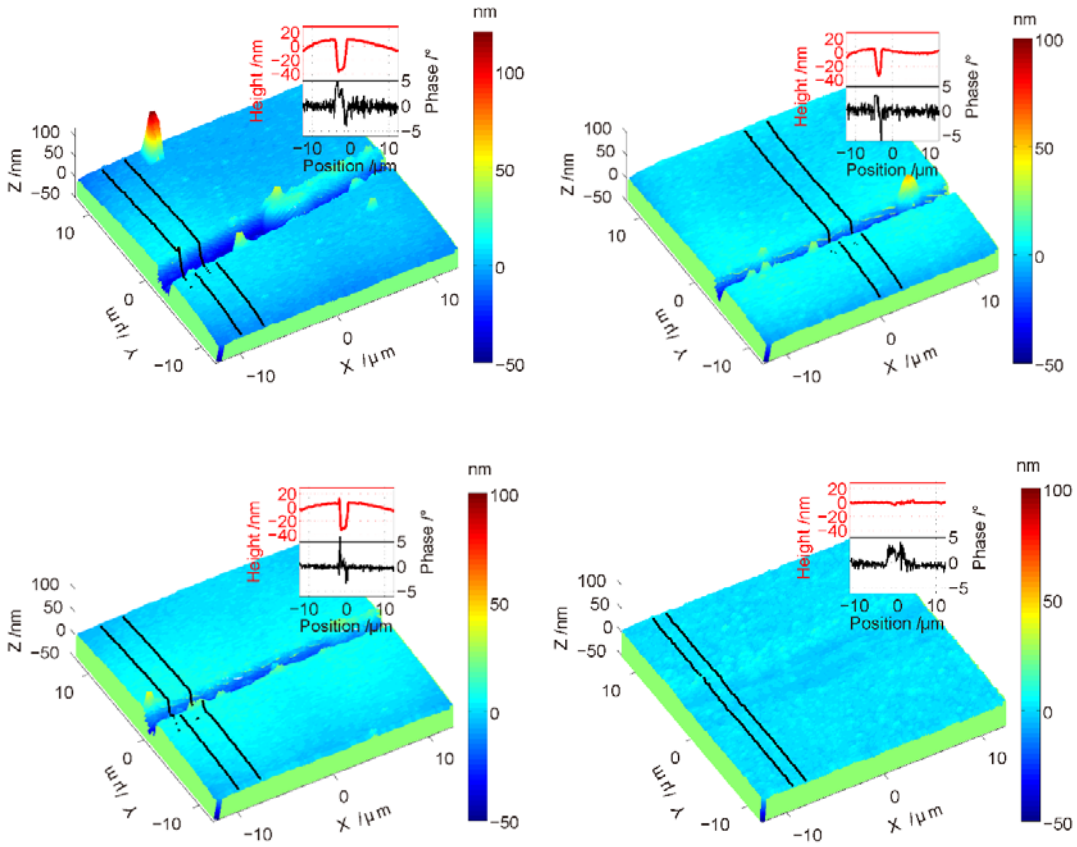

Figure 2–16 DFM images of the unannealed and annealed films shown in Figure 2–15. (Top left) position A and (top right) position B of the cell without annealing; (bottom left) position C and (bottom right) position D of the cell after annealing. The insets show the area average topological (red) and phase shift (black) linear profiles between the two parallel lines marked on the film surfaces.

2.3.6.4. *Crystalline form*

We suspected that the annealing might change the crystalline forms of organic layers. Two cells with a laminated structure of ITO (150 nm)/PEDOT:PSS (60 nm)/CuPc (25 nm)/C_{60}(40 nm) were fabricated as normal. After annealing one cell, we analyzed the crystallization of both cells with X-ray diffraction (XRD), with results shown in Figure 2–17. Only ITO and CuPc layer showed X-ray diffraction. The fullerene did not show X-ray diffraction, probably because carbon atoms are not heavy enough to significantly reflect the incident X-ray.

The XRD results suggest that the structure of the CuPc layer in the cell was α-form (triclinic). [119, 120] This agrees with the absorption spectra (Figure 2–9). The χ dependent intensity distribution shown on the right of Figure 2–17 indicates that the (001) plane of CuPc crystallites orientated parallel to the substrate plane. In other words, CuPc molecules tilted at an angle of 63° from the substrate surface. [120] The annealing did not change the stacking pattern or the crystalline form, but led to an increased crystallization of CuPc, as indicated by the slightly increased intensity at 2θ = 6.893° after annealing.

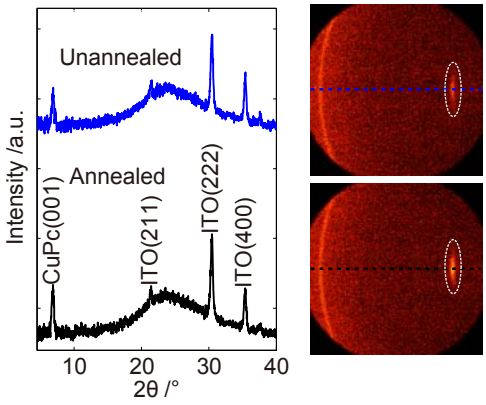

Figure 2–17 XRD results of the annealed (bottom, black) and unannealed (top, blue) cells. The left-side figure shows the χ integrals of the measured data. The peaks were labeled with the corresponding lattice planes. The right-side figures show the measured data. The short vertical arcs closed in the dotted ovals correspond to 2θ = 6.893° (d = 1.28 nm).

2.4. Film analysis

2.4.1. Thickness

The thickness of each film was measured with a Dektak^{3}ST surface profiler (Vecco). For metal oxides, a narrow groove was etched with acids. For soft materials, two parallel grooves with a distance of about one mililimeter on the surface of the film were scratched with a plastic blade. Each scratched groove was about one millimeter wide. Vertical resolution of the surface profiler is about 10 nm. Thicknesses of several films were also checked with AFM. They agreed with each other, proving the reliability of both approaches.

2.4.2. UV-Vis spectra

UV-Vis (300—900 nm) absorbance and transmittance were measured with a V-560 Spectrophotometer (JASCO). An ancillary stage was affixed onto the spectrometer to measure the in situ spectra of cells without metal cathodes inside a portable vacuum

chamber. The portable chamber was part of a cryogenic system (Oxford Instruments Limited). The chamber was pumped with a TMP.

2.4.3. XRD

The crystalline structures of organic films upon annealing were evaluated with a D8 DISCOVER with GADDS XRD system (Bruker). This system uses a 50 kV Cu-Kα X-ray source and an HI-STAR area detector. Three rotation angles of the sample substrate for collecting the data shown in Figure 2–17 were: base rotation angle ω = 2.25°, rotation above the horizontal axis ψ = 0, and in-plane (substrate) rotation angle ϕ = 0.

2.4.4. AFM and DFM

The surface morphology, viscoelasticity and thicknesses of fabricated films were characterized with a scanning probe microscope (SPA400, Seiko). For hard materials, the contact mode of SPM (AFM) was used. This mode works by scanning the cantilever across the sample surface while monitoring the change in cantilever deflection. A metal cantilever made of gold touches the surface of sample. Force constant of the cantilever usually ranges from 0.01 to 1.0 N m^{-1}, with forces ranging from nN to μN.

For soft materials, the phase shift at the tapping mode of the SPM (also called dynamic force microscope, DFM) can be used to identify the distribution of multi-components having different mechanical properties like viscosity and hardness. The DFM scans a tip on an oscillating cantilever across the sample surface. The cantilever is oscillated at or near its resonance frequency (~ 340 kHz). Viscoelasticity of the fullerene films upon annealing was estimated with DFM, with results shown in Figure 2–16.

2.4.5. Sheet resistance

The resistivities of PEDOT:PSS films spin-coated on glass were measured with a Van Der Pauw diagonal 4-point probe method illustrated on the top right of Figure 2–18. The sheet resistance of the film equals $\pi V/(I \ln 2)$, where V and I were measured with a Keithley2400 SourceMeter. This measurement method requires ohmic contacts between probes and the substrate. In order to generate a force onto each probe uniformly, a two mm thick polydimethylsiloxane (PDMS) cushion was used beneath the tested cell. The PDMS film was made in the following way. Monomer and initiator of PDMS with a 9/1 mass ratio were mixed and fully stirred. The sticky mixture was then pumped for 30 min to remove bubbles. Then the mixture was applied onto a matrix and then heated inside an 80 °C oven in air for 15 min to get solidified.

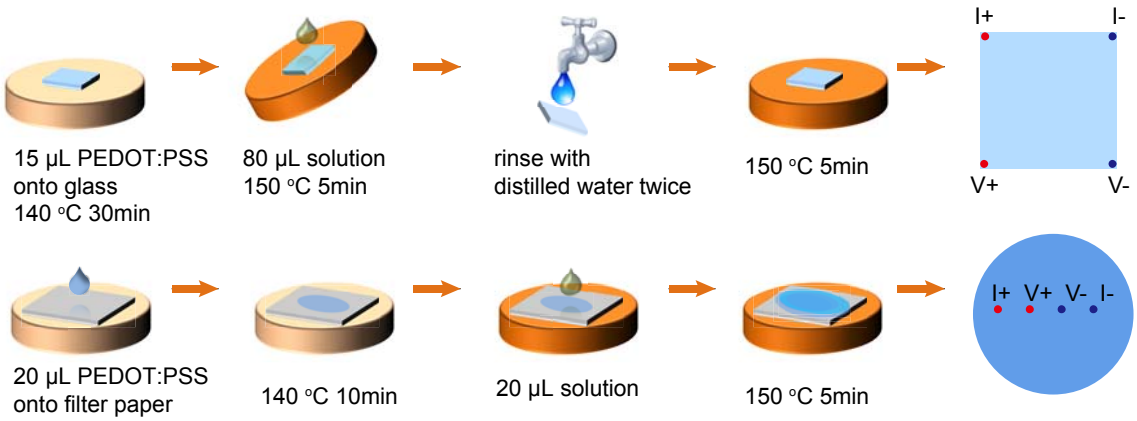

Figure 2–18 Scheme of the measurements of sheet resistance of PEDOT:PSS films with different treatments.

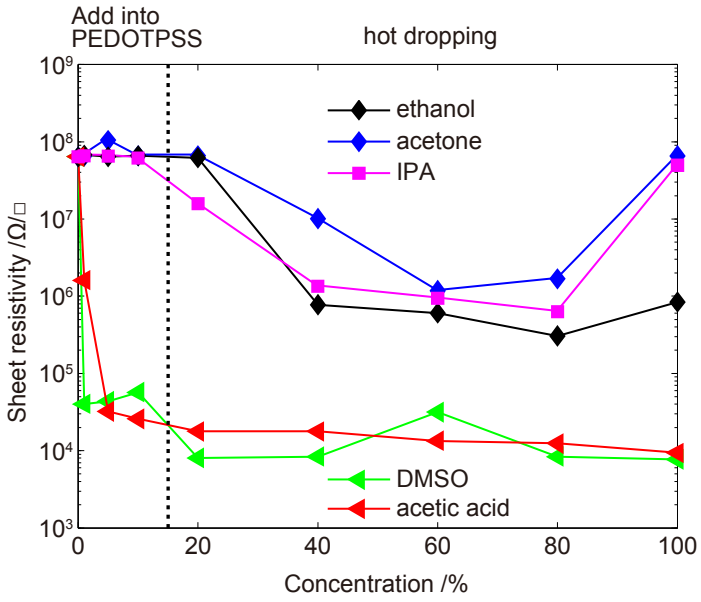

Figure 2–19 Sheet resistivity of PEDOT:PSS films upon different treatments with five different aqueous solutions.

Linear 4-point probe method, illustrated on the bottom right of Figure 2–18 was also used to estimate the conductivity of PEDOT:PSS films dispersed on filter paper. In this case, the four probes were set in an equidistant I (+)—V (+)—V (-)—I (-) arrangement. For an infinite sheet, the sheet resistance of a film also equals $\pi V/(I \ln 2)$. For a finite sheet, the size and direction of probes need to be taken into account. [121]

We compared the sheet conductivities of PEDOT:PSS films treated with different methods. The conductivities of spin-coated PEDOT:PSS films could be improved by either adding polar additives like acetic acid or dimethyl sulfoxide (DMSO) to the aqueous dispersion, or rinsing the as-coated films with aqueous solutions of polar organic solvents. Results of different treatments are shown in Figure 2–19. However, we excluded the relationship between this conductivity and the device's efficiency. According to a preliminary experiment, a device with a pristine PEDOT:PSS film performed better than a

device with a surface-treated PEDOT:PSS film.

2.4.6. TOF-SIMS

Spatial distribution of elements in organic solar cells was analyzed with time of flight-secondary ion mass spectrometry (TOF-SIMS), which is a combined technique of SIMS and TOF. The principle of SIMS is that under the bombardment of a focused fast ion beam, namely primary ions, surface species of the specimen will be simultaneously sputtered within 10^{-12} s. These secondary ions are then accelerated by an acceleration voltage U. The mass/charge ratios of the secondary ions are identified with the TOF according to the time they arrive at the detector $T = \sqrt{mL^2/(2qU)}$ where L is the distance from the detector to the outlet of the acceleration chamber, m the ion mass, and q the ion charge. TOF-SIMS has a high sensitivity and accuracy and therefore, has been used to analyze the chemical composition on the solid surface. [122]

Information of the depth profiles of different species can be obtained with TOF-SIMS performed in a dual-beam mode, by etching the detected sample layer by layer. The analysis is typically performed using a high energy but low current ion beam (usually Bi^{3+}), while the etching is performed using a high current but lower energy source, e.g. Cs^+, O_2^+ or C_{60}^+. [123]

TOF-SIMS has been widely used to study the degradation of OSCs, by virtue of its high resolution of chemical species in each layer of OSCs. We used this technique to probe the vertical distributions of oxygen, aluminum, titanium, lithium, and fluorine, etc. in different devices. The TOF-SIMS (5-100-AD, ION-TOF GmbH) used Bi^{3+} (60.0 keV, 0.04 pA, 100.0 × 100.0 μm^2) as the analysis ion, and Cs^+ and O_2^+ (2.0 keV, 470 nA, 300.0 × 300.0 μm^2) as the sputtering ions for generating electronegative and electropositive ions, respectively. The TOF-SIMS results are discussed in Chapter 5.

2.5. Photovoltaic measurement

2.5.1. Light sources

Three types of light sources were used in this study. Their light intensities were monitored with a Gentec SOLO 2 Powermeter. For the study in Chapter 3, we used a halogen lamp (MORITEX MHAA-100W) with an IR-cutoff filter (~ 80 mW cm^{-2}) and a Xe lamp with two IR-cutoff filters (90—100 mW cm^{-2}), with an optical diagram shown in Supporting figure 2. Their spectra are shown in Figure 2–21.

Energy distributions of the light sources were measured with a USB2000 Fiber Optic spectrometer which was calibrated with a standard halogen lamp (OCEAN Optics). The

sensitivity of the spectrometer and the spectra of the standard lamp are shown in Figure 2–20.

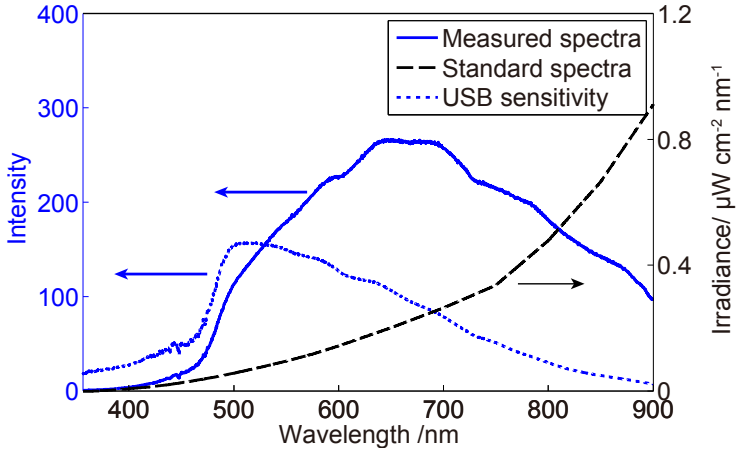

Figure 2–20 Irradicance of a standard halogen lamp (black dashed), as well as the measured spectra (blue solid) by the USB2000 spectrometer. The sensitivity of the USB2000 spectrometer (blue dotted) is calculated by dividing these two spectra.

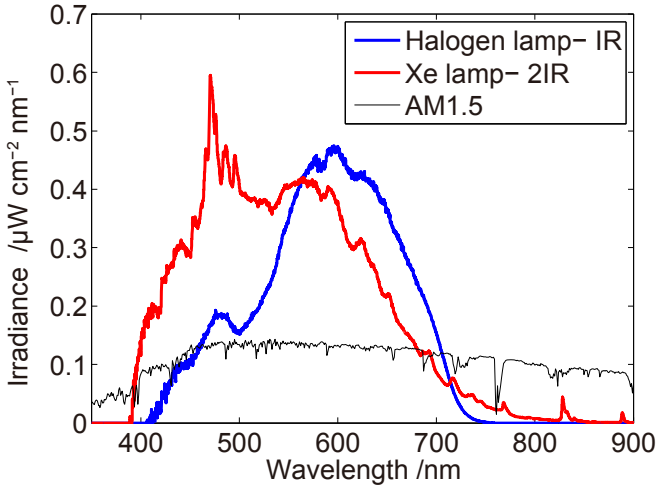

Figure 2–21 Irradiances of the two light sources, i.e. a halogen lamp and a Xe lamp with related filters. Also shown is the AM1.5 reference spectra.

For other photovoltaic measurements, an HAL-C100 solar simulator (AM 1.5, 100 mW cm^{-2}) was used. This light source is Class A, [2] in the central area of 1.2 × 1.2 cm^2. The testing system, including the solar simulator, a Keithley2400 SourceMeter, and a computer is shown in Figure 2–22.

[2] According to Japanese Industrial Standard (JIS-C8912), class A corresponds to positional uniformity of irradiance < ± 2%, temporal stability of irradiance < ± 1%, and spectral match of 0.75—1.25 (see Supporting figure 1).

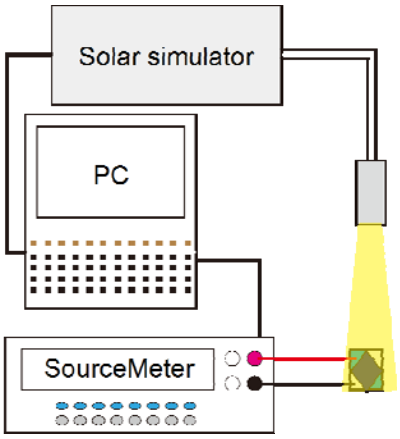

Figure 2–22 Diagram of the I-V testing system. The solar simulator and the Keithley2400 SourceMeter were controlled with the laptop.

Light intensity of the solar simulator decreased with the operation time due to the aging of the inner Xe lamp (Figure 2–23). Relation between the light intensity *I* (in mW cm^{-2}), the equipment setting (*LI*, default setting is 40), and the operation time *t* (in hour) approximately followed Equation 2-3. The light intensity *I* was adjusted to being within 98—101 mW cm^{-2} each time.

$$I \approx (-0.00359 \times LI + 0.0904) \times t + 3.84 \times LI - 53.1 \qquad 2\text{-}3$$

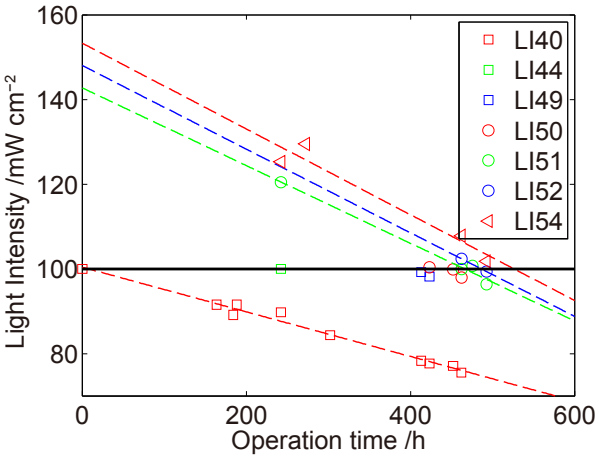

Figure 2–23 Evolution of light intensity of the solar simulator at different *LI* values. The straight lines are linear fitting curves.

2.5.2. I-V testing

Intermittent *I-V* sweepings were conducted with the programmed Keithley2400 SourceMeter with an aperture method. To get an accurate $P_{max,}$ enough data points are required. However, the performance of an OSC can be changed under continuous light illuminations, as the EQE of an OSC stored in the dark is higher than that of a device 'flooded' under 105 mW cm^{-2} AM1 illumination. [116]

For the shelf-stability measurements, devices were stored on the shelf either under fluorescent lamps or in the dark, and the intervals between *I-V* tests were 10 minutes initially and then exponentially increased to one month after decades of tests. Setting of the Keithley2400 SourceMeter was: -0.1—0.6 V voltage sweeping, 281 points with a decay time of 100 ms. In a normal case, the cell being tested was pre-irradiated under the simulated solar light for about five seconds before the *I-V* test was executed. The total irradiation time for each test was around 35 s.

2.5.3. Aperture method

The directly measured current was converted to the current density by dividing the measured current with the irradiated area. It has been noticed that the irradiated area outside the overlapping area (the so-called active area) via wave-guiding or lateral charge transport to the electrodes may contribute to the total photocurrent. This might lead to a falsely inflating photocurrent density. [69] It is thereby suggestive to irradiate one part of the active area with an aperture with a smaller area that can be measured accurately.

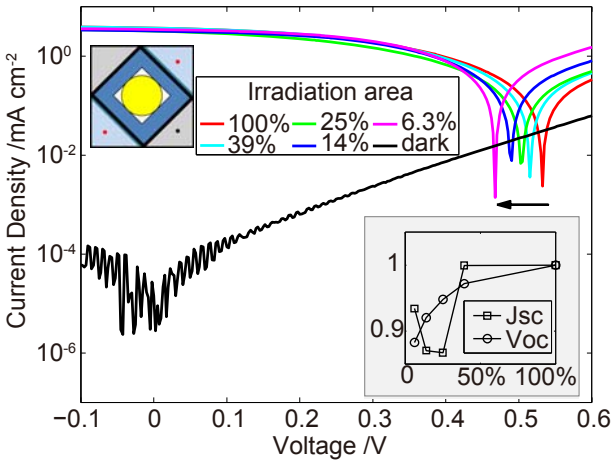

Figure 2–24 Shift of J-V curves of an encapsulated OSC with the reduction of the irradiated size. Note that the dark current density surpasses the photo current density at the voltage approaching V_{OC}; the lower-right inset shows the aperture-size dependent tested parameters. The upper-left inset is a diagram of an OSC with its active area dark-blue colored. The contacted circle and square in the center stand for the irradiated parts for OSC-Ds and OSC-Es, respectively. Three dots represent the positions of fixing probes.

The aperture method can prevent not only the possible inflation of measurements, but also possible perturbations due to impurities diffused from edges during the extrinsic degradation tests in air. For the light-induced degradation tests, devices with an active area of 1.05 cm^2 were tested with such an aperture method.

However, two problems arise at the same time. One is that the dark current through peripheral unilluminated areas becomes significant at the voltage approaching V_{OC} (Figure 2–24), which will inevitably shift the illuminated *J-V* curve. Therefore, the V_{OC}

tested with an aperture method is always lowered, by an amount depending on the size ratio between the aperture and the total active area. Another problem is caused by the spatially various degradation rates. [124] This latter problem was simply circumvented by fixing the cell, leaving an identical central part irradiated every time.

2.6. Weathering

To check the stability of devices under continuous irradiation, two bilayer-cathode cells (discussed in Chapter 5) were subjected to periodic weathering tests in air. During each 6.3 h weathering cycle, the cells were continuously irradiated with the HAL-C100 solar simulator (simulated AM 1.5G, 100—110 mW cm^{-2}) and tracked at maximum power points (MPPs) with the programmed Keithley2400 SourceMeter. Monitored yet uncontrolled ambient temperatures and relative humidity (RH) were 24 ± 5 °C and 60 ± 20 %, respectively. Ten cycles at room temperature, followed by six cycles at a higher temperature were executed for each cell over two months. Then we did two weathering tests at room temperature for each, to confirm the recovering capability. In each cycle, the tested cell was tracked at MPPs during the 6.3 h of 1-sun irradiation. *J-V* sweeps were repeated every five minutes to track the MPPs. During the idle periods, the cells were open circuited in air under fluorescent lamps.

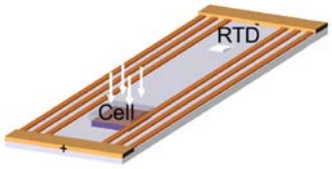

Figure 2–25 schematic diagram of the weathering test setup; parallel stripes represent heating sources.

For the weathering tests at a higher temperature (ISOS-L-2 [74]), the temperature at the back surface of the tested cell was controlled at 65 °C during tests, with a setup illustrated in *Figure 2*–25. Light transmittance of the transparent heating plate (a piece of glass with parallel ITO heaters) was measured to calibrate the light intensity. A resistance temperature detector (RTD) was embedded onto the heating source, to detect the temperature on the back surface of the cell.

2.7. Summary

In this chapter, background and function of each material comprising solar cells used in this study were discussed. The general device structure was ITO/PEDOT:PSS (or MoO_3)/CuPc/C_{60}/LiF(or BCP)/Al. The purification of organic materials and detailed fabrication procedures were discussed. The electric conductivity of a PEDOT:PSS film was improved by several orders of magnitude by treating with polar solvents, but these

enhancements seemed not to contribute to the photovoltaic performance of a device. Nevertheless, baking the PEDOT:PSS film could reduce the series resistance of a device.

Effects of pre-annealing on the physical properties of organic films were discussed. The pre-annealing resulted in a coarse surface which might increase the contact between CuPc and C_{60}, thereby increasing the photocurrent. The pre-annealing also increased the surface strength of the C_{60} film, which could mitigate the bombardment of aluminum during the thermal deposition. The final effect of the pre-annealing was an enhancement of crystallization of the CuPc layer, although the stacking pattern of CuPc molecules was not changed, i.e. approximately 63^{o} tilted on the substrate surface.

Several thin film characterization techniques used to measure properties of organic films were discussed. These properties included the thickness, the sheet resistivity, the crystallization form, the UV-visible absorption, the surface morphology, and the elemental depth profiles.

I-V tests of organic solar cells using an aperture method were also discussed. Three different light sources were discussed. We noticed that the measured V_{OC} using an aperture method was always less than the 'actual' value measured with a whole-area-irradiated method. We attributed this decrease to the dark current flowing in the unilluminated area.

In the final section of this chapter, we described a weathering setup used in Chapter 5. It was designed to test the weathering stability of bilayer-cathode devices. It had a transparent window and could control the temperature on the back surface of a weathering tested cell.[Manual chapter break]

Chapter 3. Light induced degradation

3.1. Introduction

Fullerene C_{60} is characterized not only by its high electron affinity, but also by its high affinity to oxygen. Oxygen tends to trap electrons in fullerene. And this process decreases the electric conductivity of fullerene by several orders of magnitude. The adsorption of oxygen in fullerene films can be characterized by the appearance of a new 1467 cm^{-1} Raman shift nearby the original 1458 cm^{-1} Raman shift (A_g mode of C_{60}). And this new Raman shift cannot be completely removed by heating in vacuum, but can be completely removed by laser irradiation at 514.5 nm in vacuum. [125]

The fact that the adsorption of oxygen in fullerene cannot be completely reversed by heating, but can be reversed by light irradiation in vacuum suggests that either a chemical adsorption or a deep intercalation confines some oxygen molecules in fullerene with a threshold energy beyond the thermal energy (decades of meV). Rao et al. find that the adsorption of oxygen on fullerene is physisorption and light irradiation accelerate the diffusion of oxygen in fullerene 10 times. [94, 126]

Jaime and Regueiro show that the electric conductivity of fullerene exposed in air drops with the increase of temperature. The incorporation of oxygen in a fullerene film causes a reversible decrease of its electric conductivity as well as an increase of its mass. [127] The oxygen absorption in fullerene has been shown to be reversible and be saturated at a 50% occupation of the octahedral sites.

Photo-assisted reaction of oxygen and fullerene has also been evidenced in literature. Smalley et al. show that although fullerene is intrinsically stable under light irradiation in vacuum, it reacts with O_2 under light irradiation, producing CO, CO_2, carbonyl-like bonding configurations and an amorphous carbon residue. [128]

In this chapter, we discuss the effects of light irradiation on the degradation of unencapsulated organic solar cells in which fullerene was used as the acceptors. The effects of different spectra on devices at different degradation stages are discussed.

3.2. Degradation under fluorescent lamps

In a typical procedure, a device with a 1.05 × 1.0 cm^2 active area with a structure of ITO (150 nm)/PEDOT: PSS (60 nm) /CuPc (25 nm)/C_{60} (40 nm)/LiF (2 nm)/Al (75 nm) was fabricated. Intermittent *I-V* tests were then conducted with the programmed Keithley2400 SourceMeter using the aperture method, under a 100 W halogen lamp with a total irradiance of 80 mW cm^{-2} (spectra shown in Figure 2–21 in Chapter 2) on the surface of the cell.

Timing was started when the cell began to be exposed to air. Between the intermittent testing, the cell was open circuited at room temperature (around 21 °C), either exposed under fluorescent lamps (OSC-E) or in the dark (OSC-D). The radiation intensity of the fluorescent lamps in the testing room was estimated to be approximately 1 mw cm^{-2} on the surfaces of cells. The tested areas were 0.36 cm^2 and 0.28 cm^2 for OSC-Es and OSC-Ds respectively, less than half of the total active area.

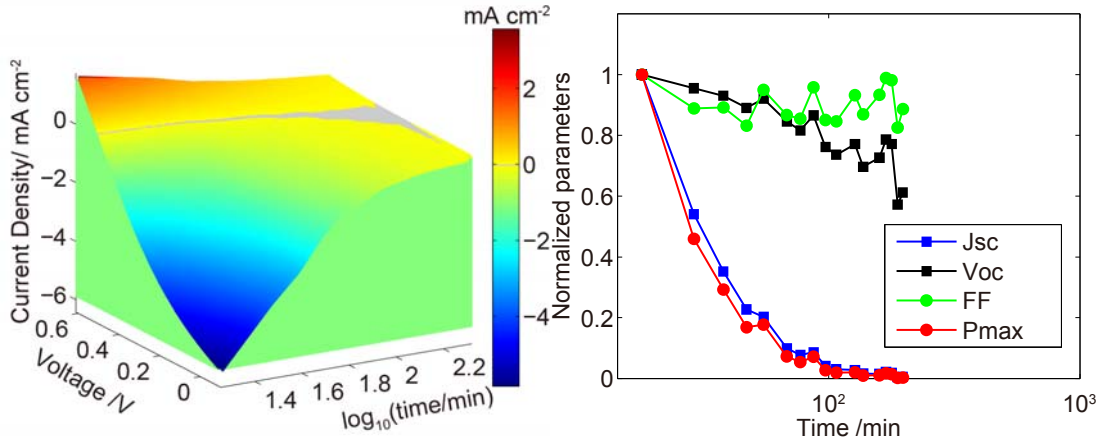

Figure 3–1 (left) J-V-time valley of an OSC-E that is exposed to the air under several fluorescent lamps between tests. (Right) Normalized parameters of the OSC-E on the left.

Normally, the unencapsulated devices degraded rapidly in the initial hours, resulting that the degradation curves were usually abnormally steep as shown on the right of Figure *3*–1. The stability of unpackaged organic solar cells depends on a number of factors, including the temperature [129] and the ambient humidity [47], etc. Although it is hard to attribute any single factor to these steep curves, it could be shown that the irradiation from the fluorescent lamps did play a role in it.

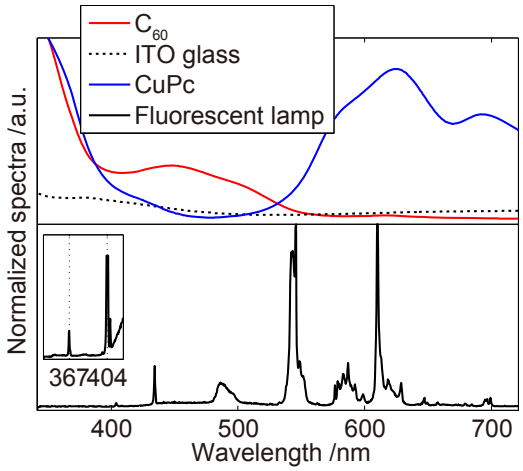

Figure 3–2 (top) absorption spectra of ITO, CuPc and fullerene on glass substrates; (bottom) radiation spectra of the lighting fluorescent lamps. The inset shows the corresponding zoomed spectra at the near-UV region.

Both the halogen lamps and the fluorescent lamps radiate light involving some near-ultraviolet light (typically at 365 nm for the latter). As the usual ITO glass substrate has a 20% absorbance at this region, the UV light emitted from both lamps could reach the organic layers effortlessly, which might damage the unsaturated photoactive compounds.

3.3. Degradation in the dark

Some devices were set into a dark box (Figure *3*–3), which held each cell on a fixed position by three retractable probes with inner springs (RS contact probes). One practical function of such a fixed test is that it could prevent the aluminum cathodes from being badly pierced by the testing probes. At the same time, it ensured that each test was taken from an identical area, eliminating deviations caused by the varied degradation rates at different parts of a cell. The inner humidity and oxygen concentration were approximately the same as these of the ambient atmosphere. Besides, both UV and visible light were negligible inside the box.

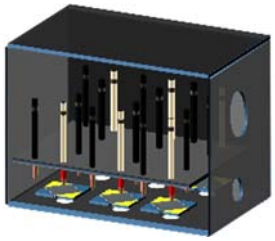

Figure 3–3 Simplified schematic diagram of the fixing box for solar cell testing whose front panel is not shown. The upper and lower holes in the side panel are for cables and ventilation, respectively. The vertical pillars are probes, and the squares under them are cells. Incident light is confined by the circular holes (Φ6 mm) beneath the cells.

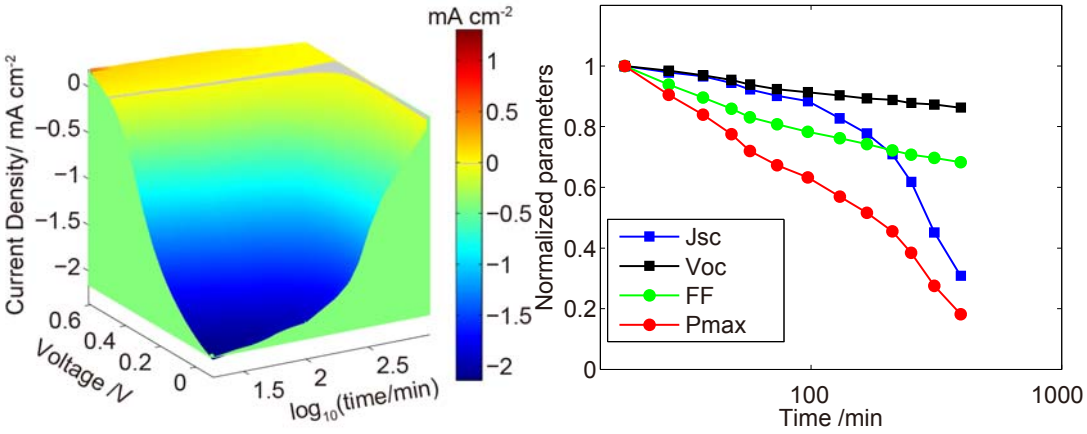

Figure 3–4 (left) J-V-time valley of an OSC-D. (Right) Normalized parameters of the OSC-D.

Almost all devices stored in the dark box degraded relatively slowly initially, generating degradation curves with near-horizontal slopes in the first several hours (Figure *3*–4). The

tested size of a cell stored in the dark is about 22% smaller than the normally tested size.

Peripheral diffusion induced degradation has been indicated by the regional degradation mapping or the size dependent degradation study. [88, 124] However, the peripheral diffusion of oxygen in OSCs has been proven to be negligible using labeled ^{18}O. [130, 131] The divergence between the OSC-D and OSC-E was presumably caused by the light irradiation from the fluorescent lamps, rather than the divergence between tested areas.

The half-shelf-lives of unencapsulated OSCs fabricated with the same procedures varied from several minutes to several days. To eliminate such deviations, we chose 11 OSC-Ds and 20 OSC-Es with PCE higher than 0.1% (tested under a halogen lamp, 80 mW cm^{-2}, spectra shown in Figure 2–21 in Chapter 2) to compare the average degradation rates. These devices had the same stacking structure. The statistical results are shown in Figure 3–5. On average, OSC-Ds degraded slower than OSC-Es.

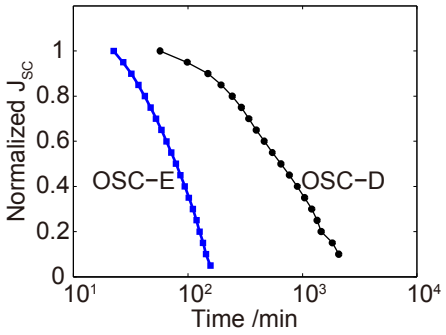

Figure 3–5 Normalized evolutions of J_{SC} averaged over 20 OSC-Es and 11 OSC-Ds with the same structure. Linear interpolation was used to average J_{SC} over the whole time span.

In order to probe the effects of light irradiation on the degradation of organic solar cells, we then checked the effects of UV light irradiation on the transmittance of organic films in air and in vacuum.

3.4. UV light induced transmittance difference

A cell with a structure of ITO/PEDOT:PSS/CuPc(25 nm)/C_{60}(40 nm) was fabricated as normal, and then it was transferred into an Ar glove box and set into a portable vacuum chamber. UV-visible transmittance was then measured through transparent quartz windows of the vacuum chamber after different periods of UV irradiation through the window. The chamber was pumped with a TMP. The UV lamp had an irradiance of about 0.5 mW cm^{-2} on the surface of the cell.

The spectrophotometer has a time-dependent response. To eliminate such a machine response deviation, transmittance at 539 nm of the initial curve (the curve measured in Ar before pumping) was used as the reference point to unify other spectra. This wavelength was chosen because both CuPc and C_{60} have weak absorptions at this wavelength.

The results shown in Figure 3–6 suggest that UV illumination in vacuum caused organic films to become more transparent to visible light, probably by removing adsorbed gas from organic films. These results further suggest that the UV light accelerates the diffusion of air in organic films.

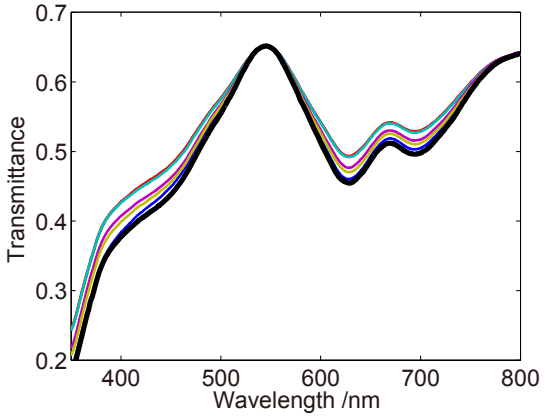

Figure 3–6 Transmittance of a cell without cathode upon UV treatments. The initial transmittance measured in Ar corresponds to the thick black curve.

3.5. Effects of light in air

3.5.1. Unencapsulated OSC

We then investigated the effects of irradiation on an unencapsulated cell with two different light sources. The cell had an initial performance as following, J_{SC} of 0.12 mA cm^{-2}, V_{OC} of 0.47 V, *FF* of 0.2 and PCE of 0.02%. We chose this cell because it degraded at a rate less than 0.34% per hour in the dark when it was used in this experiment. This means that the degradation in the experimental period lasting five hours should be less than 2%. In other words, we considered it as a 'stabilized' device.

We used two light sources, i.e. a 365 nm UV lamp (spectra is shown in the right inset of Figure *3*–7), and a halogen lamp with a UV-cutoff filter cutting off short-wavelength light from 550 nm (called UV-off light hereinafter, spectra is shown in the left inset of Figure *3*–7). Irradiation intensities were adjusted to be the same, approximately 0.7 mW cm^{-2}. Both cells had been 'stabilized' over at least one month to reduce the intrinsic degradation in the experimental period. We probed the evolution of J_{SC} and V_{OC} after different periods of UV irradiation. The results are shown in Figure *3*–7.

After the irradiation, J_{SC} rebounded completely for the UV-off irradiation and partly for the UV irradiation after in the dark for two hours. On the other hand, V_{OC} was hardly recovered after the UV irradiation even after back to dark. *FF* did not change after the irradiation.

At an open-circuit condition, J_{SC} decreased about 20% per hour after the UV irradiation,

and about 10% per hour after the UV-off irradiation. V_{OC} decreased notably by 0.02 V per hour after the UV irradiation, but unchanged after the UV-off irradiation.

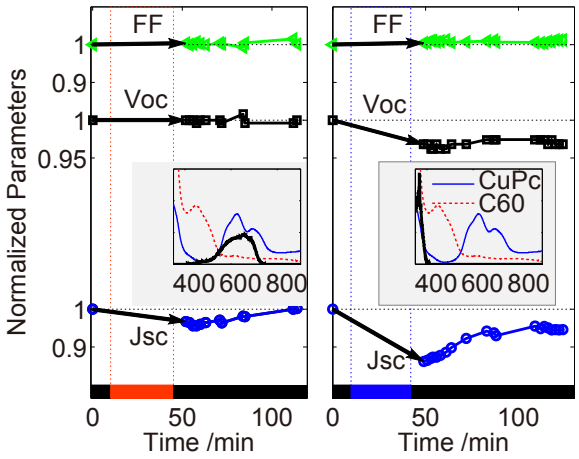

Figure 3–7 Evolutions of the normalized parameters of an unencapsulated OSC-D after irradiation. Insets are the wavelength dependent energy distributions of light sources (in nm), as well as the absorbance of CuPc and C_{60}. Bottom bars correspond to the related colors of light sources, black means in the dark.

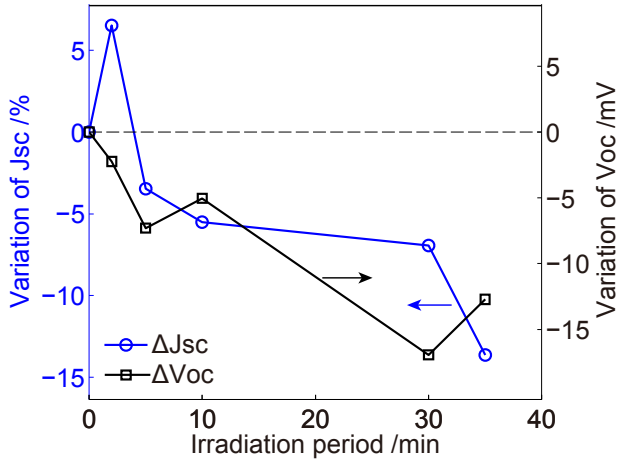

Figure 3–8 Variations of the V_{OC} and J_{SC} of the unencapsulated solar cell after different periods of low UV light irradiation.

These results suggest that the UV irradiation irreversibly changed the energy bands of active materials. On the other hand, the long-wavelength light that was only absorbed by CuPc, did not cause such an irreversible degradation. These results tell us that the light absorbed in the fullerene layer resulted in irreversible degradation in OSCs.

There are at least two adverse effects of UV light on fullerene. One is causing the photochemical degradation of fullerene, [132] which was probably related with the formation of the singlet oxygen molecule whose energy level is 0.98 eV higher (absolute value) than a normal triplet oxygen molecule. [133, 134] Another effect is an acceleration of diffusion of oxygen molecules in fullerene. Both processes could no doubt deteriorate the electronic properties of the fullerene layer. And in either case, oxygen plays an

indispensable role in the light-induced degradation of the fullerene layer. The effect of oxygen on the degradation can be evidenced in the next sections.

3.5.2. Encapsulated OSC

We used an encapsulated OSC to examine the effects of low light irradiation on the degradation of organic solar cells. This device had also reached its 'stabilized' stage with a negligible degradation rate of < 0.01% per hour. The solar cell was considered to have consumed all the air pre-adsorbed in it. The results are shown in Figure *3*–9.

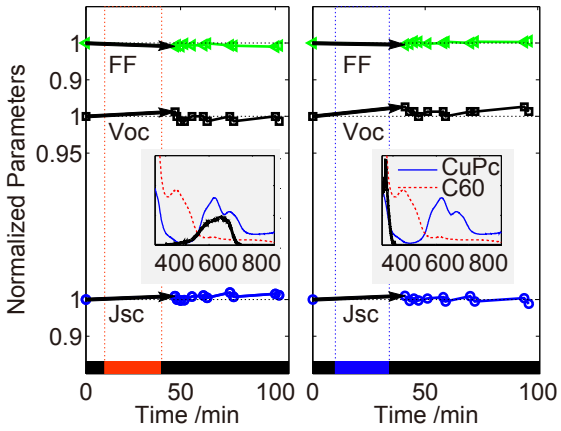

Figure 3–9 Evolutions of the normalized parameters of an encapsulated OSC-D after different irradiation. Insets show the wavelength dependent energy distributions of the light sources (in nm), as well as the absorbance of CuPc and C_{60}. Bottom bars correspond to the related colors of light sources, black means in the dark.

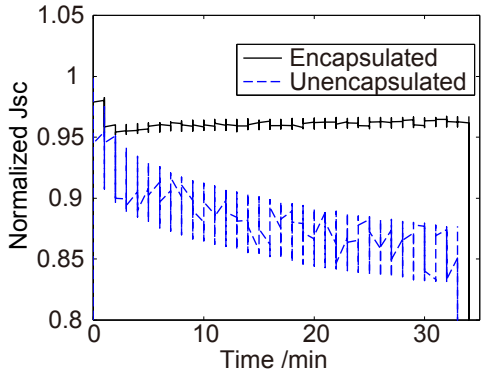

Figure 3–10 Normalized J_{SC} of an encapsulated cell (black solid) and an unencapsulated cell (blue dashed) under 0.7 mW cm^{-2} UV-off irradiation in 35 min.

Neither V_{OC} nor J_{SC} was influenced by either irradiation. We further measured J_{SC} of both the unencapsulated device and the encapsulated device under the low UV-off irradiation. The low light irradiation had little effect on the J_{SC} of the encapsulated device, whereas it continuously decreased J_{SC} of the unencapsulated device, as shown in Figure *3*–10.

Comparing the above results, we inferred that the UV light and oxygen played a synergistic effect on the degradation of organic solar cells.

3.6. Effect of light in vacuum

In order to probe the effect of short-wavelength light irradiation on the degradation of organic solar cells, we carried out other three series of experiments with two solar cells that were stored in vacuum. The vacuum chamber was the same as the one used for probing the in situ transmittance. After removing the air surrounding the tested cells, we examined the effects of air on the degradation of small-molecular organic solar cells at different degradation stages under intense light irradiation.

3.6.1. Fresh OSC

In the first series, an organic solar cell with a structure of ITO (150 nm)/PEDOT:PSS (60 nm)/CuPc (25 nm)/C_{60} (40 nm)/LiF (1.1 nm)/Al (75 nm) was fabricated as normal. After fabrication, we transferred it into a portable vacuum chamber in Ar and then pumped the chamber with a TMP to remove the surrounding Ar before the cell was exposed to light.

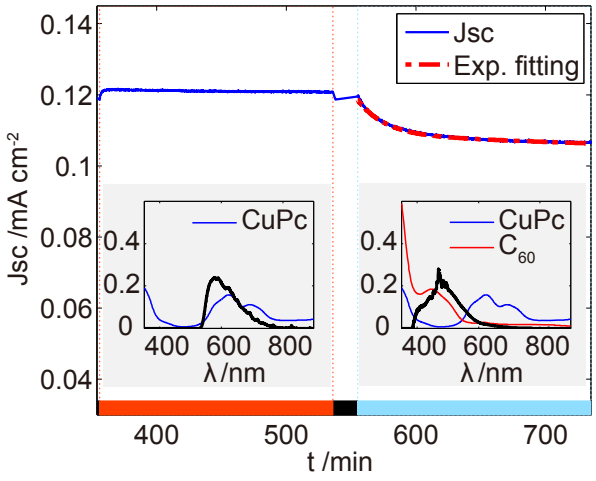

Figure 3–11 Evolution of J_{SC} of a fabricated OSC stored in vacuum under different light irradiation conditions. The dashed curve is an exponential decay fitting curve. Insets show the light spectra (black), as well as the absorbance of CuPc (blue) and C_{60} (red).

After six hours of pumping in the dark, we speculated that the gas in the chamber had been removed completely. Then we tested the performance of the device under different light irradiation. The light sources were an IR-cutoff Xe lamp with different colorfilters. A red-cutoff filter at 580 nm was used to generate the short-wavelength light and a blue-cutoff filter cutoff at 550 nm was used to generate the long-wavelength light. Both light sources had the same irradiance of about 37 mW cm^{-2} on the surface of the tested cell.

The light intensity distributions are shown in the inset of Figure 3–11.

In the first experiment lasting two hours, the red-color light source corresponding to the absorbance of CuPc was used to irradiate the cell stored in the chamber. The cell was short-circuited during the irradiation. The recorded J_{SC} is shown on the left of Figure 3–11. The cell did not noticeably degrade under this irradiation, except an initial increase probably due to a thermal effect.

This suggests that the long-wavelength light had almost no effect on the degradation of a fresh cell. More precisely, the light-induced degradation in a freshly fabricated OSC occurred neither inside nor at the interfaces of the donor material CuPc.

After the cell cooled down in the dark in the following half an hour, we used the blue-color light source to radiate the cell in the next two hours. CuPc and C_{60} can absorb this light. The evolution of recorded J_{SC} is shown on the right of Figure 3–11. Under this irradiation, the initial J_{SC} was close to that obtained under the red color. However, it decreased exponentially this time.

Inferring from these results, we proposed that the light-induced degradation in small-molecular organic solar cells occurred either inside the donor layer or at the cathode-acceptor interface. In other words, the degradation of fullerene was the main cause of the light induced degradation. To confirm this conclusion, we chose another solar cell with a different structure to investigate the light-induced degradation.

3.6.2. Air-contaminated OSC

We carried out two other series of vacuum experiments with more complicated procedures. In these two series, we replaced LiF with TiO_x. The partially oxidized titanium layer was prepared by depositing metal titanium (2 nm) upon organic (C_{60}) layers. This ultrathin metal layer was then exposed in air for about 10 s before being annealed on a 150 ^{o}C hot plate for 5 min in Ar.

The spatial distribution and chemical composition of the oxide layer were unclear. Referring to the discussion in Chapter 5, titanium atoms prefer to form clusters on the surface of fullerene, and the ultrathin titanium film could have been oxidized during the transfer in air. Upon annealing, these oxidized clusters probably migrated into the grain-boundaries of the fullerene film.

The aluminum cathode was deposited in the bell-shape chamber. The final structure of the solar cells was ITO (150 nm)/PEDOT:PSS (60 nm)/CuPc (25 nm)/C_{60} (40 nm)/TiO_x (~2 nm)/Al (75 nm). *J-V* curves of this device in the initial 40 minutes in air were recorded under a Xe lamp (95 mW cm^{-2}, spectra shown in Figure 2–21 in Chapter 2). The results are shown in Figure *3*–12.

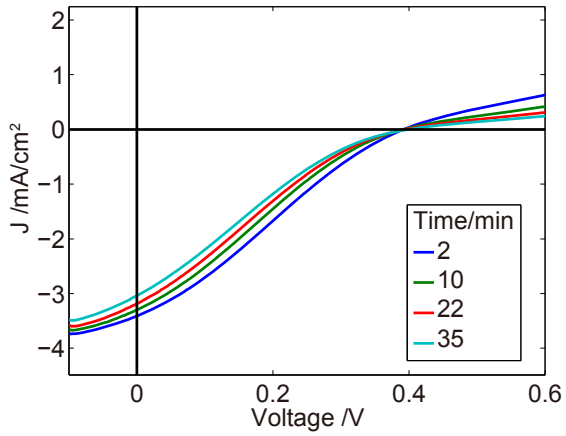

Figure 3–12 *J-V* curves of the solar cell with TiO_x as the ETL, before being set into vacuum.

This cell degraded rapidly in air, similarly to those with other ETLs. This suggests that the devices 'inhaled' air quickly. Detailed discussion on the shelf stability of these cells is in Chapter 5.

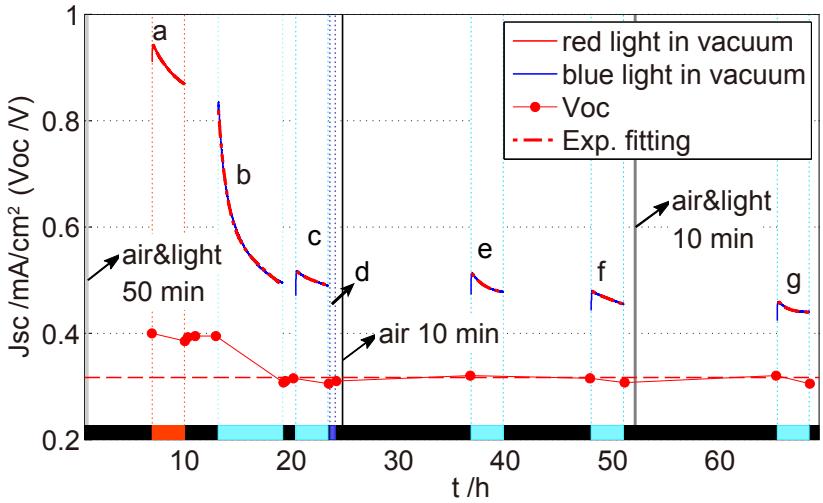

Figure 3–13 Evolution of J_{SC} and V_{OC} of the OSC in vacuum, after the *J-V* tests in Figure 3–12. Three different light sources were used, including the red-color irradiation for 3 h (a), the UV light for 30 min (d), and the blue-color irradiation for 18 h (b, c, e, f and g). The device was temporarily exposed to air before e and g. The evolution of V_{OC} intermittently measured under the red-color irradiation is also shown. Exponential fitting curves of the evolution of J_{SC} during continuous irradiation are also shown.

After intermittently testing the *J-V* curves in air for 40 min, we set this cell into the vacuum chamber to examine the stability of this air-contaminated solar cell under different light irradiation conditions. We used the same light sources as those used in Figure *3*–11. Two series, i.e. one tested at a relatively fresh stage, and one tested at a stabilized stage (stabilized in vacuum) were done. Results of the first series are shown in Figure *3*–13(a--g).

Figure 3–13 shows that the continuous red-color irradiation led to a decrease of J_{SC} (a). We explained the divergence between this result and that shown in *Figure 3*–11 with the 'inertia' of the extrinsic degradation from the initial air-exposed degradation period shown in Figure 3–12. The red-color irradiation did not decrease V_{OC}. On the contrary, the continuous blue-color irradiation seriously damaged both V_{OC} and J_{SC} (b), before the cell was 'photo-stabilized' (c).

The stabilized cell was resistant to short-wavelength light irradiation, including the 365 nm UV light (d). We inferred that there is equilibrium inside the cell after the photo-induced degradation. However, such an equilibrium state would be broken by further exposure to air, as evidenced by the slight drops of J_{SC} from period e to f and from period f to g. Nevertheless, V_{OC} was little influenced by these short-term air-exposures.

3.6.3. Stabilized OSC

After the tests shown in *Figure 3*–13, we stored the cell to an Ar glove box in the following one week, and then did the second series of tests on this 'stabilized' cell. The cell recovered its performance to some degree in Ar (less than 10%). In this second series (A—J in *Figure 3*–14), we first exposed the cell in air for two hours to inhale air under low red-color irradiation (≤ 0.5 mW cm^{-2}), and then tested its performance under continuous blue-color irradiation in vacuum (B). After that, the cell was stored in air, and tested under continuous red-color irradiation (C), continuous blue-color irradiation (D and E), and continuous white irradiation (F) in sequence.

The blue-color irradiation first decreased the V_{OC} of the cell to another 'stabilized' level (B). However, J_{SC} of the V_{OC}-stabilized cell was still susceptible to blue-color irradiation, as indicated by the results either in air (D and E) or in vacuum (H, I and J).

The red-color irradiation did not cause any degradation of the 'stabilized' cell either in air (C) or in vacuum (G). Another interesting phenomenon is that the red-color irradiation in vacuum (G) probably caused a recovery of the cell. However, this recovery was only temporary, as the sequential blue-color irradiation (H) brought the performance irreversibly down to the third stabilized level in vacuum (I and J).

The white-color irradiation (49 mW cm^{-2}) was generated with the same IR-cutoff Xe lamp but with an extra neutral density filter (50% visible transmittance) and a glass slide (92% visible transmittance). Although this white-color irradiation constituted blue light, it seemed to have enhanced the performance of the cell in air (F). However, without reference measurement under the same light irradiation, we cannot estimate the effect of this white-color irradiation.

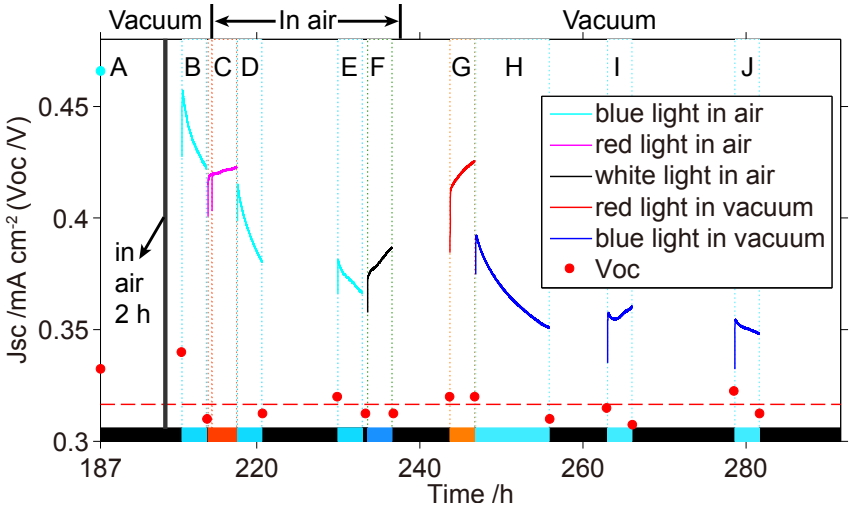

Figure 3–14 Evolution of J_{SC} and V_{OC} of the OSC after the tests in Figure 3–13. The time axes are consecutive. Three different light sources were used, including red-color irradiation in air for 3.5 h (C), or in vacuum for 3 h (G), white irradiation in air for 3 h (F), and blue-color irradiation in air for 6 h (D and E) or in vacuum for 15 h (B, H, I and J). The cell was temporarily exposed to air before B. V_{OC} intermittently measured under the red-color irradiation is also shown (red dots) with the average V_{OC} (dashed horizontal line).

The above results indicate that an organic solar cell inhaled air when it was exposed in air. The rate of the oxygen inhalation increased with the freshness of the cell. There existed equilibrium states under which neither UV irradiation nor blue-color irradiation could cause irreversible degradation of the cell in vacuum. These equilibrium states only existed after the cell had experienced photo-induced degradation. The equilibrium state was probably related with the removal of the remaining air inside the cell under blue-color light irradiation. These equilibrium states were susceptible to further air exposure. If the stabilized cell was exposed in air again, it inhaled air, and reached another equilibrium state after consuming the inhaled air under blue-color irradiation in vacuum. Referring to the light-induced acceleration of diffusion of oxygen in fullerene, we conclude that the photo-induced degradation in small-molecular organic solar cells originates from the synergistic deteriorating effects of oxygen and light irradiation on the electronic properties of the acceptor material fullerene.

3.7. Summary

In this chapter, we discussed the synergistic effects of light and air (oxygen) on the extrinsic degradation of small-molecular organic solar cells. The lighting fluorescent lamps with a low irradiance caused an acceleration of the degradation of unencapsulated organic solar cells in air. On average, the fluorescent lamps increase the degradation rate sevenfold.

We compared the effects of two different low light irradiation conditions on one

encapsulated and one unencapsulated solar cells in air. We found that for the unencapsulated cell, both irradiation caused reversible degradation, while the UV irradiation further caused irreversible degradation. On the contrary, for the encapsulated solar cell, neither of the low light irradiation caused degradation. We concluded that although the CuPc layer did not degrade under light irradiation, the fullerene layer was degraded under light irradiation in air.

We probed the effect of different intense light irradiation conditions on the degradation of organic solar cells stored in vacuum. A fresh solar cell in vacuum resisted red-color irradiation, whereas it did not resist blue-color irradiation in vacuum.

The effects of different light irradiation conditions on the degradation of a photo-stabilized solar cell in vacuum were also probed. We found that a cell stored in vacuum could reach an equilibrium state. However, this equilibrium state would be broken by further inhalation of air. We concluded that air and light play a synergistic role in the degradation of small-molecular organic solar cells.

Table 4 Summary of degradation patterns under different spectra, with different amount of air, of devices under different degradation stages.

OSC Stage		Fresh				Stabilized*				
Intensity & Spectra	Low light (<1.0 mW cm^{-2})	D	A+B+ C**			A→D	C→D	A		C
	Strong light (>20 mW cm^{-2})			C	B				B	
Air ***		P	P	T	T	P	P	T	P	T
Normalized J_{SC}-t										
λ		A (365nm)	B (500nm)		C (620nm)		D (dark)			

* Normal light irradiation no longer causes degradation;

** Fluorescent lamps;

*** P: plenty amount; T: trace amount

The effects of different spectra we investigated in this chapter are summarized in Table 4. From it, at least three processes are evidenced:

- Light independent extrinsic degradation;

- Light dependent reversible degradation;
- Short-wavelength light dependent irreversible degradation.

Chapter 4. Modelling of degradation curves

4.1. Introduction

Building a simple model to explain experimental observations is one of the powerful ways to improve our understanding of variables that are involved in a complicated system. A proper model of a dynamic process also makes it possible for us to predict the evolution of an observable.

Organic solar cells degrade in various ways as mentioned in the introduction chapter. Short-circuit current (I_{SC}), proportional to the rate of electron transportation between layer interfaces, is widely used to represent a cell's real-time quality. Exponential polynomials have generally been postulated to be the decay equation of I_{SC}, either on the shelf or under continuous irradiation.

For devices stored on the shelf, a single exponential equation has been employed for curve fitting. [135] A single exponential expression fails to depict the evolution of I_{SC} of a device exposed under continuous light irradiation. Under the continuous irradiation, an OSC usually degrades exponentially at first but then either degrades slowly or becomes photo-stabilized. In this case, Equation 4-1 and 4-3 are employed to describe the performance.

Krebs et al. fabricated polymer-C_{60} based cells with an area of 3 cm^2 and fitted the evolution of I_{SC} as a function of time with a double-term exponential expression (Equation 4-1) corresponding to an initially fast decay and a sequentially slow decay. [136] The integrated charge Q_{total} can be estimated according to Equation 4-2.

$$I_{\mathrm{SC}} = ae^{-bt} + ce^{-dt} \tag{4-1}$$

$$Q_{\mathrm{total}} = \frac{a}{b} + \frac{c}{d} \tag{4-2}$$

A stretched exponential relationship between I_{SC} and t (Equation 4-3) has also been employed. [52, 137] The half-life of a device $t_{1/2}$ can be estimated according to Equation 4-4.

$$I_{\mathrm{SC}} = I_{\mathrm{SC\ (t=0)}} \exp\left[-\left(\frac{t}{\tau}\right)^{\beta}\right] \tag{4-3}$$

$$t_{1/2} = \tau(\ln 2)^{1/\beta} \tag{4-4}$$

For the mechanisms of the extrinsic degradation in OSCs, oxygen and water have been believed to be two main causes. Krebs and Norrman's group reported a long-timespan study on the degradation of OSCs, and pointed out two oxygen sources, i.e. microscopic

pinholes and in-between grain boundaries. [131] They also investigated the vertical distribution of oxygen in cells with thin aluminum cathodes of 22 nm and without any ETL, and found that oxygen diffuses into the organic layers and further oxidizes both the organic layer and the aluminum cathode under light irradiation. [95]

They further used BPhen as the ETL and 100nm of aluminum as the cathode, and found that water plays a more significant effect on the degradation of fabricated devices in this case. Pinholes in the aluminum cathode are attributed to the oxygen intruding pathway, and grain-boundaries in the cathode to the water intruding pathway. [91] From these previous findings, we infer that the intake and also the significance of oxygen (compared to water) depends on the structure of the cathode interface as well as the thickness of the cathode.

Normally, it is hard to sketch a material degradation model for organic solar cells with diverse constitutive materials. For the small-molecular organic solar cells with a structure of ITO/PEDOT:PSS/CuPc/C_{60}/LiF/Al, Xi et al. have compared the effects of water and oxygen on the stability of unencapsulated devices and stated that oxygen plays a more crucial role in extrinsically degrading the cells. [135]

The above literature, together with the observations discussed in Chapter 3, formed the basis of modelling in this chapter. To comply with various experimental degradation curves, we built several different models to explain experimental observations from different perspectives.

4.2. Compartmentalization

The transportation of charge carriers in an OSC is driven by a vertical electric field between electrodes, [23] meaning that it is reasonable to divide each cell into numerical imaginary vertical sections (normally called compartmentalization) connected in parallel, as illustrated in Figure 4–1. For the validity of compartmentalization in OSCs, two assumptions are necessary. First, the lateral diffusion of either constituting molecules, or charge transporting species, or excitons in organic layers is omitted. Second, the influence of trapped charges on the transport of neighbouring charges is omitted. In a compartmentalized device, each section can be photovoltaic active or inactive. The active section captures and transfers photo-energy independently. A similar method has recently been used to explain experimental observations in BHJ-OSCs. [138]

The recovering of device performance discussed in Chapter 3 has suggested that there exists equilibrium in a device. It means that there are some sections which are not photoactive temporarily could be transferred to or from photo active sections. These retrievable but temporarily inhabited states cancel out part of a strain loaded on a solar cell during degradation. The strain may be light irradiation or exposure to damp (see Chapter 5), or any other factors that result in recoverable degradation in an OSC.

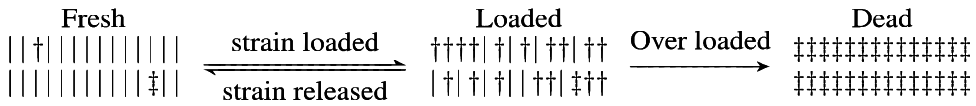

Scheme 1 Scheme of three steps during the life of an OSC.

In *Scheme 1*, we suppose that each fresh cell consists of numerous sections, including the photovoltaic active ones (|), the temporally photovoltaic inactive ones (†) and the permanently photovoltaic inactive ones (‡). The active section will turn permanently inactivated states (| ⟶ ‡) under an over-loaded strain or to the temporally active section (| ⟶ †) under a moderate strain. The temporally photovoltaic inactive section has the potential to become active († ⟶ |) if the strain is released. For the OSCs discussed in Chapter 3, the strain might be the light irradiation.

The overall photocurrent *I* flowing in the external circuit of an OSC is the sum of all the photocurrent *i* in each section, as illustrated in Figure 4–1.

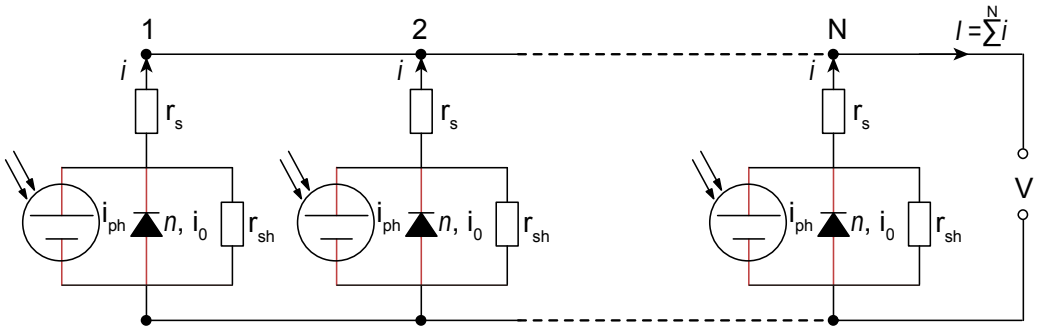

Figure 4–1 Equivalent circuit diagram of an OSC consisting of numerous nanoscale separate OSC sections connected in parallel.

4.3. Photo-chemical reaction model

4.3.1. Logistic decay

Most OSCs degraded monotonically in air, generating degradation curves that can be well fitted with an exponential decay equation having two variables, like Equaiton 4-3. However, some devices degraded moderately in the initial period, as the one shown in *Figure 4*–2 (greenish dots). After trying several common two-variable fitting equations, we found that a logistic equation (Equation 4-8) fits such a normalized J_{SC}-*t* curve better than others. We derive this equation with an abstract model in the following.

The logistic function typically stems from an autocatalysis reaction in chemistry or a dose response in pharmacology. To derive a logistic decay function for the degradation of solar cells, we suppose that the decaying rate of active sections *M* in a cell is nonlinar, following

$$\frac{dM(t)}{dt} = -kM(t)\cdot[1 - M(t)\cdot Q(t)] \qquad 4\text{-}5$$

where *k* denotes rate constant, and a parameter *Q*(*t*) is introduced to involve the possible recovery of temporal inactive sections or the possible self-accelerated degradation. To simplify Equation 4-5, we take *Q*(*t*) as constant *Q*. Solving equation 4-5, we can get

$$M(t) = \frac{1}{Ce^{kt} + Q} \qquad 4\text{-}6$$

where *C* is an arbitrary constant. If we assume the initial value of *M* at t = 0 is M_0, the specific solution becomes

$$M(t) = \frac{1}{(1/M_0 - Q)e^{kt} + Q} \qquad 4\text{-}7$$

Then the normalized short-circuit current (noted as NI_{SC}) which is proportional to the number of active sections follows

$$\mathrm{NI_{SC}}(t) = \frac{1}{(1-q)e^{kt} + q} \qquad 4\text{-}8$$

where $q = M_0Q$. The curve of Equation 4-8 at t > 0 is an inverse sigmoid curve when $0 < q < 1$ (degradation with recovery), or a steeply decaying curve when $q < 0$ (accelerated degradation). According to this model, the device's half shelf-life $t_{1/2}$ and the integrated charge Q_{total} are determined by *k* and *q*,

$$t_{1/2} = \frac{1}{k}\ln\left(1 + \frac{1}{1-q}\right) \quad \text{and} \quad Q_{\mathrm{total}} = -\frac{1}{kq}\ln(1-q) \qquad 4\text{-}9$$

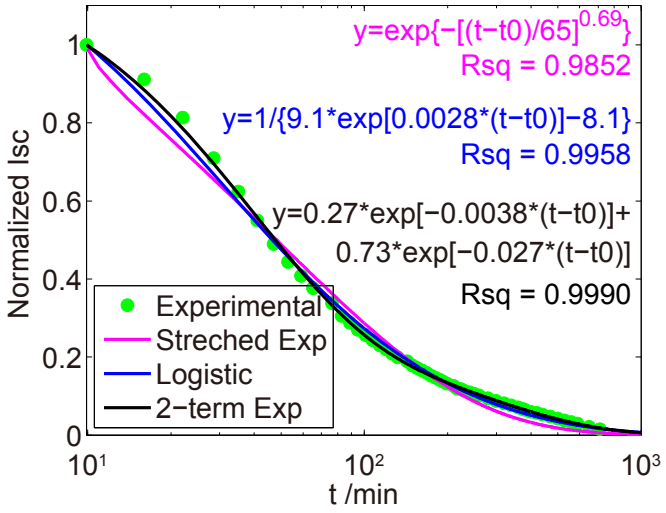

Figure 4–2 Experimental short-circuit current curves, and different fitting curves using the three models: the stretched exponential decay (magenta), the logistic decay (blue), and the double-term exponential decay (black). t0 represents the time of the first recorded point. The employed fitting expressions and related R-squares are noted beside the curves.

4.3.2. Two-term exponential decay

Performances of some devices might increase instead of decreasing in the initial period, especially for those with relatively low initial performances (*Figure 4*–3). One explanation of the initial increase is a removal of shortage spikes between electrodes in air. For such devices, the above discussed double-variable equations failed to depict their degradation curves. We need at least three variables to well depict such a degradation curve. A double-term expoential decay equation (Equation 4-1) with three variables (a + c =1) could fit the degradation curve well. We derive this equation with a material model in this section.

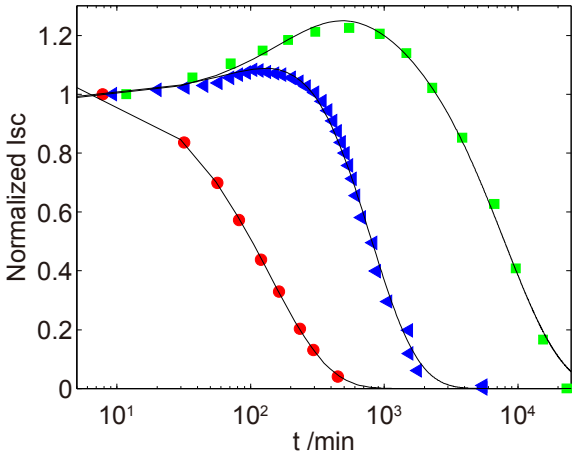

Figure 4–3 Examples of initial increases of performances of devices stored in air (blue triangles and green squares). The performance of a monotonically degrading device is also plotted as a reference (red circles). Black curves are double-term exponential fittings.

In order to sketch a material model including the recovering process as well as the UV induced permanent damage, we hypothesized that C_{60} was oxidizable by photoinduced reactions like the cycloaddition with oxygen under UV irradiation. Besides, the failure of cells due to the oxidation of aluminum was also suggested. [22] Then the degradation processes occurring nearby the cathode interface were sketched as

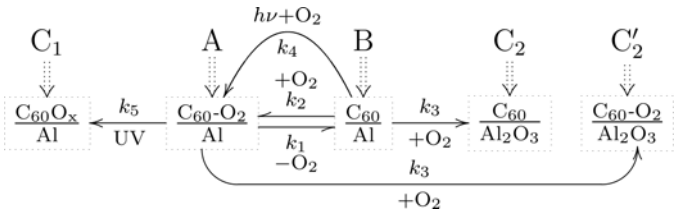

Scheme 2 Photochemical processes at the cathode interface in an OSC.

where *k*s are the rate constants of reactions. In *Scheme 2*, we classify a section into one of three types, including the (photovoltaic) active one B, the temporarily inactive one A, and the permanently inactive ones C_1, C_2, and C_3, etc. Section A can be transferred to section B by vacuum-annealing under light irradiation, and from section B in the

presence of oxygen. The effect of short-wavelength light is perhaps accelerating the oxidization of the cathode (C_2 and C_2') by speeding up the vertical diffusion of oxygen. UV light might further induce the oxidization of fullerene (C_1). [94]

We assumed that the oxygen was continuously supplied, and then put all of the irreversibly inactivated sections together as C. The concentration of free oxygen at the C_{60}/Al interface was supposed to be a constant, [O_2], while at the (O_2-C_{60})/Al interface it was reduced to [O_2]'. The rate equations were then drawn up as

$$\frac{d}{dt}[\mathrm{A}] = -(w_1 + w_3' + h_4\mathrm{D}_4)\cdot[\mathrm{A}] + (w_2 + h_2\mathrm{D}_2)\cdot[\mathrm{B}]$$
$$\frac{d}{dt}[\mathrm{B}] = w_1[\mathrm{A}] - (w_2 + w_3 + h_2\mathrm{D}_2)\cdot[\mathrm{B}]$$
$$\frac{d}{dt}[\mathrm{C}] = w_3[\mathrm{B}] + (w_3' + h_4\mathrm{D}_4)\cdot[\mathrm{A}]$$

where:

w_1 equals k_1;
w_2, w_3, and h_2 equal k_2, k_3, and k_4 multiplied by [O_2], respectively;
w_3' equals k_3 multiplied by [O_2]';
h_4 equals k_5 which is only UV light dependent;
[A] is the amount of the retrievable sections;
[B] is the amount of the active sections;
[C] is the total amount of the inactivated sections;
D_2 is the light dependent Boolean logic;
D_4 is the UV light dependent Boolean logic.

In the dark, D_2 and D_4 are zeros. The solution of [B] (proportional to I_{SC}) is in the form of a double-term exponential polynomial (Equation 4-1).

We did parameterizations to the above model. After assigning values for each parameter, we got three featured sets of curves (*Figure 4*–4). A short period of irradiation was also simulated. The values of the corresponding parameters *a, b, c* and *d* are listed in figures. The solid curves represent the amount of section B and also NI_{SC}. We further added intermittent irradiation to simulate the one minute's test with exponentially increasing intervals between tests (blue curves). The simulation shows recovery of performance after the strong light irradiation, resembling experimental results (Supporting figure 3). The red curves are the simulations for the continuously light exposure, resembling ordinarily reported curves.

One of the drawbacks of the photo-chemical model is the large flexibility of parameters. In the following section, we show how to understand the degradation curves from a diffusion perspective, using several measurable parameters.

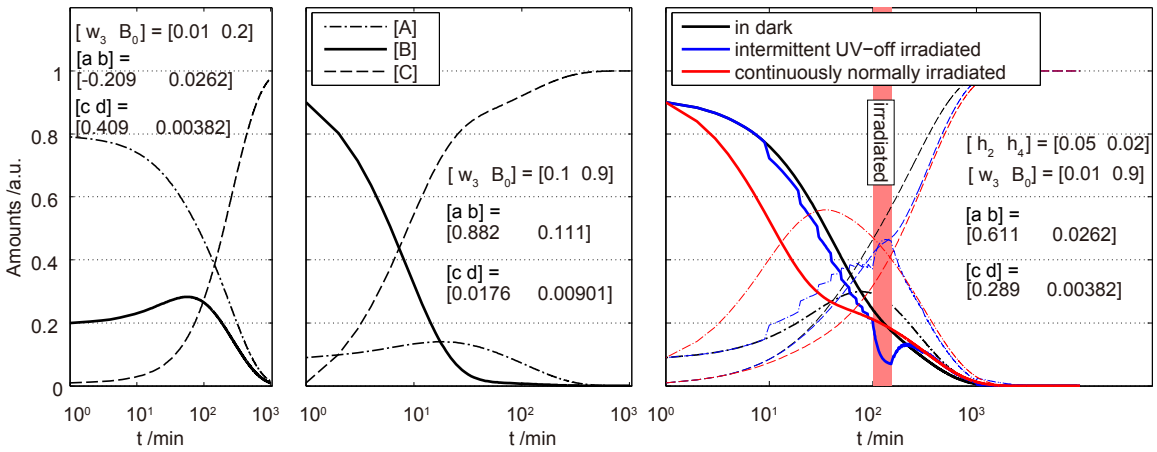

Figure 4–4 Simulations of the model with w_3' to be zero, and the number of all sections to be one. The initial parameters without dimensions are: $C_0 = 0.01$, $w_1 = 0.01$, $w_2 = 0.01$, $A_0 = 0.99 - B_0$, and $B_0 = 0.2$, $w_3 = 0.01$ (left); $B_0 = 0.9$, $w_3 = 0.1$ (middle); $B_0 = 0.9$, $w_3 = 0.01$ (right). The solid curves indicate their photovoltaic capabilities. The red column corresponds to 30 min's light irradiation with $h_2 = 0.05$.

4.4. Lateral diffusion model

4.4.1. Fick's diffusion law

Fick's laws of diffusion are generally used to quantitatively depict diffusion using a diffusion coefficient *D*. [139] The first law states that the rate of transfer of diffusing substance (diffusate) through unit area of a section is proportional to the concentration gradient normal to the section, i.e.

$$F = -D\,\partial C/\partial x \qquad 4\text{-}10$$

where *F* is the rate of transfer per unit area of section, *C* the concentration of diffusate, and *x* the space coordinate normal to the section.

The second law is derived from the first law, and it describes how diffusion causes the concentration to change with time:

$$\partial C/\partial t = \nabla \cdot D\nabla C \qquad 4\text{-}11$$

4.4.2. Peripheral diffusion from edges

Although it has been widely suggested that the air intruding from the covering cathode is the major cause of the extrinsic degradation of OSCs, [131] it has also been found that the stability of a fabricated OSC is influenced by the size of the active area. [88] Yamanari et al. compared in parallel the spatial degradation of three devices with HTL composed of

PEDOT:PSS or MoO_x or without any HTL, and found that the PEDOT:PSS device degrades preferentially from four edges of the solar cell stored in air in the dark. [124] Inspired from these reports, we simulated the lateral diffusion of air from edges of devices.

Figure *4*–5 shows the peripherally one-dimensional diffusion of air inside a square cell. The yellow regions shown in the insets represent the illuminated areas, whereas the blue regions represent the entire active areas. After time *t* the boundaries (dotted) of diffusate were approximated by the one-dimensional diffusion length, namely $2\sqrt{Dt}$. [118, 139] For a sake of simplicity, we considered *D* as a constant. The active sections were assumed to lose photo-activities immediately after encountering the intruding air.

Devices stored in the dark sometimes did not degrade in the initial period, which agrees with the simulation shown in *Figure 4*–5, a. The proportion of the initial plateau period depends on both the diffusion coefficient *D* and *R/L*, where *R* is the radius of the tested part, and *L* the distance from the center to the edge of the active area of a cell. The value of *D* was taken arbitrarily.

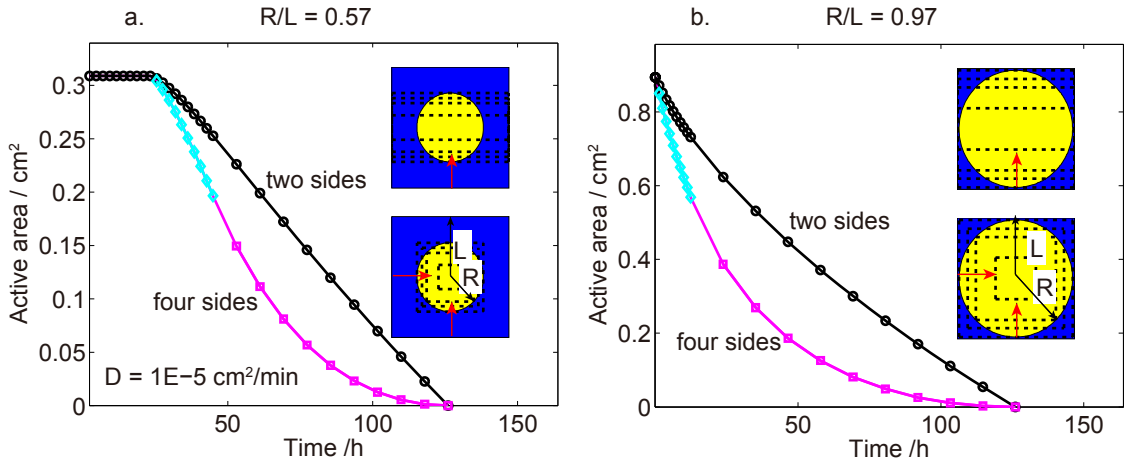

Figure 4–5 Unpolluted area of the tested region with the same diffusion coefficient; (a) a smaller tested area (yellow) and (b) a larger tested area. The side lengths of the cell were set to 1.1 cm. The dot lines denote the diffusion boundaries. The cyanic periods correspond to the periods between the exterior and interior contacts of the diffusion boundaries with the tested area.

This peripheral diffusion model gave us clues for understanding the dynamics of extrinsic degradation of OSCs, although it had some problems. First, it failed to explain the extremely long shelf-lives of PEDOT:PSS devices discussed in Chapter 5. Furthermore, the diffusion coefficient of fatal diffusate was presumed to be a constant 1×10^{-5} cm^2 s^{-1}, not complying with the pressure-dependent diffusion coefficient of gas in a polymer. [118] Finally, it did not take into account the overlapping between longitudinal diffusion and latitudinal diffusion. To solve these problems, we proposed another diffusion model as follows.

4.4.3. Pinholes and grain-boundaries

Normally, microscopic pinholes exist on the surface of fabricated OSCs. One possible origin of these pinholes is wrinkled organic layers, especially after the pre-annealing. These wrinkles could cause the formation of pinholes in a subsequently deposited cathode, and may even cause a circuit shortage [116]. When we used BCP as the ETL, no pre-annealing was done, and as a result the pinhole density was much reduced. Furthermore, we showed in Chapter 5 that these pinholes could be eliminated by an ultrathin titanium layer beneath the aluminum cathode.

The pinholes on the surface of an aluminum cathode can be observed under an optical microscope. Therefore, the pinhole density was estimated by counting the density of bright spots in the cathode under transmitted light with a Nikon OPTIPHOT-POL microscope. The exposure time of the camera was 30 s. These pinholes were also characterized with AFM (Figure 5–42 in Chapter 5).

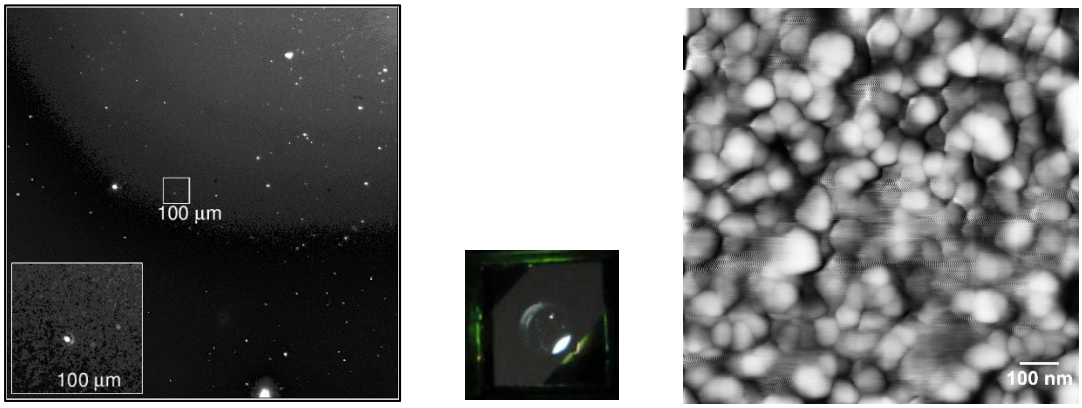

Figure 4–6 (left) microscopic image of an OSC under transmitted light, the total area is 1500 × 1500 µm^2. Each bright spot corresponds to one pinhole. One pinhole is shown in the zoomed inset. (Middle) one large pinhole visible to the naked eye.(Right) AFM image of the aluminum surface of an OSC.

Bulk aluminum is composed of numerous crystalline grains separated by grain-boundaries. These nanoscale grains are observable under a scanning electron microscope (SEM) [131] or an AFM. The average diameter of Al grains shown on the right of Figure 4–6 was estimated to be about 60 nm. The exposed grain boundaries probably have a mean width of 0.5 nm, [140] larger than the molecular diameter of either oxygen or water.

4.4.4. Lateral diffusion of oxygen

We made a simple simulation of the lateral diffusion of oxygen according to the observed different degradation patterns under different storage conditions. Sources of oxygen in-

taken by OSCs have been found to include both microscopic pinholes and in-between grain boundaries in the cathode. [131] Microscopic pinholes were randomly distributed with a minimum average distance of 50 µm (*Figure 4*–6).

An approximation by a cylindrical diffusion model [139] with the reported diffusion constant (10^{-13} cm^2 s^{-1} [141]) suggested that the lateral effective diffusion distance from a microscopic pinhole (Φ1 µm) is approximately 1.5 µm in seven hours. Such a short length compared to the average distance between pinholes implies that the diffusion through the microscopic pinholes was much less than that required by the observed degradation. In other words, the major short-term oxygen source in OSCs was probably the grainboundaries, rather than microscopic pinholes. Unfortunately, few detailed studies on the grain boundaries could be found until now. Suppose all the observed boundaries that were separated by approximately 40 nm following the SEM image reported by Krebs et al. [131] were totally permeable for oxygen, the laterally diffused oxygen from one boundary only needs approximately one minute to meet with that from its neighboring boundaries. It means that not all these boundaries are actually permeable for oxygen.

Instead, we found it convenient to consider all oxygen sources as randomly distributed submicroscopic sources, incorporating both grain boundaries which were wide enough for oxygen to pass through, and microscopic pinholes. The average distance between these imaginary submicroscopic sources should be on a micron scale according to the experimentally observed degradation rate. The oxygen distribution throughout the fullerene film at these submicroscopic sources was supposed to be uniform and maintained constant. We made such an assumption because it facilitated the boundary setting as discussed below. Besides, oxygen behaviors in other lamellar layers were not taken into account.

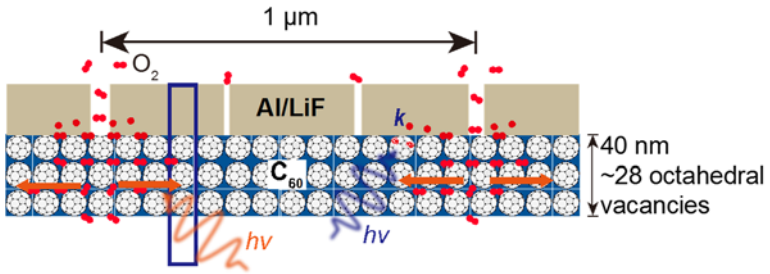

Figure 4–7 Scheme showing the lateral diffusion of oxygen in the fullerene layer. Grain-boundaries are represented with narrow gaps in the aluminum cathode, whereas pinholes, including wide graingrainboundaries, are represented with wide gaps. Oxygen molecules are represented with the peanut-shape red particles. Light (orange sinuous) accelerates the lateral diffusion of oxygen, while the short-wavelength part (blue sinuous) further causes the reaction of oxygen.

With these assumptions, the dynamical degradation finally became a two-dimensional non-steady multi-source radial diffusion problem in the fullerene film. The oxygen

diffusion is a non-steady process following the extended Fick's law:

$$\partial C/\partial t = \nabla \cdot D\nabla C - kC \qquad \text{4-12}$$

where *C* is the concentration of oxygen, *t* the time, *D* the diffusion coefficient and *k* the reaction rate constant of oxygen. Along with the diffusion of oxygen, the contaminated area becomes photo-inactivated due to the strong carrier trapping effects of oxygen in fullerene. [95, 142-144]

The analytical solution of an analogous single-source non-reaction radial diffusion problem has been solved to be [139]

$$\frac{C - C_0}{C_1 - C_0} = 1 + \frac{2}{\pi}\int_0^\infty \exp(-Du^2 t)\frac{J_0(ur)Y_0(ua) - Y_0(ur)J_0(ua)}{J_0^2(ua) + Y_0^2(ua)}\frac{du}{u} \qquad \text{4-13}$$

where *r* and *a* are the radii of the diffusate and the central source (*a* = 10 nm here), respectively, C_0 the initial concentration throughout the region $r > a$ (C_0 = 0 here), C_1 the constant concentration maintained at $r = a$ (C_1 = 1 here), and J_0 and Y_0 Bessel functions of the first and second kind respectively, of order zero.

4.4.5. Simulation

The problem is numerically solvable with Matlab® using a finite-element method (FEM). The oxygen concentration *C* is then substituted by *x* in the composition of $C_{60}(O_2)_x$. The physical meaning of *x* is the average concentration of oxygen molecules over all fullerene molecules in one vertical section. As the thickness of the fullerene layer is 40 nm, vacancies in one minimal section could maximally house 28 oxygen molecules (the *fcc* lattice constant of fullerene is 1.417 nm [101]). The boundary between alive sections and inactive sections was therefore set to $x = 1/28 \approx 0.036$, corresponding to one O_2 in one section.

Simulated evolution of J_{SC} with different values of C_1 is shown in *Figure 4*–8. According to Equation 4-13, the concentration *C* at position *r* after time *t* is proportional to C_1 (suppose C_0 to be zero). In other words, C_1/x does not vary with C_1. Consequently, we only adopted C_1 = 1 in simulations discussed hereinafter. In the two-dimensional simulation, 5 × 5 circular sources with a radius of 10 nm, separated by 1 μm, were suddenly fulfilled with oxygen from time zero when the concentration changed from zero to one.

The concentration throughout the surrounding area was initialized as zero. The FEM employs triangular meshes for calculations. Mesh refinements followed with Jiggle mesh optimizations were applied four times, limited by the computation times. After problem solved, the concentration distribution around the central source in a square of 1 × 1 μm^2 was analyzed by calculating the area enclosed by a concentration of 0.036.

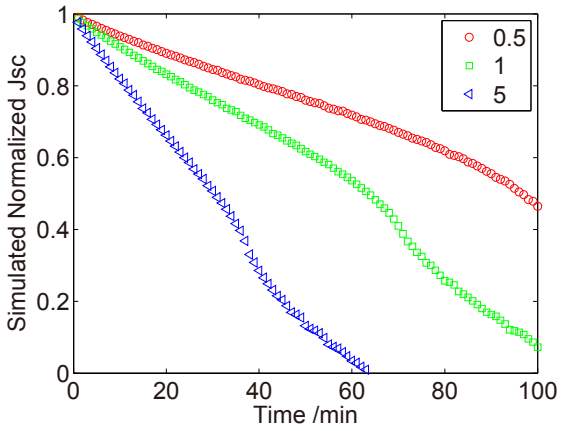

Figure 4–8 Simulated evolution of J_{SC} with three different values of C_1.

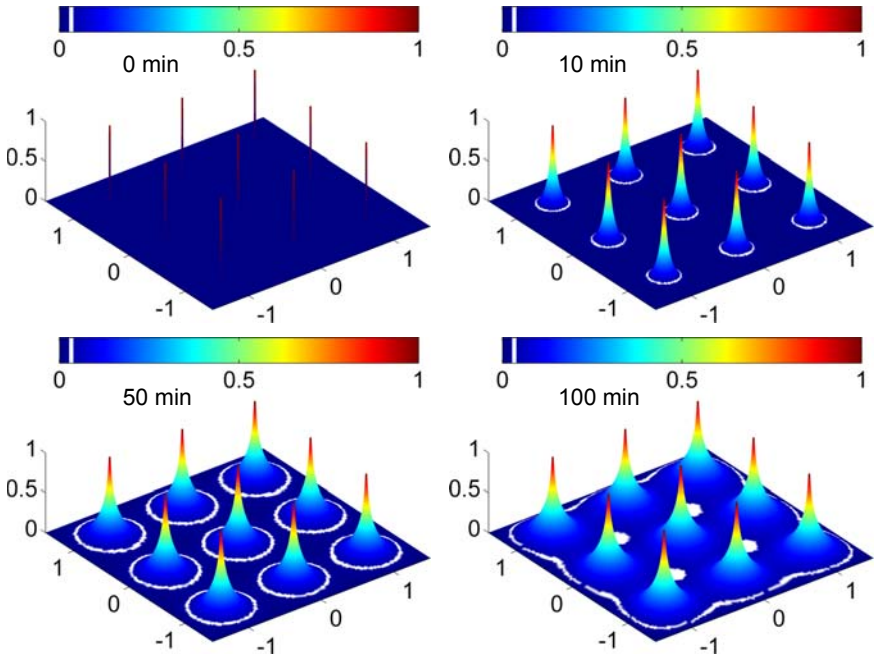

Figure 4–9 Simulated oxygen concentration x in the central 3 × 3 μm^2 area over time. The diffusion constant was set to 1 × 10^{-13} cm^2 s^{-1}. The boundary of each pinhole was set to 1. k was set to zero. The white circles were plotted at 0.036.

4.4.6. Fitting

An OSC-E and an OSC-D fabricated from an identical batch with the same initial performance were chosen for comparison. Degradation curves of both cells are linear initially [*Figure 4*–11(c)]. It agrees with the near-linear reduction of the active area in the initial lateral radial diffusion according to a single-source non-reaction simulation. Further fitting revealed that the fluorescent lamps lead to an approximately sevenfold larger diffusion constant, which is possible according to the literature. [94, 95, 126]

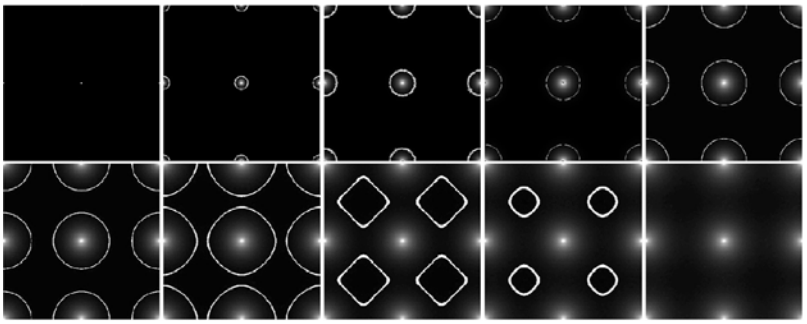

Figure 4–10 Simulated oxygen concentration in the central 2 × 2 μm^2 area of the multi-source diffusion in 100 min, with different diffusion constants (top: left to right is 0, 0.17, 0.83, 1.67, 3.33; bottom: left to right is 5.00, 6.67, 8.33, 10.00, 11.67, with a unit of 10^{-14} cm^2 s^{-1}). Bright spots represent sources with concentration maintained constant. Circles are the boundaries of active sections (x = 0.036), and totally merges in the last panel.

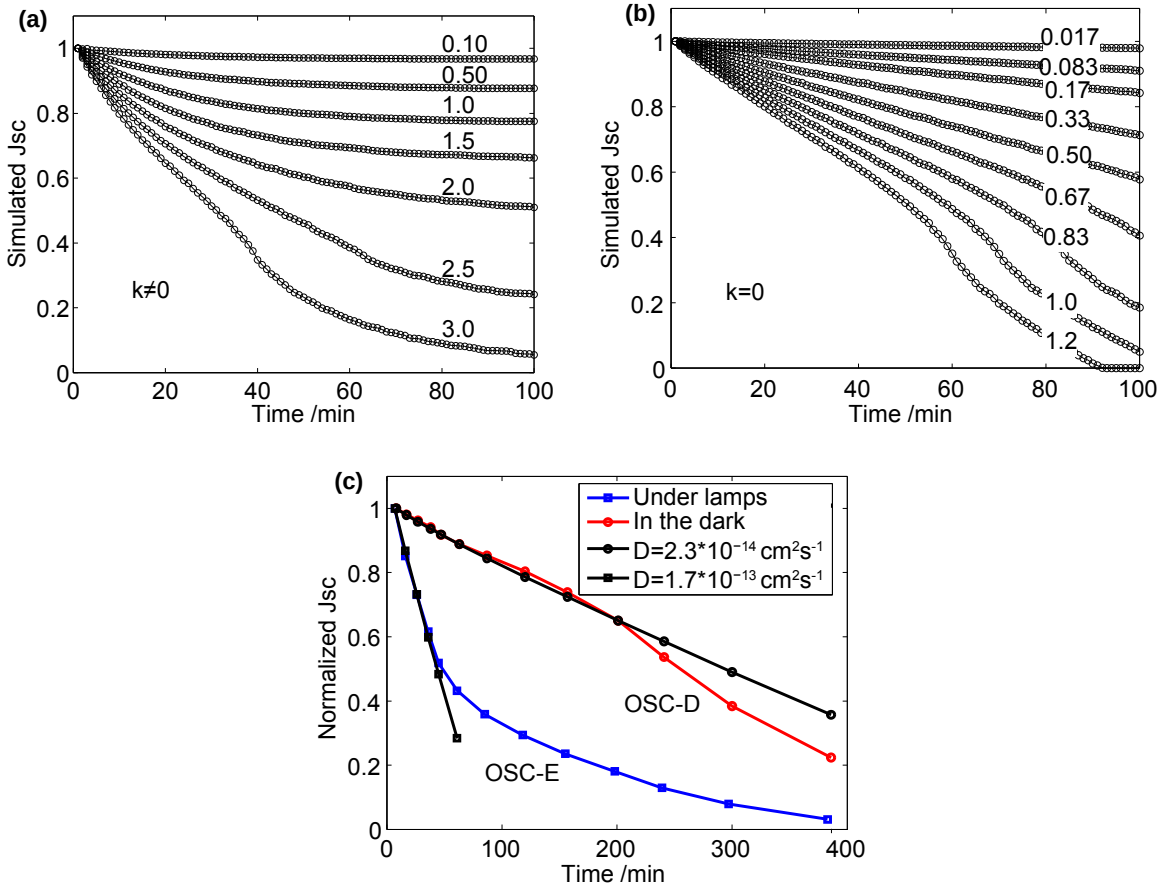

Figure 4–11 (a) Simulations of the multi-source diffusion with a first-order reaction with an arbitrarily set rate constant of 0.036 min^{-1}; (b) Simulations of the multi-source diffusion without a reaction or immobilization. Diffusion constants with a unit of 10^{-13} cm^2 s^{-1} are noted on the related curves; (c) Evolution of J_{SC} of an OSC-E and an OSC-D in one batch and simulated curves with a single-source non-reaction diffusion model (straight lines).

Let us consider the multi-source diffusion with (k > 0) or without (k = 0) a reaction. Firstly,

if oxygen diffused without reacting, a slight acceleration of degradation is expectable due to the inevitable overlapping between diffusing neighbor boundaries (*Figure 4*–10). It agrees with the trend of the degradation curve of the OSC-D shown in *Figure 4*–11(c). Secondly, if there is an irreversible reaction accompanying with the diffusion ($k > 0$), the degradation will eventually be slowed down [*Figure 4*–11(a)]. It interprets the curvature of the degradation curve of the OSC-E in *Figure 4*–11(c). Reaction of oxygen in OSCs has been suggested to be accelerated under light irradiation. [95, 128] Therefore, the diffusion of oxygen in OSCs is actually accelerated more than sevenfold under fluorescent lamps.

4.4.7. Application to others' work

A straightforward application of the lateral-diffusion model may be to supply an explicit explanation of extrinsic degradation curves of OSCs induced by the intrusion of oxygen. The degradation curves reported by Xi et al. in 2010 [135] were taken as an example to demonstrate the application, as shown in Figure 4–12.

Compared with our cells which were fabricated with thinner aluminum, cells reported by Xi et al. degrade relatively slowly. The initial slope of of the J_{SC}-t curve of the C_{70} cell is close to that of our C_{60} based OSC-D shown in *Figure 4*–11(c) (0.0018 min^{-1}). As discussed above, the initial slope of the degradation curve (J_{SC}-t) is approximately proportional to the diffusion constant. Consequently, it could be inferred that the diffusion constant of oxygen in C_{60} is 1.73 times that in C_{70}. However, one should keep in mind that these values may vary much, depending on the fabrication and test processes.

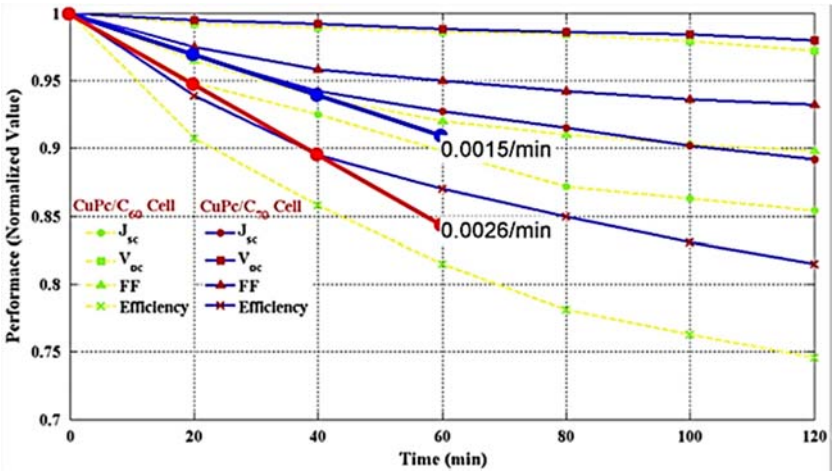

Figure 4–12 Application example of the 2-dimensionall diffusion model in OSCs with a structure of CuPc/C_{60}/LiF/Al reported in the reference [135]. Linear fittings were roughly executed on the normalized J_{SC}. The noted rates indicate the decreasing rate (slope) of the related normalized Jsc in the first twenty minutes (C_{60}), or forty minutes (C_{70}).

The cathode of OSCs is sometimes Ag in literature. An Ag-cathode device tends to give a longer shelf-life compared to an Al-cathode device. [145] From a chemical point of view, this can be easily understood according to the fact that silver is less reactive to oxygen

(and water) compared with aluminum. From a diffusion point of view, this can be understood as a consequence of the reduction of air sources in the cathode, resulting from the smaller grain size and grain boundaries in the silver film as shown in this literaure.

Because the oxygen affinity of fullerene is very high, the exposure of organic films (after the deposition of the fullerene layer) to air before the deposition of the cathode will deteriorate the shelf stability of the device. In order to apply the model to interpret this phenomenon, the pre-adsorbed oxygen needs to be taken into account. If the cathode (e.g. Al) reacts with oxygen, the pre-adsorbed oxygen molecules lower the scavenging capability of the cathode, and we should add an extra parameter c_s to terminate the reaction factor *kc* in Equation 4-12. If the cathode (e.g. Ag) does not react with oxygen, the pre-adsorbed oxygen will remain in the fullerene and trap charges, and then we should set the initial oxygen concentration C_0 to be nonzero. Nevertheless, as indicated in Equation 4-13, a nonzero C_0 does not influence the diffusion dynamics.

However, the diffusion model cannot cover all extensive degradation of OSCs involving various chemical and physical processes. One intriguing example is the recovery of an unencapsulated OSC in the dark after light exposure which was discussed in Chapter 3. In this case, photochemical reactions become complicated. And the photochemical models might give a complementary explanation to the degradation.

The diffusion model may also have difficulties in explaining the degradation of devices adsorbing water or having complicated donor-cathode interfaces. Besides, it could not be used to explain the intrinsic degradation in devices occurring in a long term.

4.5. Summary

In this chapter, we mainly created two models to explain the photo-induced degradation of small-molecular organic solar cells based on CuPc and C_{60} discussed in Chapter 3.

The first model is a photo-chemical model based on the fact that the short-term degradation in OSCs occurs mainly at the cathode interface. It involved several photo-induced processes occurring at the cathode interface. This photo-chemical model explains the light-induced chemical degradation in small-molecular OSCs. Parameterization of this model was also shown.

The second model is a lateral diffusion model based on Fick's laws of diffusion as well as the synergistic effect of oxygen and light irradiation on the degradation of fullerene-based OSCs mentioned in Chapter 3. The light-induced degradation of unencapsulated OSCs shown in Chapter 3 was attributed to the light-accelerated lateral diffusion of oxygen in the fullerene layer of an OSC. Besides the photo-accelerated diffusion of oxygen, we added a reaction (immobilization) term to reflect the light-induced oxidization in OSCs.

We found that only the microscopic pinholes in the aluminum cathode are insufficient to cause the rapid degradation of an unencapsulated device in a few hours. On the contrary, the density of grain-boundaries in the aluminum cathode is too large. Incorporating both pinholes and grain-boundaries which are wide enough for oxygen to pass through as the effective oxygen sources, we chose an average distance of oxygen sources of one micron for simulation.

We simulated the lateral diffusion of oxygen in the fullerene layer using different diffusion coefficients, considering that light irradiation could promote the diffusion of oxygen in fullerene. The simulations agree with experimental results discussed previously in Chapter 3, especially in curvatures of degradation curves. According to simulations, diffusion coefficient of oxygen in fullerene increases at least sevenfold under fluorescent lamps. At the end of this chapter, several extended applications of the lateral-diffusion model were mentioned.[Manual chapter break]

Chapter 5. Titanium-aluminum bilayer cathode

5.1. Introduction

5.1.1. Metal oxide/aluminum

Aluminum is commonly used as the cathodes of OSCs, mainly because of the suitable match of its work function (4.06—4.26 eV) with the electron affinity of fullerene (4.2 eV). However, the nature of aluminum makes OSCs age rapidly for several reasons. Firstly, aluminum itself is susceptible to oxidization, forming an insulating layer, particularly in the presence of water. [124] Secondly, the intrusion of oxygen through cracks at grain boundaries in aluminum films seriously impairs the fullerene in cells. [131, 146]

Many approaches have been found to be effective in protecting OSCs in air. Some of them use precious metals like gold, which increase the cost of manufacturing. One relatively cheap way is to use metal oxides as the ETLs beneath the aluminum cathodes. Sol-gel processed TiO_x or ZnO has been widely used in organic electronic devices like OFETs [147] and OSCs. The most attractive property of these materials is their oxygen (perhaps also water) scavenging capabilities. These materials processed with a sol-gel method are often baked at a mild temperature to remove the volatile solvents. This method is well compatible with the solution-processed polymeric OSCs and improves both the efficiency and stability of the fabricated devices in air. [148]

The improved efficiency of OSCs in the presence of TiO_x has been ascribed to the enhanced absorption of light in the PALs. [149] The enhancement of absorption was usually ascribed to the so-called optical spacing effect. Such a conclusion was proposed by comparing the calculated light intensity distribution in each layer with or without the transparent TiO_x layer. However, since the thickness of the TiO_x layer can be as thin as a few nanometers, such an ultrathin layer causes little optical redistribution. Therefore, the optical spacer explanation is questionable. The enhanced scatter of incident light by the metal oxides may also play a role in redistributing the incident light. In the presence of TiO_x, the incident light propagating in the PAL will encounter scatters from oxide clusters locating in the fullerene grain boundaries.

One issue related with the oxides of Zn or Ti used as ETLs in OSCs is associated with their fabrication processes. The fabrication method reported by Heeger's group is like this: spin-coating an isopropanol solution of $Ti[OCH(CH_3)_2]_4$, and then exposing the film in air for a while before baking it in an inert environment to remove the organic fragments. This method does not need a vacuum chamber, which makes it specifically suitable for thin-film coating on solution-processed polymeric blends (the PALs of polymeric BHJ-OSCs). However, a vacuum chamber is finally used even in this method to evaporate the

aluminum cathode onto the TiO_x surface. [149] What is more, the complex transfer processes used in this method consume a lot of energy and time. It is doubtless that finding a candidate way of improving the stability of OSCs is still urgently demanded, especially for the small-molecular OSCs, which are usually fabricated in vacuum.

Another common technique for depositing metal oxides is the atomic layer deposition (ALD). This method has been employed to deposit aluminum doped zinc oxide (AZO) films, which are used as the anode to replace ITO. [150] High stability in air can be achieved in an inverted structure with an anode deposited this way. However, metal gold is used as the cathode in this structure, making it impossible to horizontally compare the stability of the fabricated devices with the above-mentioned aluminum-cathode devices.

5.1.2. Metal on fullerene

Many bilayer cathodes have been applied to OSCs, either to improve the efficiency, or to improve the stability. In some cases, metals are directly deposited onto fullerene (planar or blending film) without any ETL. Therefore, it is important to have a review on how the deposited metal atoms locate themselves on the fullerene surface before further mechanism discussions of these metal cathodes.

Small atoms or ions can easily occupy the interstices in the face-centered cubic lattice of fullerene at room temperature. Metal atoms deposited on the surface of fullerene tends to occupy the octahedral interstices in the fullerene lattice, and further change the electric conductivity of the fullerene by supplying free electrons into the LUMO of fullerene. Haddon et al. suggest that small alkali metal cations like K^+ may intercalate into the octahedral vacant sites of fullerene without disrupting the network between fullerene molecules. [45] The intercalation increases the conductivity of the fullerene layer by adding no more than six electrons onto each fullerene molecule. A red shift of the Raman shift (5 cm^{-1} per electron on average) of fullerene at 1467 cm^{-1} (1458 cm^{-1} was also reported [125]) with the increase of electrons accepted on each fullerene molecule is observable. These observations suggest that the electron donors in fullerene red-shifts (vibration energy reduced) the Raman scattering of fullerene.

The situation of titanium on the surface of fullerene might be different from that of the alkali metals. Ohno et al. demonstrated that the first Ti layer deposited on fullerene forms a monolayer, but the subsequently deposited titanium will produce clusters. They also concluded that no intermixing of titanium atoms and fullerene could be evidenced. [151] On the contrary, Wang et al. argued that the C_{60} at Ti/C_{60} interface tends to diffuse into Ti layer and form amorphous Ti carbide. [152] Later, first principle calculation by Sun et al. confirmed the clustering tendency of titanium on the surface of fullerene. [153] These findings suggest that an ultrathin titanium layer deposited onto fullerene could perform similarly as bulk titanium metal. The titanium atoms presumably reside inbetween the grain-boundaries, rather than interdiffuse into the lattice.

5.1.3. Titanium/aluminum

Titanium stands for strength not only in name (from the Greek's gods, Titans), but also in fact. It has been widely utilized in areas where high strength and high corrosion resistance are simultaneously required, for example in the jet engine. Titanium has versatile functions in alloys. It acts as a deoxidizer in steel and as an alloying addition in many steels to reduce grain size, in stainless steel to reduce carbon content, in aluminum to refine grain size, and in copper to produce hardening. [3]

Besides these applications, titanium has also been used in vacuum to scavenge oxygen owing to its high affinity to oxygen. Moreover, its work function (3.95—4.45 eV) overlaps with that of aluminum. These properties would make titanium an ideal material satisfying the requirements for a stabilizer of the aluminum cathode of OSCs. To test this hypothesis, we deposited an ultrathin titanium layer prior to the deposition of aluminum during the fabrication of small-molecular OSCs (see *Figure 5*–2 for the stack structure).

Titanium surface exposed in air is immediately oxidized to a scale comprising TiO_2, which is an n-type anion-defective oxide through which oxygen ions can interstitially diffuse. [154] Consequently, a nanoscale titanium film is not a competent oxygen barrier to be used as the cathode of an OSC. Fortunately, by adding some specific doping atoms like Al or Nb, etc., the diffusion rate of oxygen in titanium can be significantly decreased by forming a dense metal oxide layer. [155]

Of the dopants of titanium that can improve the resistance to oxygen, aluminum has been studied the most. The oxidation resistance of an alloy film with a composition of Al_xTi_{1-x} increases with x, as shown in *Figure 5*–1. [155] For pure titanium, more than 50% of oxygen is incorporated into the metal, forming an oxygen-diffusion zone. [154] With increasing the aluminum ratio, the oxygen-diffusion zone becomes thinner and finally vanishes when a continuous alumina layer can be formed.

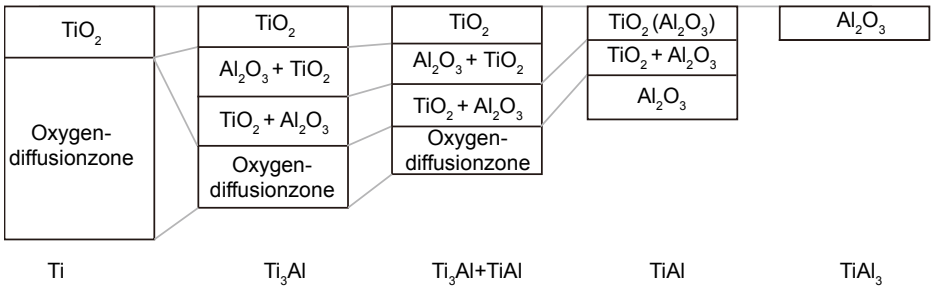

Figure 5–1 Schematic cross sections through the oxide layers and the oxygen diffusion zone in titanium and titanium-aluminides.

For the laminar Ti-Al structure we introduce here, a dense Al_2O_3 layer can undoubtedly form in air, which can be evidenced by the TOF-SIMS results shown in the last sections of

[3] http://www.britannica.com/EBchecked/topic/597135/titanium-Ti

this chapter.

In this chapter, we mainly discuss the stability of small-molecular organic solar cells with different buffer layers, as well as different cathodes. Although the optimization of fabrication parameters has only been done in a preliminary level, we could have proven that a horizontal comparison between the stability of devices with relatively low initial PCE can reflect the relative stability of optimized ones.

We employ three different types of cathodes to fabricate devices in this chapter, i.e. aluminum, titanium, and aluminum-titanium cathodes. Hereinafter, devices with these three cathodes are denoted as Al-OSCs, Ti-OSCs, and AlTi-OSCs, respectively. For the HTL, MoO_3 or PEDOT:PSS is used. For the ETL, LiF, TiO_x or BCP is used. The stability and initial performance of fabricated devices depend dramatically on the choice of each layer. The AlTi-OSCs showing extremely long shelf lives are the major topic of this chapter. After showing the performances of these devices, we further discuss the stabilization mechanisms in the AlTi-OSCs by probing the elemental depth profiles in several fabricated devices.

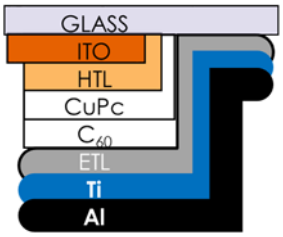

Figure 5–2 Schematic diagram of the stack structure of the AlTi-OSCs discussed in this chapter.

5.2. Al-OSCs

5.2.1. PEODT:PSS-PAL-LiF-Al

Devices with a structure of ITO (150 nm)/PEDOT:PSS (60 nm)/CuPc (25 nm)/C_{60} (40 nm)/LiF (2 nm)/Al (75 nm) with an active area of 1.05 cm^2 were fabricated as described in Chapter 2. Performance of one cell is shown in *Figure 5*–3. Intermittent *I-V* curves were recorded with the Keithley2400 SourceMeter using the aperture method under the halogen lamp (80 mW cm^{-2}, spectra in Figure 2–21 in Chapter 2).

THM (definition in Section 2.2.8) of this device was only 1.2 h under fluorescent lamps. During the degradation, J_{SC} and *FF* dropped rapidly, indicating a rapid intrusion of air into this device. One common drawback of OSCs is that devices with higher initial performances generally degrade more rapidly. This can be explained by the fact that metal oxides on a metal surface usually passivate the metal from further oxidization. At

the inner interface of the cathode of an OSC, when an oxidized layer has been formed, it slows down the inhalation of oxygen of the cell. However this oxide layer blocks electrons passing through the interface if it is an insulating layer.

We compared the integrals of P_{max} over time (P_{TOTAL}) defined in Equation 5-1 of different devices. P_{TOTAL} reflects the photovoltaic capability of an OSC. Notes that this integral also depends on the intensity of used light source.

$$\mathrm{P_{TOTAL}} = \int_{t_0}^{t_{\mathrm{end}}} \mathrm{P_{max}(t)}\ \mathrm{d}t \qquad 5\text{-}1$$

where t_0 is the time of the first recorded *J-V* curve, and t_{end} the time of the finally recorded *J-V* curve. P_{TOTAL} of the device shown in *Figure 5*–3 is 3.6 J cm^{-2}.

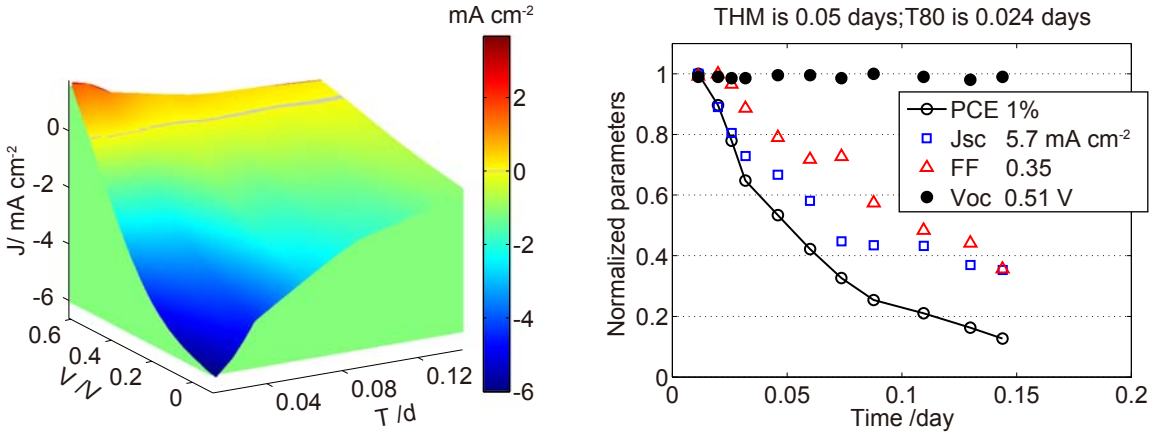

Figure 5–3 (left) J-V-time valley of an Al-OSC with a structure of PEODT:PSS-PAL-LiF-Al. (Right) Normalized parameters of the LiF-Al-OSC.

5.2.2. PEODT:PSS-PAL-BCP-Al

Devices with a structure of ITO (150 nm)/PEDOT:PSS (50 nm)/CuPc (20 nm)/C_{60} (40 nm)/BCP (8 nm)/Al (100 nm) with an active area of 0.06 cm^2 were fabricated as described in Chapter 2. Intermittent *I-V* curves were recorded with the Keithley2400 SourceMeter, under the solar simulator (AM1.5G, 100 mW cm^{-2}). Results are shown in *Figure 5*–4 and *Figure 5*–5.

We compared P_{TOTAL}s of two Al-OSCs with different initial performances, e.g. an initially high-performance device (OSC-high-1) and an initially low-performance device (OSC-low-1). P_{TOTAL} of the OSC-high-1 (*Figure 5*–4) was about 6.5 J cm^{-2}, while P_{TOTAL} of the OSC-low-1 (*Figure 5*–5) was about 57.0 J cm^{-2}. We speculate that the OSC-low-1 had an aluminum oxide layer which blocked charge transport, meanwhile suppressing the oxygen inhalation of the device.

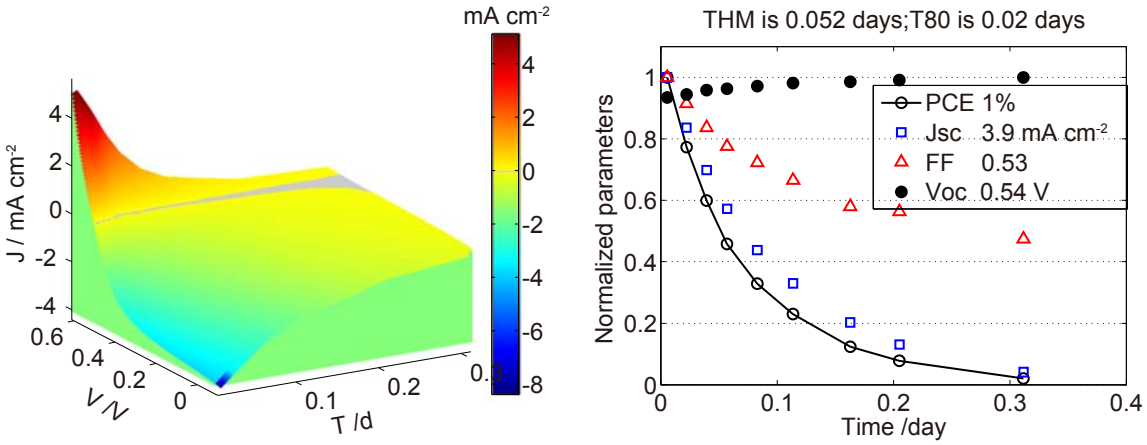

Figure 5–4 (left) J-V-time valley of the OSC-high-1 (see the text) with a structure of PEDOT:PSS-PAL-BCP-Al. (Right) Normalized parameters of the BCP-Al-OSC.

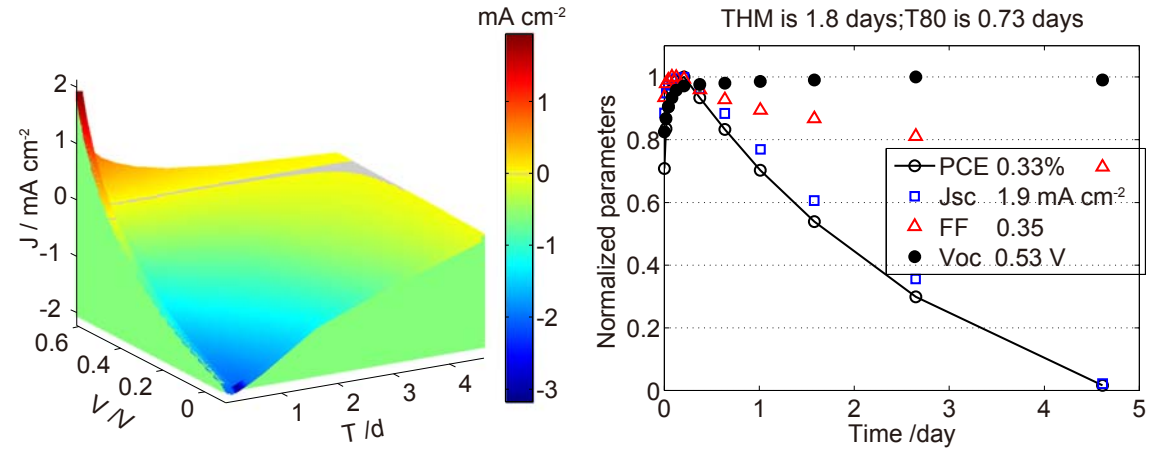

Figure 5–5 (left) *J-V-time* valley of the OSC-low-1 with a structure of PEDOT:PSS-PAL-BCP-Al. (Right) Normalized parameters of the BCP-Al-OSC.

5.2.3. MoO_3-PAL-BCP-Al

Devices with a structure of ITO (150 nm)/MoO_3 (5 nm)/CuPc (20 nm)/C_{60} (40 nm)/BCP (8 nm)/Al (100 nm) with an active area of 0.05 cm^2 were fabricated as described in chapter 2. Intermittent *I-V* curves were recorded as above (AM1.5G, 100 mW cm^{-2}). Performances of two cells are shown in *Figure 5*–6 and *Figure 5*–7.

Similarly as above, we compared P_{TOTAL}s of two such devices with different initial performances, including an initially high-performance device (OSC-high-2) and an initially low-performance device (OSC-low-2). P_{TOTAL} of OSC-high-2 (*Figure 5*–6) was about 138.2 J cm^{-2}, while that of OSC-low-2 (*Figure 5*–7) was about 112.3 J cm^{-2}.

On average, THMs of MoO_3-Al-OSCs were much longer than those of PEDOT:PSS-Al-OSCs discussed above. One possible explanation is that the PEDOT:PSS layer absorbed water

which further oxidized the aluminum cathode. [124]

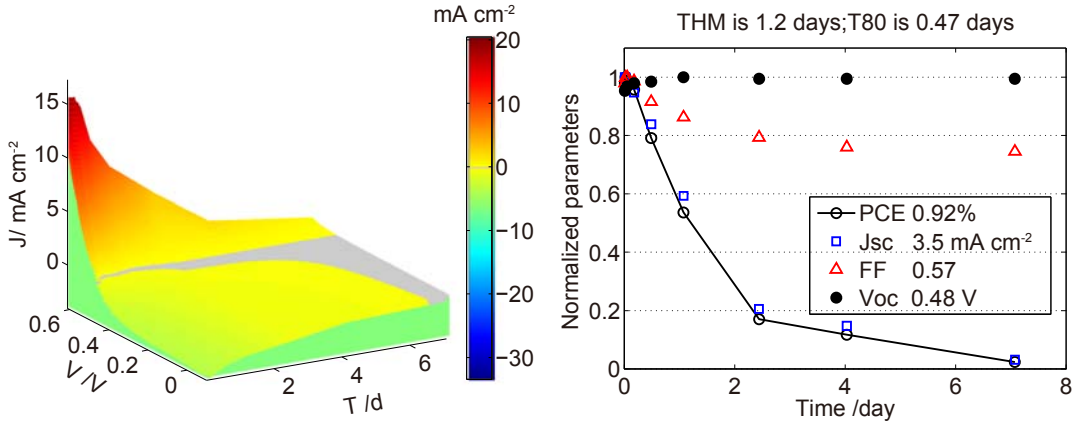

Figure 5–6 (left) *J-V-time* valley of the OSC-high-2 with a structure of MoO_3-PAL-BCP-Al. (Right) Normalized parameters of the Al-OSC.

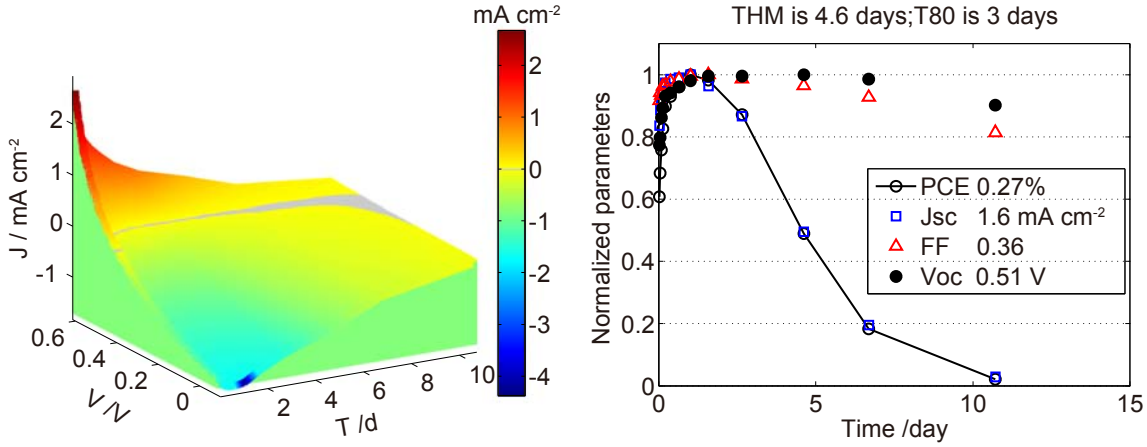

Figure 5–7 (left) *J-V-time* valley of the OSC-low-2 with a structure of MoO_3-PAL-BCP-Al. (Right) Normalized parameters of the Al-OSC.

5.2.4. PEDOT:PSS-PAL-TiO_x-Al

Devices with a structure of ITO (150 nm)/PEDOT:PSS (60 nm)/CuPc (25 nm)/C_{60} (40 nm)/TiO_x (2 nm)/Al (75 nm) with an active area of 0.06 cm^2 were fabricated as described in Chapter 2 and Chapter 3. These devices were pre-annealed in Ar for 5 min after the deposition of an ultrathin layer of Ti and before the deposition of aluminum in the bell-shape chamber. During the exposure in air for about 20 s, the titanium layers were oxidized to titanium oxides. The titanium oxide layers were considered as nonstoichiometric because TiO_2 can be reduced by the subsequently deposited aluminum. [156]

J-V curves of one cell were intermittently recorded under a Xe lamp (95 mW cm^{-2}, spectra shown in Figure 2–21 in Chapter 2) in air. The results are shown in *Figure 5*–8.

P_{TOTAL} of this device was about 3.7 J cm^{-2}, three orders of magnitude less than that of an AlTi-OSC discussed in the following section. This immense divergence suggests that the ultrathin TiO_x film had little effect on the stability of the fabricated devices.

These devices suffered much from the inhalation of oxygen, as indicated by the S-shaped *J-V* curves (the left-front cross-section of the *J-V-time* valley on the left of Figure 5–8). We inferred that these devices had failed to form a continuous titanium oxide layer beneath the aluminum cathode. The ultrathin oxidized titanium film was presumably either ruptured by the pre-annealing, or diffused into the grain-boundaries of the fullerene layer. And as a result, the overall device comprised only Al-OSC sections (as introduced in Chapter 4).

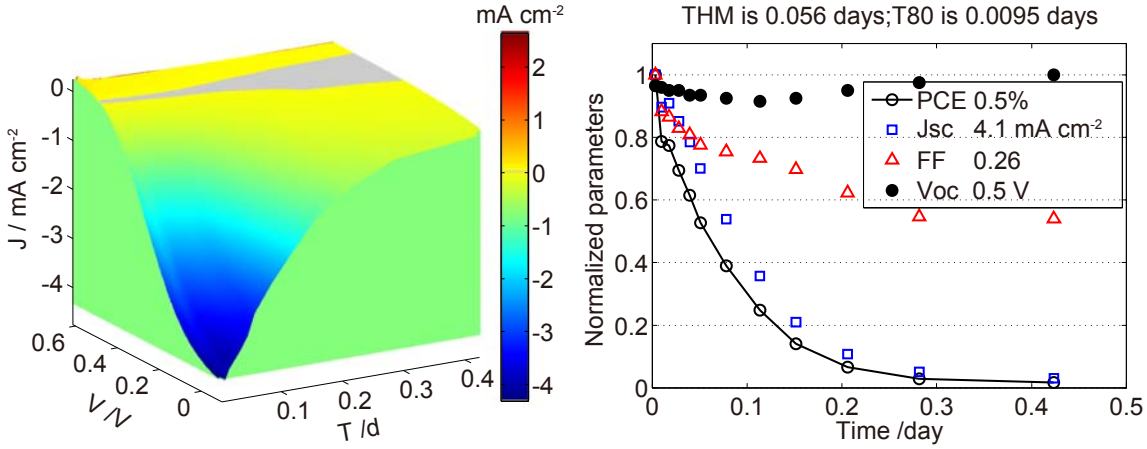

Figure 5–8 (left) J-V-time valley of an Al-OSC with a structure of PEDOT:PSS-PAL-TiO_x-Al. (Right) Normalized parameters of the Al-OSC.

5.3. Ti-OSCs

Devices with cathodes made up of only titanium are discussed in this section. Ti-OSCs with a structure of ITO (150 nm)/PEDOT:PSS (60 nm)/CuPc (20 nm)/C_{60} (40 nm)/LiF (2 nm)/Ti (100 nm) with an active area of 0.06 cm^2 were fabricated. The titanium cathodes were deposited with the 6 kV EB gun at a deposition rate of 0.003—0.1 nm s^{-1} in the EL chamber. We gradually increased the deposition rate to reduce the deposition time. However, the increased deposition rate (e.g. 0.1 nm s^{-1}) seemed to increase the risk of forming shortage spikes between electrodes, as discussed in the next sections. Other layers were fabricated with the same procedures as those for the Al-OSCs discussed in Chapter 2. *I-V* curves were intermittently recorded with the Keithley2400 SourceMeter under the solar simulator (AM1.5G, 100 mW cm^{-2}). Between *I-V* tests, the Ti-OSCs were stored under several fluorescent lamps at room temperature.

Figure 5–9 shows the performance of a Ti-OSC. P_{TOTAL} of this device was 741 J cm^{-2} within the initial 6.5 months shown in *Figure 5*–9. One interesting feature of Ti-OSCs was that they degraded in a fluctuating way (see the ridges on the *J-V-time* valley shown on the

left of *Figure 5*–9). Degradation slowed down and oscillated after the device lost about 85% of the initial performance. We attributed these featured stabilized low-performance states to the formation of TiO_2. Some dye-sensitized photochemical sections (as introduced in Chapter 4) were presumably formed along with the oxidization of titanium.

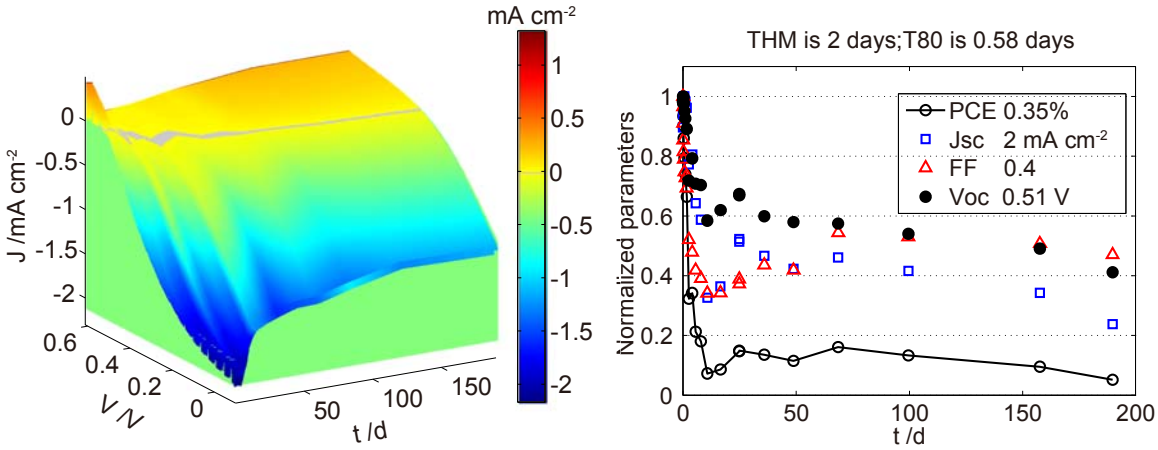

Figure 5–9 (left) J-V-time valley of a Ti-OSC with a structure of PEDOT:PSS-PAL-LiF-Ti. (Right) Normalized parameters of the Ti-OSC.

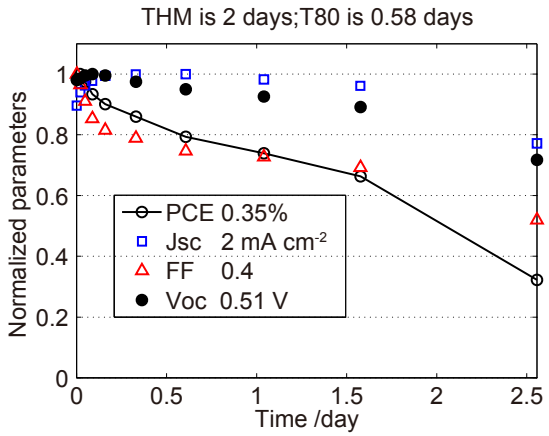

Figure 5–10 Normalized performance of the device shown in Figure 5–9 in the initial two and a half days.

We averaged performances over eight Ti-OSCs and the results are shown in Figure 5–11. These devices showed similar behaviors.

In the next sections, we fabricated devices with consecutively deposited titanium layers and aluminum layers in the high-vacuum EL chamber, without breaking the vacuum. The stability of these devices was much improved compared to the above discussed Al-OSCs and Ti-OSCs.

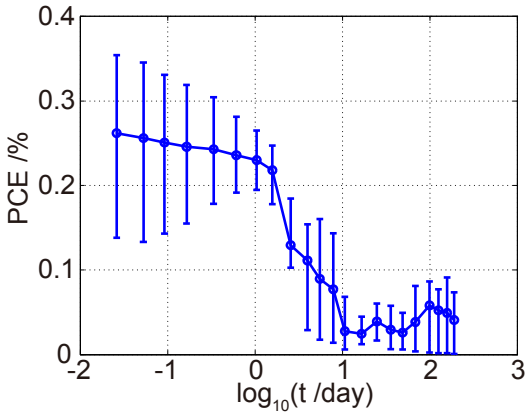

Figure 5–11 Averaged performance of eight Ti-OSCs with the same structure as the one shown in Figure 5–9.

5.4. PEODT:PSS-PAL-LiF-Ti-Al

Ti-Al cathodes have been reported to be used in OSCs in which they were used as the inner electrodes adjacent to glass substrates. [157] In such a structure, the titanium layer provides no protection once exposed to air. In contrast, the structure we used here is capable of protecting unencapsulated OSCs exposed to air.

AlTi-OSCs with a structure of ITO (150 nm)/PEDOT:PSS (60 nm)/CuPc (20 nm)/C_{60} (40 nm)/LiF (1.5 nm)/Ti (2 nm)/Al (100 nm) with an active area of 0.06 cm^2 were fabricated in the EL chamber. Other layers were fabricated with the same procedures as the Al-OSCs discussed in Chapter 2. The titanium and aluminum layers were deposited with the 6 kV EB gun at deposition rates of 0.003 nm s^{-1} and 0.1 nm s^{-1}, respectively. *I-V* curves were intermittently recorded with the Keithley2400 SourceMeter under the solar simulator (AM1.5G, 100 mW cm^{-2}). Between the *I-V* tests, cells were stored under several fluorescent lamps at room temperature. Several devices were encapsulated with glass sealed with UV resins at edges in an argon glove box.

Performance of one unencapsulated device with the bilayer cathode is shown in *Figure 5*–12. An estimated shelf life of at least 1 year can be achieved (averaged over 4 devices, Figure 5–14). However, *FF* of these devices was relatively low, perhaps due to the thickness and deposition rate of the aluminum, or due to the existence of the LiF buffer layers.

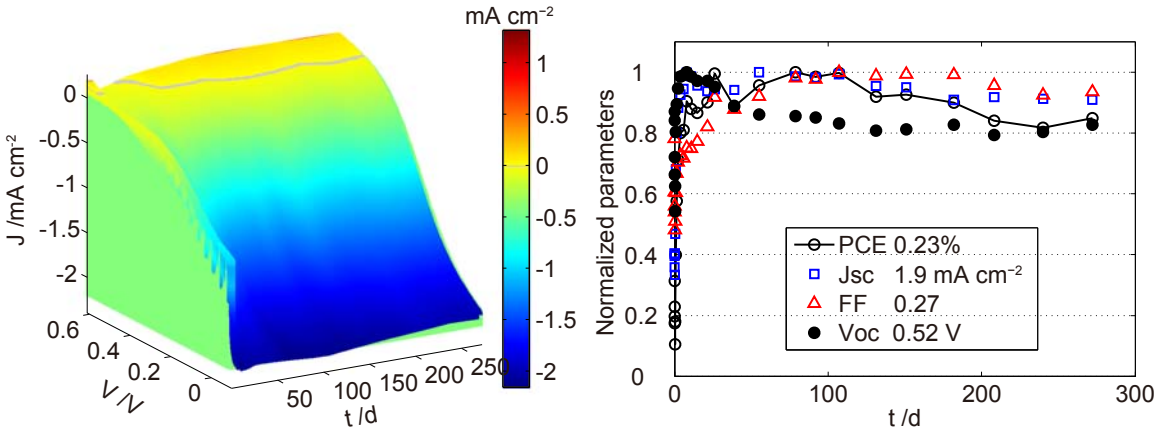

Figure 5–12 (left) J-V-time valley of an AlTi-OSC with a structure of PEDOT:PSS-PAL-LiF-Ti-Al. (Right) Normalized parameters of the AlTi-OSC.

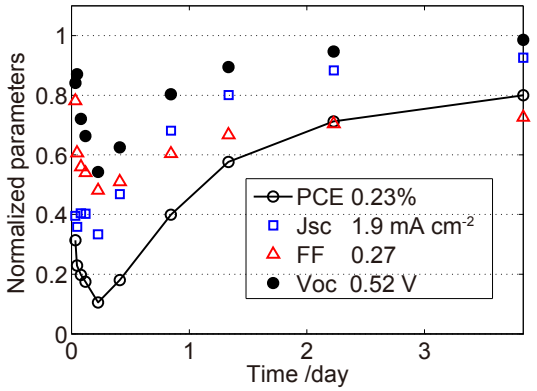

Figure 5–13 Normalized performance of the device shown in Figure 5–12 in the initial period.

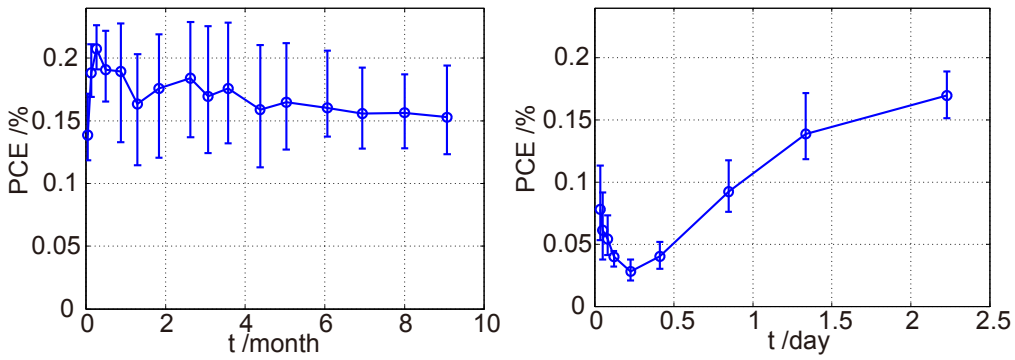

Figure 5–14 Averaged performance of four AlTi-OSCs with a structure of PEDOT:PSS-PAL-LiF-Ti-Al. (Left) long-term performance; (right) initial performance.

P_{TOTAL} of this device was 4.9 kJ cm^{-2} within the initial 9 months shown in *Figure 5*–12. Performance of this device in the initial few days is shown in *Figure 5*–13. Upon exposure in air, both V_{OC} and *FF* decreased in the initial several hours, and then restored and

surpassed their initial values. This phenomenon was observed merely for AlTi-OSCs, indicating that it was related with the titanium layer. Another interesting phenomenon is that the J at V > V_{OC} at t > 50 d rebounded, resulting from a decreased R_s.

One possible explanation of the increase of performance of the AlTi-OSCs in air is that the metal titanium was oxidized by oxygen. The oxygen sources might be either the organic or the aluminum layer (from the ambient air). The titanium oxide is semiconductor which selectively transports electrons.

We also stored one group of PEDOT:PSS-LiF-AlTi-OSCs in the dark (AlTi-OSC-D, as discussed in Chapter 3). We recorded its *J-V* curves intermittently under a Xe lamp (100 mW cm^{-2}, spectra in Figure 2–21 in Chapter 2) in the initial few months with results shown on the left of Figure 5–15, and then under a solar simulator (AM 1.5G, 100 mW cm^{-2}) with results shown on the right of Figure 5–15. This device was initially short-circuited (R_{sh} very small). It slowly inhaled air from the ambience. After about one hour, V_{OC} (black squares) quickly increased, probably resulting from the oxidization of shortage spikes (shortage Ti→TiO_x). After about one month, J_{SC} (blue squares) surged, perhaps resulting from the formation of semiconducting titanium oxides.

We have shown in Chapter 3 that low light irradiation accelerated the degradation of Al-OSCs. To check the effect of low light irradiation on AlTi-OSCs, we stored the above-mentioned AlTi-OSC-D under fluorescent lamps for two periods between successive *J-V* tests (yellow patches on the right of Figure 5–15). This AlTi-OSC-D had been gradually degrading at a rate of about 4% per month in the dark before the two periods of tests. After the low-light exposure, J_{SC}, V_{OC} and PCE increased, while *FF* decreased in the first period and increased in the second period. One possible explanation is that oxygen residing in fullerene was removed from the fullerene layer under the low light irradiation, oxidizing Ti (Al) to TiO_x (Al_2O_3).

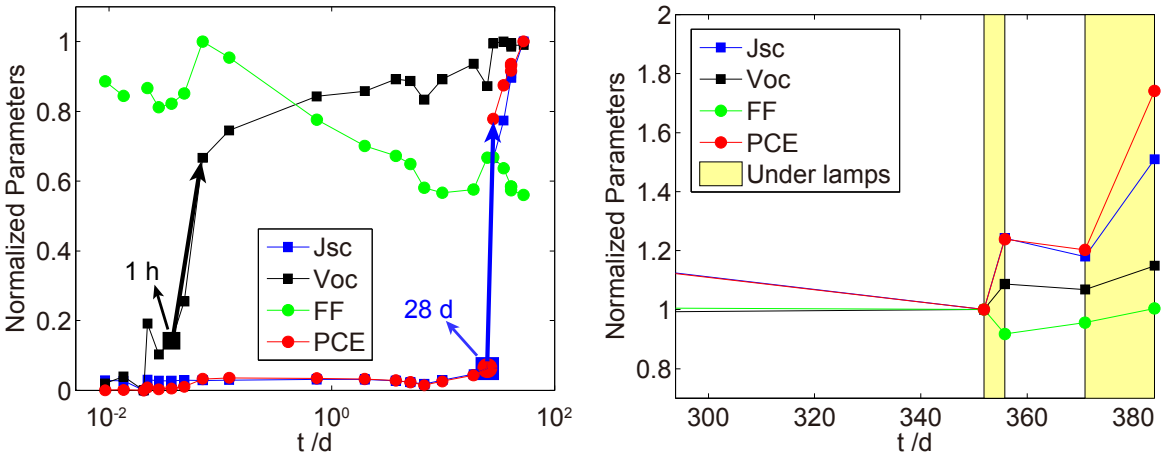

Figure 5–15 Normalized evolutions of parameters of an AlTi-OSC-D. (Left) in the initial few months. Arrows mark the surges of V_{OC} and J_{SC} (also PCE). (Right) after 10 months in air. Two periods of exposure under fluorescent lamps are marked with the yellow patch. Two figures have consecutive time axes, but different normalization values.

These observations are consistent with the phenomenon that a ZnO device needs some photo-annealing to obtain a maximum efficiency. [73] We note here that other devices discussed in this chapter were stored under fluorescent lamps in the idle periods.

We further checked the stability of two other LiF-AlTi-OSCs under continuous simulated solar irradiation (weathering test). The results are discussed in section 5.8.1.

5.5. PEODT:PSS-PAL-Ti-Al

AlTi-OSCs with a structure of ITO (150 nm)/PEDOT:PSS (60 nm)/CuPc (20 nm)/C_{60} (40 nm)/Ti (2 nm)/Al (100 nm) with an active area of 0.06 cm^2 were fabricated and tested similarly as above. These devices without any ETL were prone to forming shortage spikes between electrodes during the deposition, resulting in very low $R_{sh}A$. We fabricated several devices having relatively high $R_{sh}A$ such that they could show photovoltaic character. Performance of one of these cells is shown in *Figure 5*–16 and *Figure 5*–17. P_{TOTAL} of this device was 1.6 kJ cm^{-2} within the initial 4.5 months shown in *Figure 5*–16.

Compared to the device with an ETL of LiF (*Figure 5*–12), the non-ETL device shown in *Figure 5*–16 degraded a little faster, which was perhaps due to the clustering of titanium on the surface of fullerene in the absence of any ETL. As a consequence of clustering, some sections became Al-OSC. The majority of the entire device was composed of AlTi-OSC sections, while a small part was constituted by Al-OSC sections.

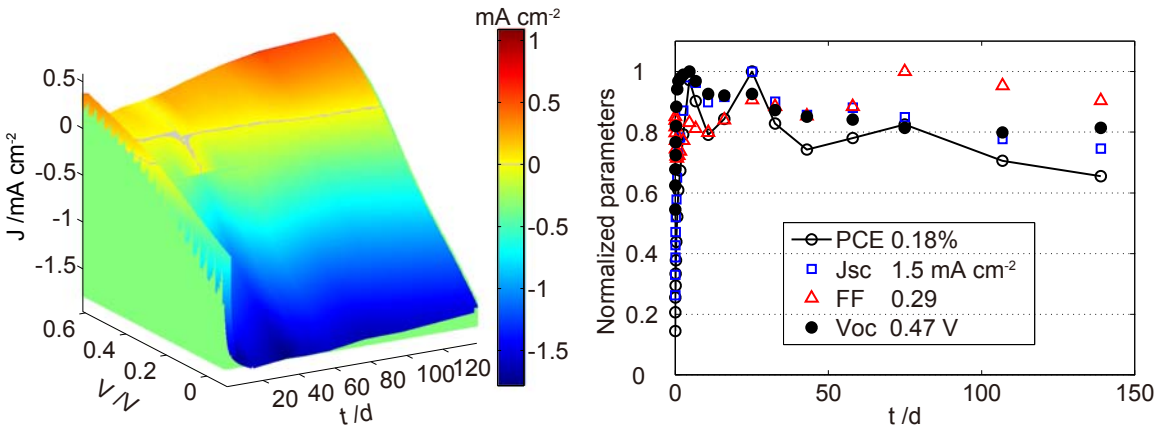

Figure 5–16 (left) *J-V-time* valley of an AlTi-OSC with a structure of PEDOT:PSS-PAL-Ti-Al. (Right) Normalized parameters of the AlTi-OSC. The initial performance is shown in Figure 5–17.

The performance of this device in the initial one week is shown in *Figure 5*–17. Upon exposure in air in this initial period, J_{SC} and V_{OC} increased, while *FF* decreased at first and then increased. One explanation is that the oxidization of titanium annihilated the shunted spikes between electrodes, thereby increasing V_{OC}. Nevertheless, the inhaled oxygen trapped charges, lowering *FF*, and then oxidized Ti into TiO_x which facilitated the

transport of electrons, thereby increasing J_{SC}. Removal of the inhaled oxygen by Ti finally restored *FF*.

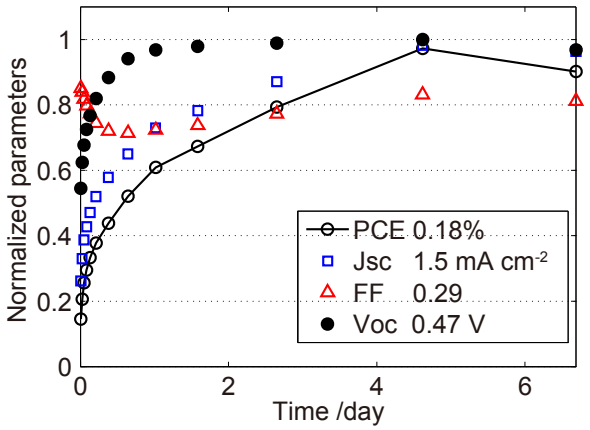

Figure 5–17 Normalized performance of the device shown in Figure 5–16 in the initial one week.

5.6. PEODT:PSS-PAL-BCP-Ti-Al

5.6.1. High- and low-performance devices

We compared P_{TOTAL}s of two BCP-AlTi-OSCs with different initial performances, i.e. an initially-low-performance device (PEDOT:PSS-BCP-AlTi-low) shown in *Figure 5*–18 and an initially-high-performance device (PEDOT:PSS-BCP-AlTi-high) shown in *Figure 5*–20. The deposition rates of the aluminum cathodes were 0.1 nm s^{-1} and 0.5 nm s^{-1}, respectively. For both devices, a structure of ITO (150 nm)/PEDOT:PSS (60 nm)/CuPc (20 nm)/C_{60} (40 nm)/BCP (8 nm)/Ti (2 nm)/Al (100 nm) with an active area of 0.06 cm^2 were fabricated and tested similarly as above.

The performance of the PEDOT:PSS-BCP-AlTi-low is shown in *Figure 5*–18 and *Figure 5*–19. This device showed increasing performance in air over the initial four months. Compared to the LiF-AlTi-OSC with performance shown in *Figure 5*–12, this BCP-AlTi-OSC had a relatively high *FF*, indicating a reduced amount of charges (oxygen-trapped probably) at the cathode inner interface. We may conclude that the BCP layer effectively protected the fullerene layer from directly contacting with the intruding air. P_{TOTAL} of this device was 5.7 kJ cm^{-2} within the initial 4.5 months. From a time-average point of view, this value is almost twice that of the LiF-AlTi-OSC shown in *Figure 5*–12, and more than thrice that of the non-ETL-AlTi-OSC shown in *Figure 5*–16.

On the other hand, P_{TOTAL} of the PEDOT:PSS-BCP-AlTi-high shown in Figure 5–20 was about 4.0 kJ cm^{-2} within the initial two months. However, this device degraded much faster than the PEDOT:PSS-BCP-AlTi-low shown in *Figure 5*–18. In the next section, we show several other PEDOT:PSS-BCP-AlTi-OSCs showing similar initial performance with

the one shown in *Figure 5*–20, but exhibiting higher shelf stability.

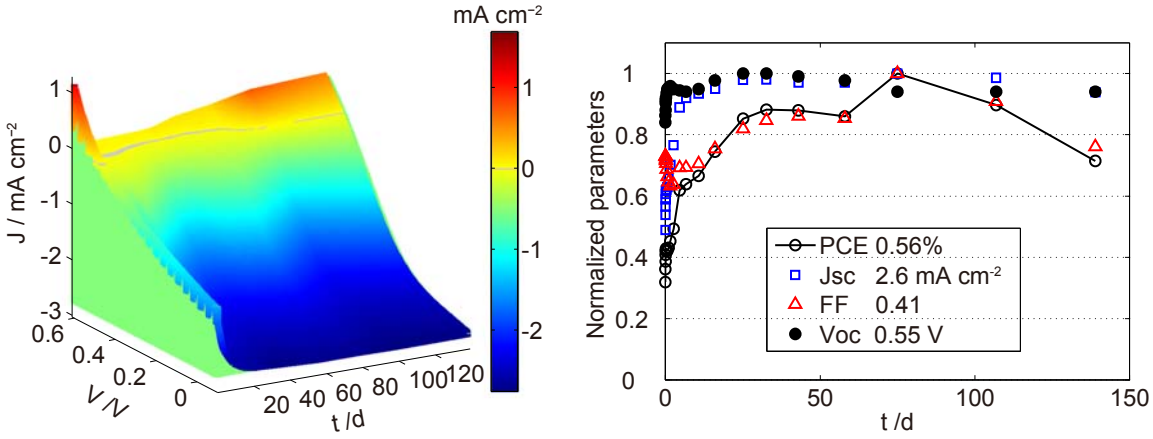

Figure 5–18 (left) *J-V-time* valley of the PEDOT:PSS-BCP-AlTi-low with a structure of PEDOT:PSS-PAL-BCP-Ti-Al. (Right) Normalized parameters of the AlTi-OSC.

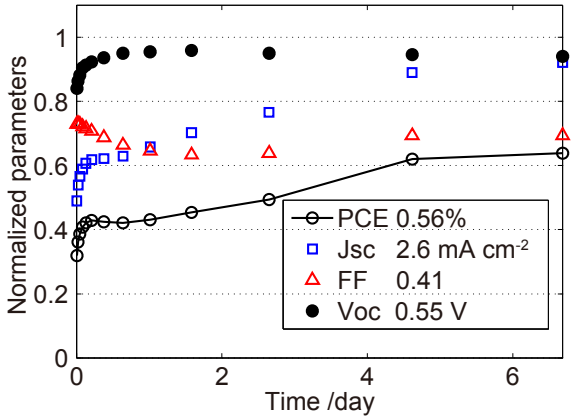

Figure 5–19 Normalized performance of the device shown in Figure 5–18 in the initial one week.

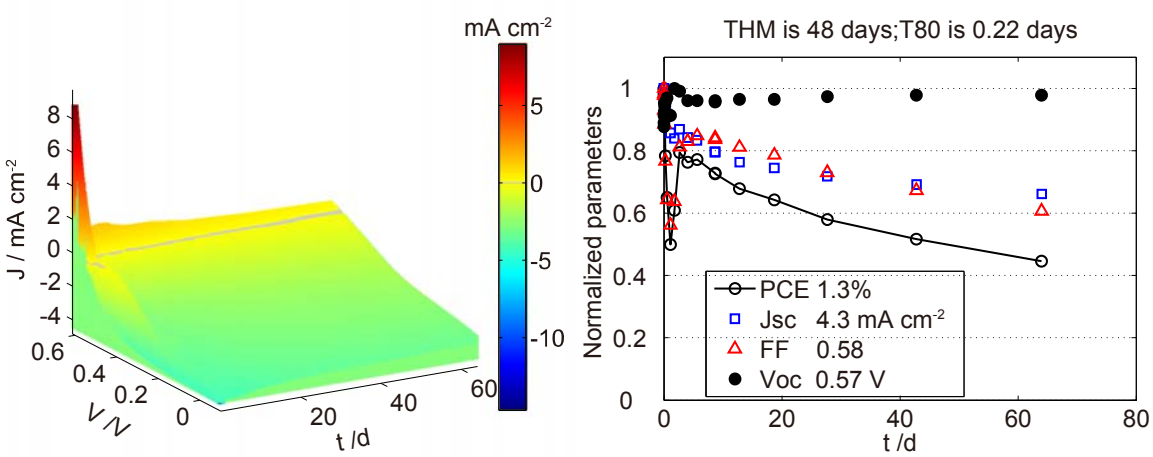

Figure 5–20 (left) *J-V-time* valley of the PEDOT:PSS-BCP-AlTi-high with a structure of PEDOT:PSS-PAL-BCP-Ti-Al. (Right) Normalized parameters of the AlTi-OSC.

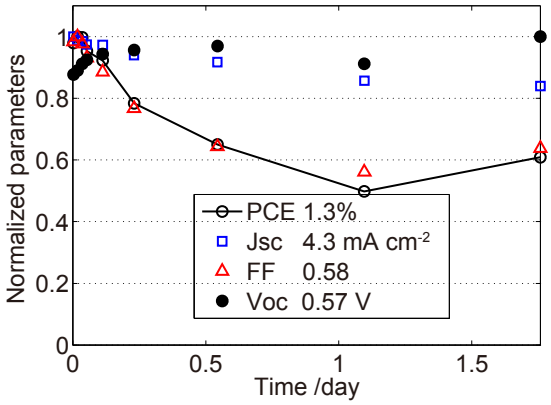

Figure 5–21 Normalized performance of the device shown in Figure 5–20 in the initial two days.

5.6.2. Deposition rate of cathode

Table 5 summarizes parameters of three devices with cathodes deposited at different rates. These devices had a structure of ITO (150 nm)/PEDOT:PSS (50 nm)/CuPc (20 nm)/C_{60} (40 nm)/BCP (8 nm)/Ti (2 nm)/Al (100 nm), stored and tested under the same condition: AM1.5G 100 mW cm^{-2}, 20 °C. The parameters were extracted at the maximum PCE moment of each device using the *Delta approximation method* discussed in Chapter 1.

For devices with the same Ti layers (thickness and deposition rate), key parameters (J_{SC}, V_{OC}, *FF*, and PCE) of the device with a fast-deposited aluminum cathode (cell 2) were larger than those of the slowly deposited aluminum cathode device (cell 1). Some parameters of cell 1 were not extractable and noted with a dash mark (-), and similarly hereinafter. We estimated some THMs with the assumption that unencapsulated devices degraded linearly in air. We marked tildes (~) before these estimated values. THM of cell 2 was only 48 days, whereas THM of cell 1 was longer than half a year. We speculate that the slowly deposited Al cathode was pre-oxidized into Al_2O_3, which possesses a very high air-resistance [154], resulting in enhanced shelf stability in air.

For devices with the same Al layer (cell 2 and cell 3), key parameters of devices with different Ti layers were similar. However, the series resistance R_sA of the slowly deposited cathode device (cell 2) was several times larger than that of the fast-deposited-cathode device (cell 3), while the saturated current density J_0 of cell 3 was larger than that of cell 2. These comparisons suggest that the slowly deposited cathode presumably formed a charge-blocking layer. Besides, the fast-deposited-cathode device had a THM of approximately eight months, much longer than that of the slowly deposited cathode device. One possible explanation of this divergence is that the fast deposited titanium does not have enough time to cluster. A relatively uniform titanium layer could be

formed beneath the aluminum layer. Consequently, the entire device comprises completely AlTi-OSC sections.

Table 5 Parameters of devices fabricated with cathodes deposited at different rates Γ, at maximum PCE moments.

No.	**Γ_{Ti}** **nm s^{-1}**	**Γ_{Al}** **Nm s^{-1}**	**J_{SC}** **mA cm^{-2}**	**V_{OC}** **V**	***FF***	**PCE** **%**	**n**	**R_sA** **Ω cm^2**	**$R_{sh}A$** **Ω cm^2**	**J_0** **μA cm^{-2}**	**J_{ph}** **mA cm^{-2}**	**THM** **d**
1	0.003	0.1	2.6	0.52	0.41	0.56	-	-	-	-	-	~200
2	0.003	0.5	4.3	0.5	0.58	1.3	2.4	5.1	1071	0.94	4.3	48
3	0.1	0.5	4.2	0.49	0.56	1.1	2.6	1.9	760	1.92	4.2	~200

5.6.3. Thickness of titanium

Table 6 summarizes the extracted parameters from AlTi-OSCs (including one Al-OSC and one Ti-OSC) with titanium layers of different thicknesses. These devices had a structure of ITO (150 nm)/PEDOT:PSS (50 nm)/CuPc (20 nm)/C_{60} (40 nm)/BCP (8 nm)/Ti (x nm)/Al (100 or 0 nm). The deposition rate of aluminum was identical, 0.5 nm s^{-1}. Thickness of aluminum was zero for the Ti-OSC (cell 6). These devices were stored and tested under the same condition: AM1.5G 100 mW cm^{-2}, 20 °C in air. The parameters were extracted at the maximum PCE moment, also the initially tested moment of each device.

Table 6 Parameters of devices fabricated with titanium cathodes of different thicknesses, at the related maximum PCE moments.

No.	***x***	**J_{SC}** **mA cm^{-2}**	**V_{OC}** **V**	***FF***	**PCE** **%**	**n**	**R_sA** **Ω cm^2**	**$R_{sh}A$** **Ω cm^2**	**J_0** **μA cm^{-2}**	**J_{ph}** **mA cm^{-2}**	**THM** **d**
1	0	3.8	0.50	0.53	1.03	2.6	6.3	734	1.47	3.9	0.076
2	2	4.2	0.49	0.56	1.12	2.6	1.9	760	1.92	4.2	~200
3	4	4.4	0.49	0.57	1.23	2.5	2.2	888	1.94	4.4	~260
4	8	3.7	0.48	0.58	1.02	2.6	1.2	1164	2.22	3.7	41
5	10	-									
6	100	Refer to section 5.3									

The devices with titanium layers thicker than 10 nm (cell 5 and cell 6) were short-circuited. This suggests that at room temperature, titanium tends to form shortage spikes deep down to the ITO layer from the top of the fullerene layer. However, this risk meanwhile brings about a decrease of the series resistance R_sA. Optimizing the thickness and deposition rate of the titanium layer can keep the merit and eliminate the demerit. On the contrary, aluminum is less prone to forming such shortage spikes upon organic layers, nevertheless it often causes a relatively high series resistance which is detrimental to charge transport.

One interesting phenomenon here is that V_{OC} of these devices seemed to be not influenced by the existence of a titanium layer, indicating that no Schottky junction was formed between the ETL and the titanium layer.

Performances of cell 2, cell 3, and cell 4 are shown in *Figure 5*–22 and *Figure 5*–23, *Figure 5*–24 and *Figure 5*–25, and *Figure 5*–26 and *Figure 5*–27, respectively. The device with a 4 nm thick titanium layer performed the best, both efficiently and durably.

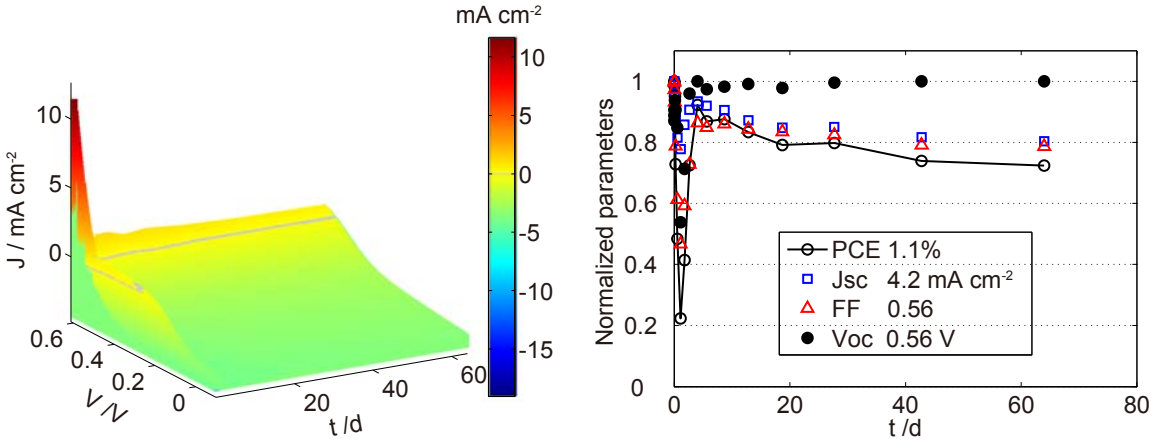

Figure 5–22 (left) J-V-time valley of an AlTi-OSC with a structure of PEDOT:PSS-PAL-BCP-Ti (2 nm)-Al (100 nm). (Right) Normalized parameters of the AlTi-OSC.

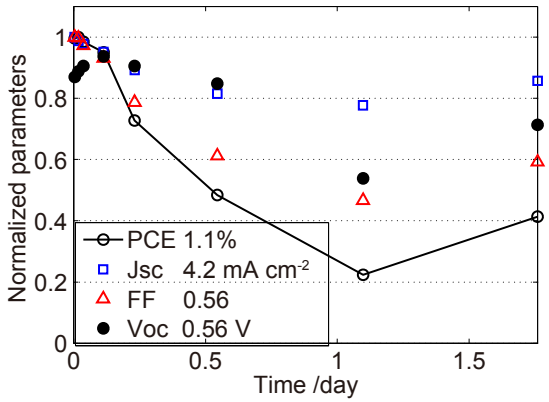

Figure 5–23 Normalized performance of the device shown in Figure 5–22 in the initial two days.

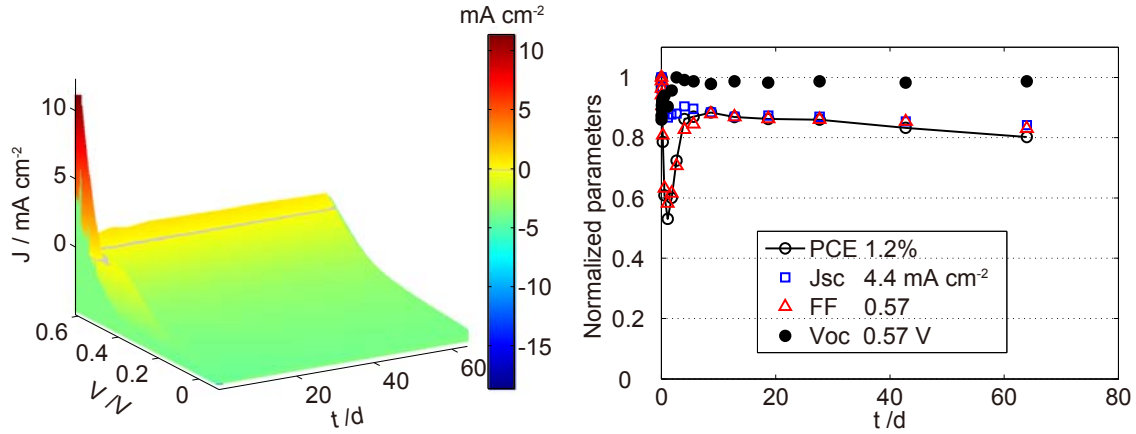

Figure 5–24 (left) J-V-time valley of an AlTi-OSC with a structure of PEDOT:PSS-PAL-BCP-Ti (4 nm)-Al (100 nm). (Right) Normalized parameters of the AlTi-OSC.

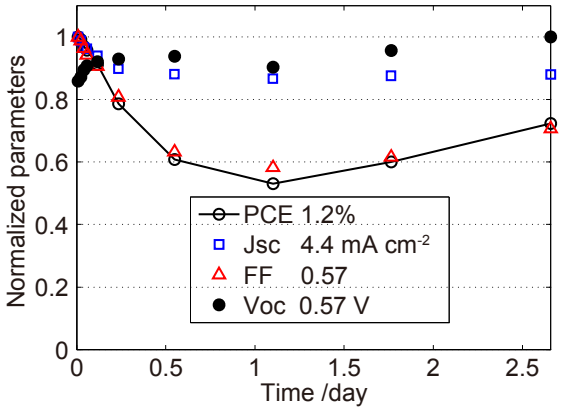

Figure 5–25 Normalized performance of the device shown in Figure 5–24 in the initial two days.

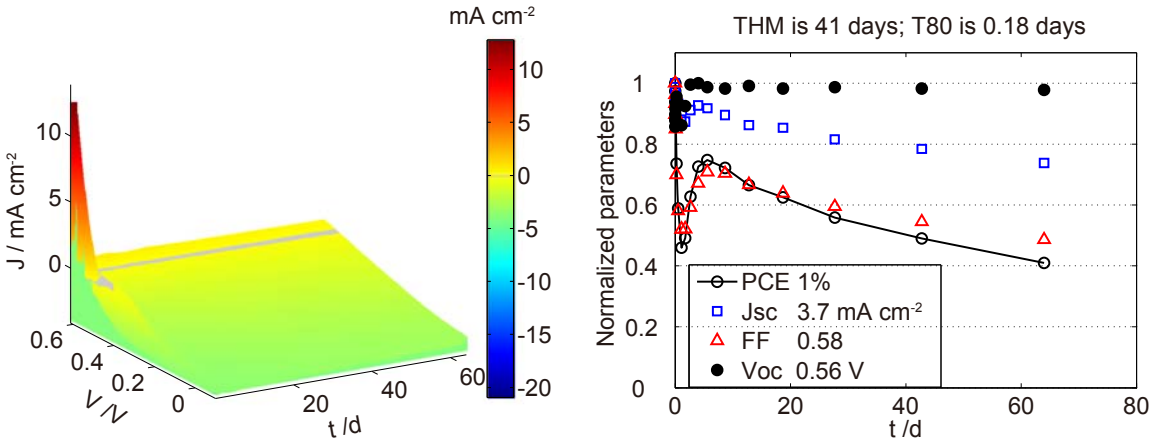

Figure 5–26 (left) J-V-time valley of an AlTi-OSC with a structure of PEDOT:PSS-PAL-BCP-Ti (8 nm)-Al (100 nm). (Right) Normalized parameters of the AlTi-OSC.

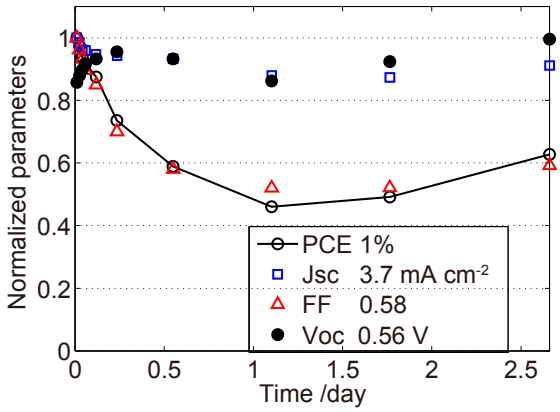

Figure 5–27 Normalized performance of the device shown in Figure 5–26 in the initial two days.

The intensity of an electromagnetic wave $E = E_0 \exp[i(kr - \omega t)]$ is proportional to the amplitude square $|E|^2$. Using a transfer matrix method, [158, 159] we calculated the one-dimensional distribution of $|E|^2$ of the 633 nm light (EQE of a CuPc/C_{60} Al-OSC is highest around this wavelength [160]) in an AlTi-OSC with different thicknesses of Ti. The modeling structure is glass (0.7 mm)/ITO (150 nm)/PEDOT:PSS (50 nm)/CuPc (20 nm)/C_{60} (40 nm)/BCP (8 nm)/Ti (*x* nm)/Al (100 nm).

Results shown in *Figure 5*–28 indicate that the light intensity at the interface of CuPc and C_{60} slightly increases with increasing Ti thickness from 0 to 12 nm and then decreases with further increasing Ti thickness. This might contribute to the increase of PCE with increasing Ti thickness from 0 to 4 nm. Nevertheless, J_{SC} is an integral result of many factors, like the work functions of electrodes, which depends on the thickness (coverage) of the titanium layer. Increasing Ti thickness may decrease the charge transport possibility.

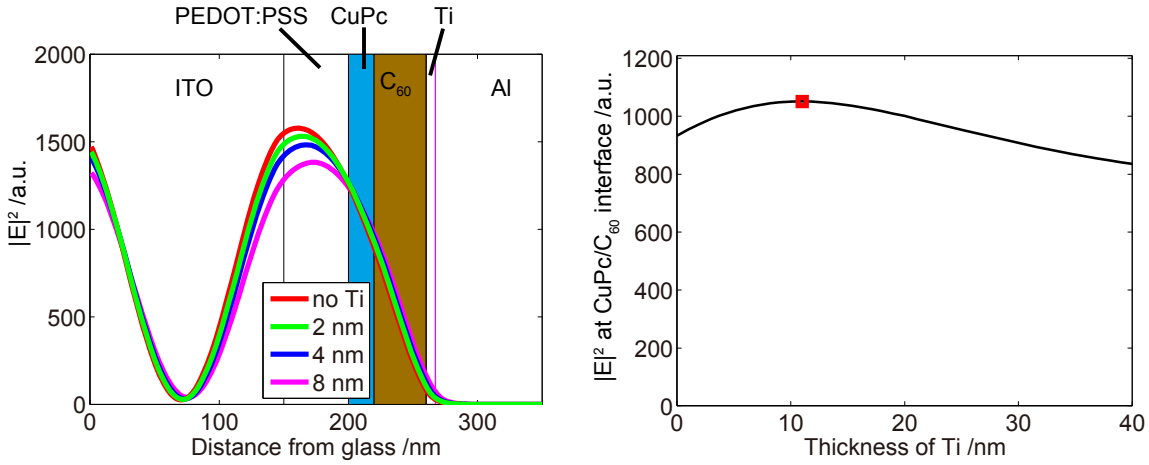

Figure 5–28 (left) calculated distribution of $|E|^2$ of light (λ_{vacuum} = 633 nm) incident from the glass side. (Right) calculated distribution of $|E|^2$ of the incident light at the CuPc/C_{60} interface, as a function of Ti layer thicknesses. The maximum $|E|^2$ marked with the reddish square corresponds to 12 nm Ti.

5.7. MoO_3-PAL-BCP-Ti-Al

Devices with a structure of ITO (150 nm)/MoO_3 (5 nm)/CuPc (20 nm)/C_{60} (40 nm)/BCP (8 nm)/Ti (2 nm)/Al (100 nm) with an active area of 0.06 cm^2 were fabricated and tested similarly as above. The performance of one cell is shown in *Figure 5*–29. Devices with MoO_3 as HTLs were not so stable as those with PEDOT:PSS as HTLs discussed above. P_{TOTAL} of the device shown in *Figure 5*–29 was 2.7 kJ cm^{-2} within the initial 4 months. It notes that another MoO_3-AlTi-OSC (*Figure 5*–40) with the same structure showed a relatively higher PCE at the maximum PCE moment, compared to PEDOT:PSS-AlTi-OSCs from the same batch.

The MoO_3-AlTi-OSCs were less stable than PEDOT:PSS-AlTi-OSCs. This finding is inconsistent with those reported in previous studies which show that when TiO_x is used as the ETL, devices with HTLs of MoO_3 are more stable than devices with HTLs of PEODT:PSS. [161] This difference suggests that stabilization mechanisms in the AlTi-OSCs are probably different from those in the TiO_x devices.

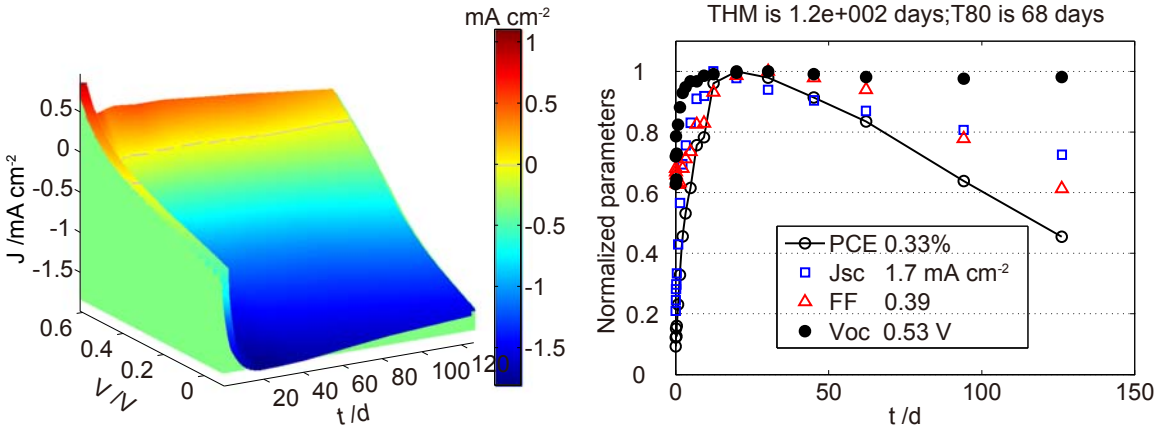

Figure 5–29 (left) J-V-time valley of an AlTi-OSC with a structure of MoO_3-PAL-BCP-Ti-Al. (Right) Normalized parameters of the AlTi-OSC.

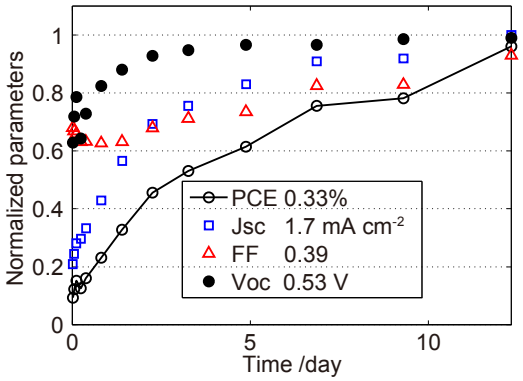

Figure 5–30 Normalized performance of the device shown in Figure 5–29 in the initial two weeks.

5.8. Accelerated degradation

The extended lifetime of organic solar cells have necessitated accelerated degradation tests that can be carried out in lab in a relatively short term. [73] There are mainly three types of acceleration methods, including the thermally accelerated test, the over-humidity accelerated test, and the concentrated sunlight accelerated test.

The thermally accelerated degradation test is based on the hypothesis that the degradation constitutes a series of chemical reactions with reaction rates following the Arrhenius equation $k = A_0 \exp(-E_a/(RT))$, where A_0 is the prefactor, E_a the activation energy and R the gas constant. Also, for the diffusion-dominated degradation, the diffusion coefficient D depends exponentially on the temperature T in a similar way.

The over-humidity (e.g. RH ≥ 85%) accelerated degradation test is based on the hypothesis that the rate of water-induced degradation is proportional to the concentration of water, which follows Fick's first diffusion law (Equation 4-10 in Chapter 4).

The concentrated-sunlight accelerated degradation test is based on two acceleration effects of the intense irradiation. One is the thermal effect, and the other is related with the photo-induced chemical reactions proceeding with a speed decided by the population of photo-excited states.

One common drawback of these methods is that each method involves at least two accelerated processes, making it difficult to correlate the results tested under an acceleration condition with those tested under normal conditions. A consensus on the study of stability of OSCs has been reached in 2011. [74] The indoor weathering test defined in this consensus employs solar simulators for aging of the specimen under irradiation in indoor conditions. [73]

5.8.1. Weathering

We chose two AlTi-OSCs with a structure of ITO (150 nm)/PEDOT:PSS (60 nm)/CuPc (25 nm)/C_{60} (40 nm)/LiF (1.5 nm)/Ti (2 nm)/Al (100 nm) (same structure as those discussed in Section 5.4) to test their weathering stability. One encapsulated device and one unencapsulated device with similar initial performances were chosen from one batch for comparison.

Both devices had almost the same performance throughout the weathering tests over 3 months, as shown in from *Figure 5*–31 to *Figure 5*–36. Here, blue and red points represent data tested at room temperature and 65 °C, respectively. We continued tracing both devices after the weathering tests. The overall performances of them in eight months are shown in *Figure 5*–31 and on the left of *Figure 5*–33.

5.8.1.1. Encapsulated AlTi-OSC

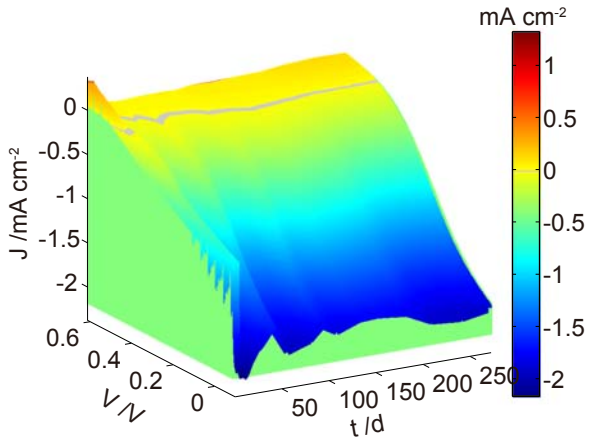

Figure 5–31 J-V-time valley of the encapsulated AlTi-OSC over time, including the three months of weathering tests.

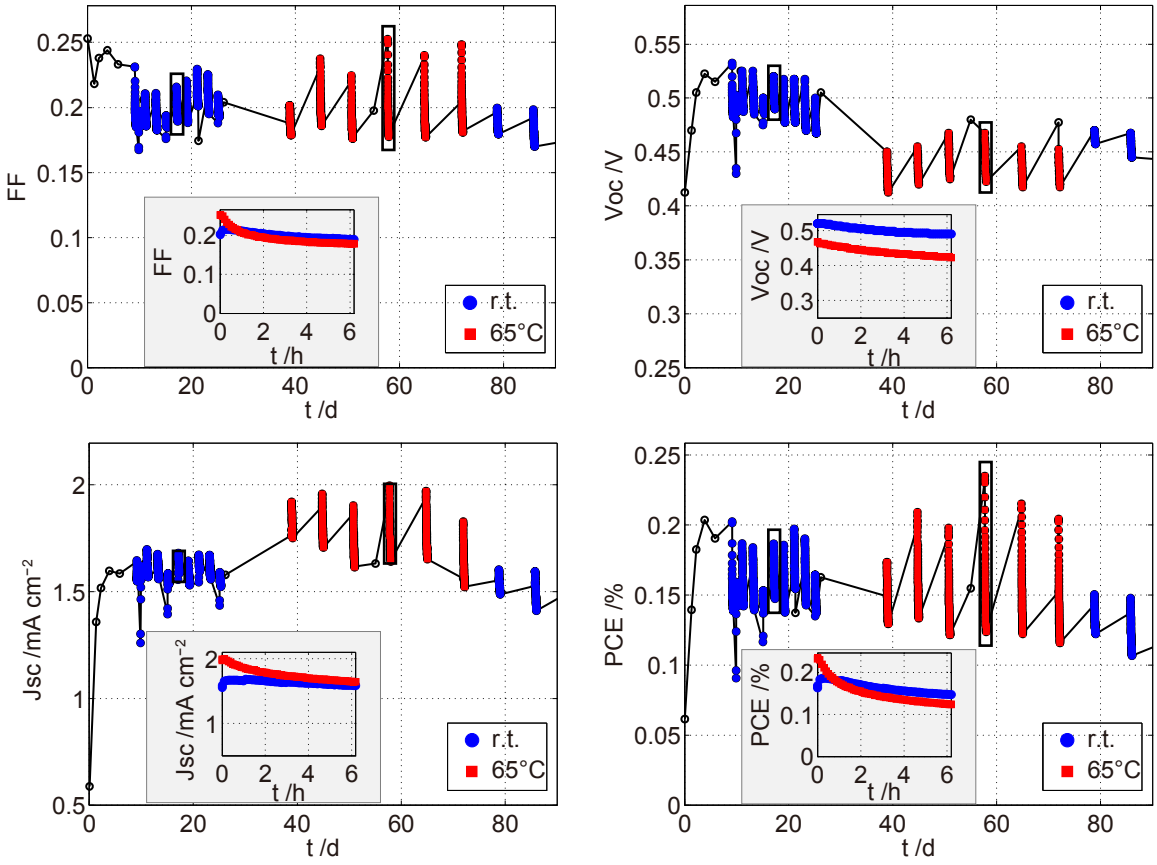

Figure 5–32 Evolutions of parameters of the encapsulated AlTi-OSC shown in Figure 5–31 under weathering tests at different temperatures, i.e. room temperature (blue) and 65 °C (red). Insets show evolutions of parameters in the framed periods marked in the related figures.

The overall long-term evolutions of key parameters of the encapsulated device during the 3 months of weathering are shown in *Figure 5*–32. The processes include instances of

114 h of 1-sun irradiation and idle periods. During each instance of 6.3 h 1-sun irradiation at room temperature, its PCE showed a rapid increase at first and then monotonically decreased (bottom right inset of *Figure 5*–32).

Under the continuous irradiation lasting 6.3 h at room temperature, *FF* and J_{SC} also first increased and then decreased, while V_{OC} monotonously decreased. Under the continuous irradiation lasting 6.3 h at 65 °C, all parameters decreased monotonously. Therefore, we attributed the initial increases of parameters under continuous irradiation at room temperature to the thermal effect of light.

5.8.1.2. Unencapsulated AlTi-OSC

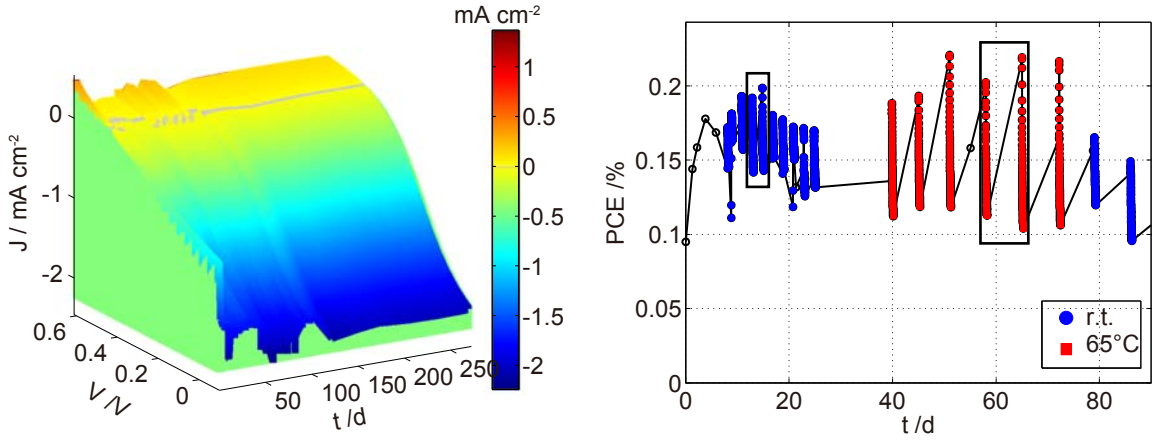

Figure 5–33 Performance of the unencapsulated AlTi-OSC under weathering tests over time. (Left) *J-V-time* valley of the device; (Right) long-term performance of the device. Boxes represent the periods corresponding to the data shown in Figure 5–37.

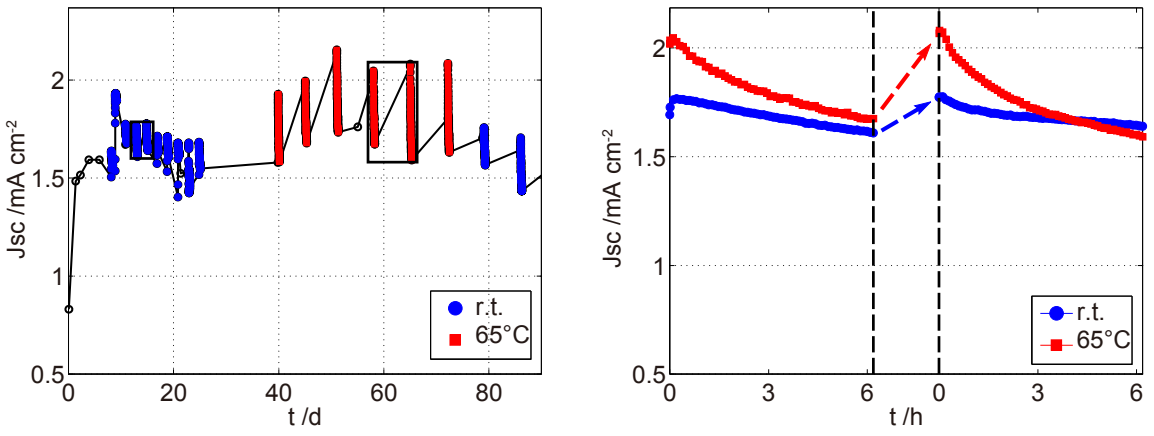

Figure 5–34 Evolution of J_{SC} of the unencapsulated AlTi-OSC under weathering tests at different temperatures: (left) long-term; (right) in the two marked successive cycles.

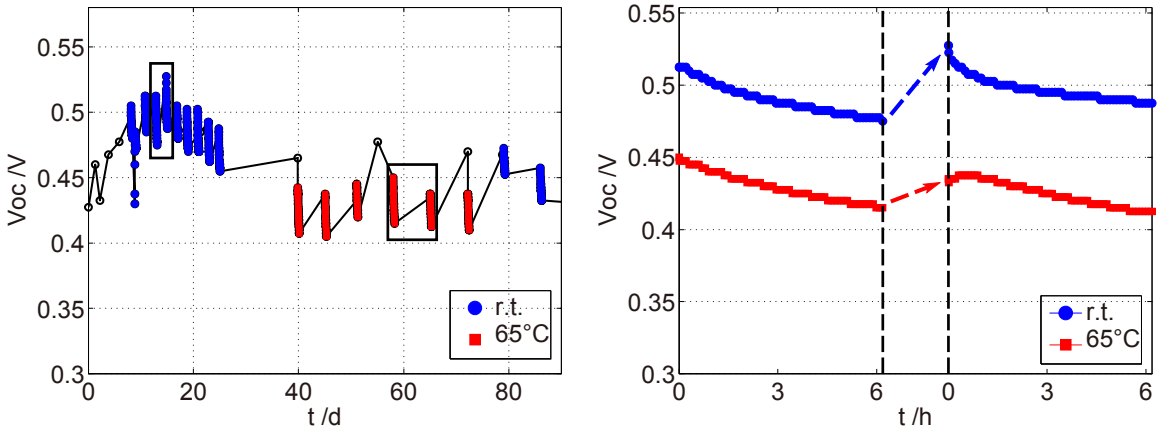

Figure 5–35 Evolution of V_{OC} of the unencapsulated AlTi-OSC under weathering tests at different temperatures: (left) long-term; (right) in two successive cycles.

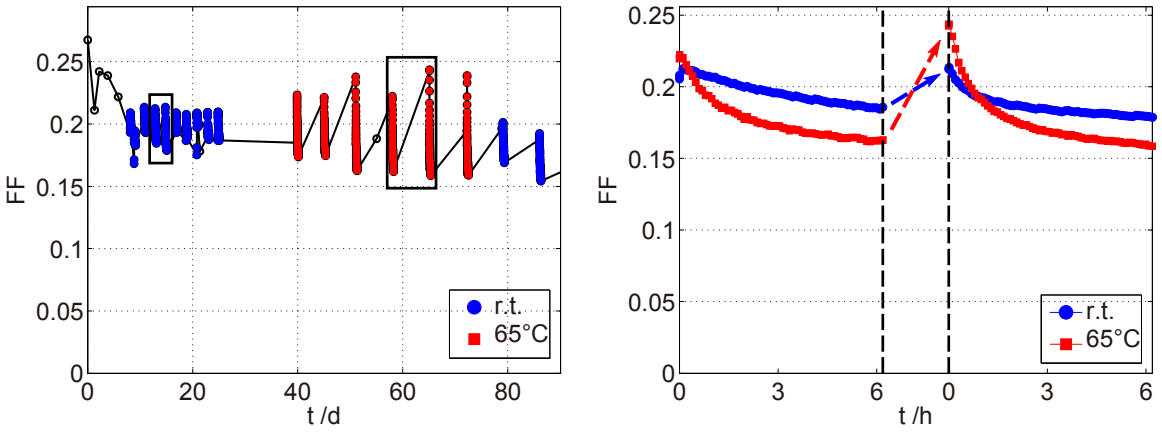

Figure 5–36 Evolution of FF of the unencapsulated AlTi-OSC under weathering tests at different temperatures: (left) long-term; (right) in successive cycles.

The overall long-term evolutions of key parameters of the encapsulated device during the 3 months of weathering tests are shown in from *Figure 5*–33 to *Figure 5*–36. The unencapsulated AlTi-OSC and the above discussed encapsulated AlTi-OSC performed similarly in each parameter, either at room temperature, or at 65 °C.

5.8.1.3. Recovery of performance after weathering

It is very important to note that the decrease in performance of this unencapsulated device under the weathering test was almost fully restored during the idle period (between the two dashed vertical lines in *Figure 5*–37). As far as we are aware, such a recovering capability has only been found in encapsulated OSCs with ZnO as the HTL, [162] indicating that the bilayer cathode was probably self-encapsulated. In the same report, the authors further show that the conductivity of the cell (shunting) was significantly improved after high intensity light exposure. The photo-induced reversible degradation is attributed to the temporal oxygen desorption of ZnO, whereas the recovery in the dark is

attributed to the re-chemisorption of oxygen of ZnO. We speculate that similar processes existed in the recoverable degradation of AlTi-OSCs under weathering tests. This similarity also suggests that the air intrusion, which causes rapid degradation of unencapsulated organic solar cells, was almost totally inhibited in the AlTi-OSCs.

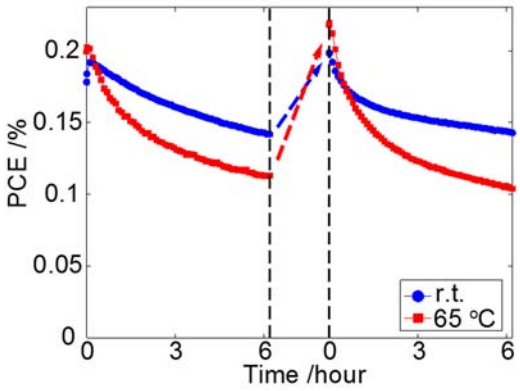

Figure 5–37 PCE of the device shown in Figure 5–33 in two successive cycles at different temperatures. The period between the vertical dashed lines indicates the idle periods between measurements: 46 h for the room-temperature weathering and 169 h for the 65 ^{o}C weathering.

5.8.2. Over-humidity

5.8.2.1. Effect of humidity on Al-OSCs

Fabricated OSCs were exposed in the ambient air with varied humidity. Aluminum reacts with pure water particularly at a relatively high temperature, forming an amorphous insulating oxide. [163] Grain-boundaries in the aluminum cathode of an OSC are permeable to water. The humidity in the storage ambience influenced the stability of Al-OSCs. We took the averaged RH [164] throughout the cells' lives to statistically analyze the effect of humidity on their shelf lives. Dozens of LiF-Al-OSCs, having the same structure as the one shown in *Figure 5*–3, were chosen and analyzed. The results are shown in *Figure 5*–38. Devices stored in a low-humidity environment (RH < 50%) degraded relatively slowly, while devices stored in a high-humidity environment degraded relatively fast. It notes that this analysis did not exclude the influence from other environmental variables like the light exposure, T_{open}, or T_{final} (see Section 2.3.4). The latter two factors influenced the stability of fabricated OSCs by influencing the pre-oxidation of the cathode interfaces.

Upon exposure in air, Al-OSCs sometimes form cracks on the surface, especially for devices whose cathodes were deposited in the bell-shape chamber with a relatively high T_{final}. The device shown on the right of *Figure 5*–38 was fabricated in this chamber with a T_{final} of 190 ^{o}C. A coarse and amorphous Al_2O_3 interlayer was presumably formed under such a high temperature. The coarse film was more permeable to water compared to a

flat film, and finally the abundantly inhaled moisture caused the rupture of the metal cathode.

It is easy to prove that such cracks are related with water. Exhaling upon a fabricated device instantaneously caused such wrinkles on the aluminum surface, as the dew point of exhaled moisture was close to the surface temperature of the device (~20 °C).

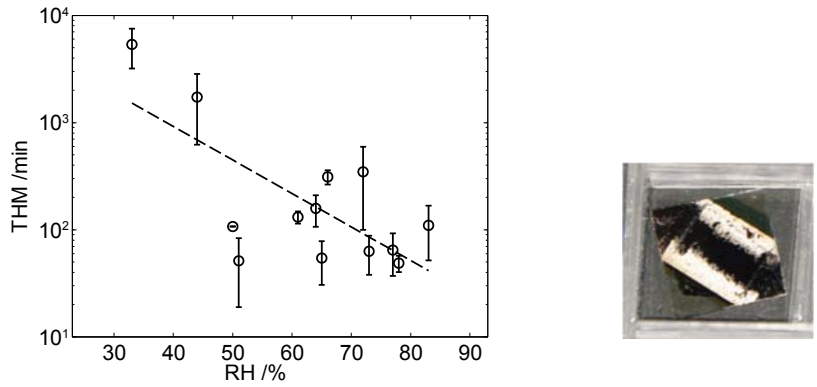

Figure 5–38 (left) THMs of decades of Al-OSCs fabricated in environments with varied relative humidity. (Right) An Al-OSC-D with a structure of ITO (150 nm)/PEODT:PSS (60 nm)/CuPc (25 nm)/ZnPc (1.2 nm)/C_{60} (40 nm)/LiF (2 nm)/Al (75 nm) after being stored in air in the dark box (Figure 3–3 in Chapter 3) for four days.

5.8.2.2. Effect of over-humidity on AlTi-OSCs

The normal ambience with an RH lower than 85% did not influence the shelf stability of AlTi-OSCs, irrespective of the existence of moisture sensitive buffer layers like BCP. This was perhaps because titanium does not react with or introduce water from the ambient air. We checked whether the AlTi-OSCs could resist a higher humidity, e.g. RH > 90%, with the following experiments.

We used a beaker with water on the bottom to generate an over-humidity environment. An atmosphere with an RH as high as 95% was achieved by heating the beaker to about 50 °C for 1 hour and then let it cool down naturally to room temperature (19 °C). We chose two stabilized AlTi-OSCs for comparison. One is a PEDOT:PSS-LiF-AlTi-OSC, and the other is a MoO_3-BCP-AlTi-OSC. By comparing behaviors of these cells having different buffer layers in such an over-humidity environment, we could identify which layer was more sensitive to moisture.

The PEDOT:PSS-LiF-AlTi-OSC with a structure of ITO (150 nm)/PEDOT:PSS (60 nm)/CuPc (20 nm)/C_{60} (40 nm)/LiF (1.5 nm)/Ti (2 nm)/Al (100 nm) and the MoO_3-BCP-AlTi-OSC with a structure of ITO (150 nm)/MoO_3 (5 nm)/CuPc (20 nm)/C_{60} (40 nm)/BCP (8 nm)/Ti (2 nm)/Al (100 nm) were fabricated and intermittently tested as normal in air over decades of days before they were stored in the beaker for 12 h. We recorded the ambient RH in the beaker with a humidity logger (EL-USB-2). The performances as well as the recorded RH are shown in *Figure 5*–39 and *Figure 5*–40.

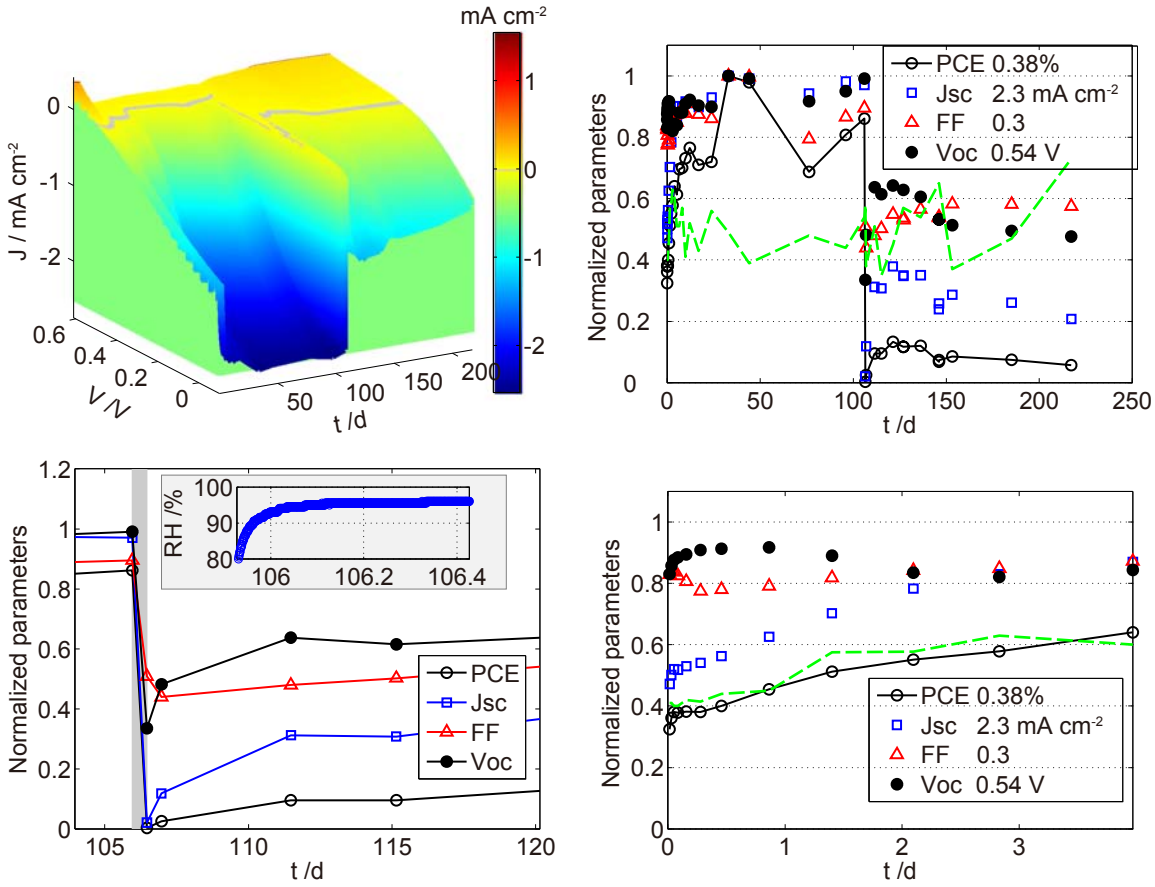

Figure 5–39 Performance of an AlTi-OSC with a structure of ITO-PEDOT:PSS-PAL-LiF-Ti-Al experiencing an over-humidity test. All time axes are consistent. The top left figure is the *J-V-time* valley. The variation of RH in the storage ambience of this cell is shown in the right-side figures with the greenish dashed curve (percentage expressed as decimal). The gray patch in the bottom left figure corresponds to the over-humidity testing period. The RH during this period is shown in the inset. The bottom right figure shows the initial performance.

The PEDOT:PSS-LiF-AlTi-OSC was completely inactivated in the ambience with an RH reaching 96%. The cathode film was seriously ruptured in the beaker. After the over-humidity test, we continued to trace its performance in the next months and found that only about 10% performance was recovered. One explanation of this recovery is that the bilayer cathode was self-healed to some degree. Another explanation is that some photochemical sections were formed, similarly to the situation in Ti-OSCs. Similar recovery phenomenon was also observed for the MoO_3-BCP-AlTi-OSC discussed below.

The surface of the MoO_3-BCP-AlTi-OSC was uniformly ruptured in the over-humidity environment (final RH of 91%). The cathode of the BCP-AlTi-OSC started to be broken down after about 3 hours in the over-humidity environment, corresponding to RH over 85%. Cracks on the aluminum cathode also showed some self-closing, as indicated by the recovery of performance shown on the top right of Figure 5–40.

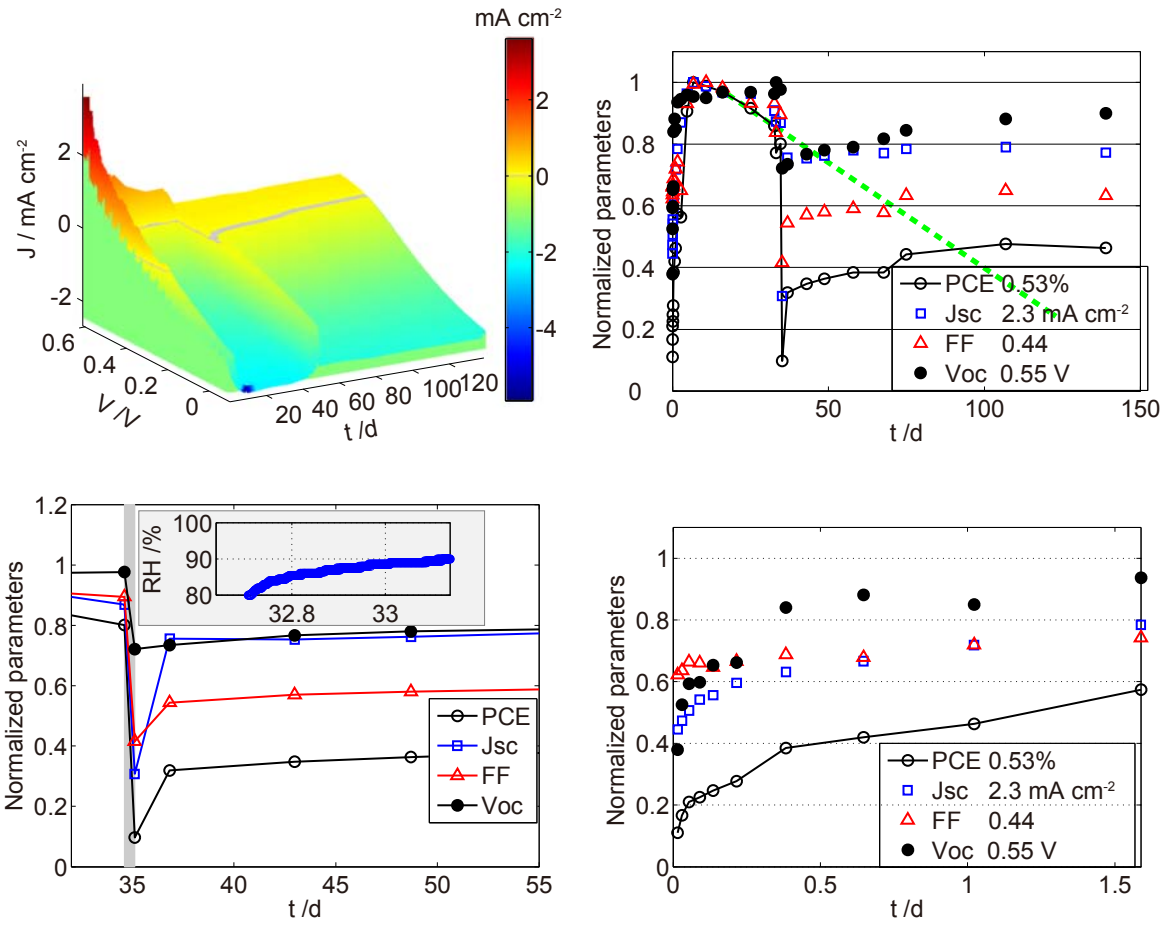

Figure 5–40 Performance of an AlTi-OSC with a structure of ITO-MoO_3-PAL-BCP-Ti-Al experiencing an over-humidity test. All time axes are consistent. The top left figure is the J-V-t valley. The average degradation tendency of this cell before the over-humidity test is marked by the greenish dashline in the top right figure. The gray vertical patch in the bottom left figure corresponds to the over-humidity testing period. The RH during this period is shown in the inset. The bottom right figure shows the initial performance.

Figure 5–41 shows the comparison between cracks formed on cathodes of both devices after the over-humidity tests. Interestingly, the cracks on the LiF-AlTi-OSC (left-side figure) mainly appeared in the region where LiF was deposited (region A), whereas the region without LiF (region B) was less affected by the high humidity. The LiF boundary was formed as a result of the different evaporating directions of Al and LiF sources. It also suggests that the PEDOT:PSS film was not related with the formation of these cracks. On the contrary, the cracks on the MoO_3-BCP-AlTi-OSC (right-side figure in *Figure 5*–41) dispersed uniformly, as the beneath BCP layer was uniformly deposited.

We speculate that these cracks are related with the moisture adsorption by polar substances beneath the cathode. Polar substances like LiF (or AlF_x) or BCP facilitated the water adsorption, thereby accelerating the formation of cracks in cathodes. However,

under normal humidity, the adsorbed water rarely affected the adjacent cathode composed of titanium (partly oxidized), which is totally resistant to water.

The above-discussed effects of humidity on the cathodes of OSCs suggest that water in air could penetrate the cathode, at least penetrate the aluminum layer. Nevertheless, as titanium does not react with water, resistance of AlTi-OSCs to normal humidity is sufficiently high.

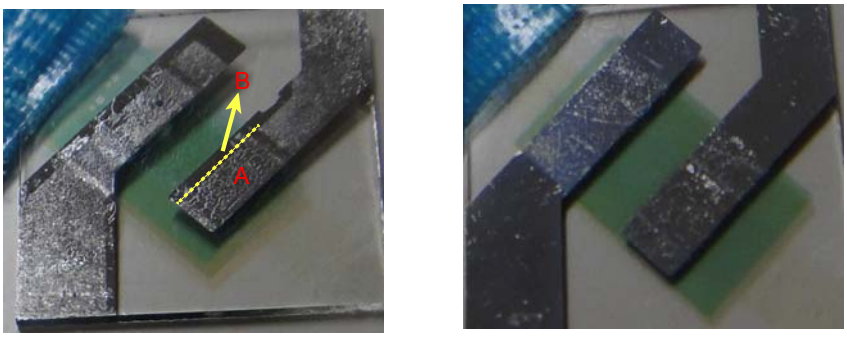

Figure 5–41 Cracks on the two AlTi-OSCs after the over-humidity tests. The right-side device in the left-side figure is the device with the performance shown in Figure 5–39. It has a clear boundary (dotted) dividing the cell into two regions: region A with LiF and region B without LiF. The right-side device in the right-side figure is the AlTi-OSC with the performance shown in Figure 5–40.

5.9. Stabilization mechanism of the bilayer cathode

In this section, we discuss the stabilization mechanisms of Ti-Al bilayer cathodes, from perspectives of both surface observations and elemental depth profiles.

5.9.1. Elimination of pinholes

The pinholes in the aluminum cathodes were probably caused partly by wrinkled surfaces of the organic layers after the pre-annealing. These pinholes were observable under a microscope of either optical or atomic force type. We found that these pinholes were completely annihilated in AlTi-OSCs, even though they were pre-annealed in a same way as Al-OSCs.

We chose three fabricated devices, i.e. an Al-OSC, a Ti-OSC and an AlTi-OSC for comparison. These three devices were pre-annealed on a 155 ^{o}C hot plate for 10 min in Ar before the deposition of LiF. After exposed in air for 24 days (Al-OSC), 4 days (Ti-OSC) and 24 days (AlTi-OSC), we analyzed their surface morphology with the contact-mode AFM. The results are shown in *Figure 5*–42.

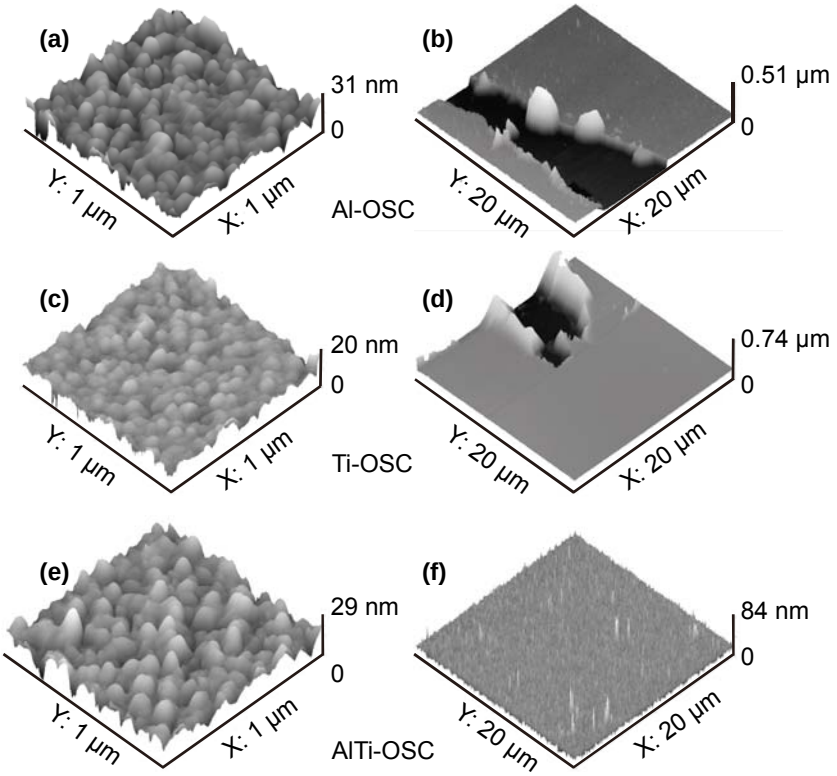

Figure 5–42 AFM images of an Al-OSC (top two), a Ti-OSC (middle two) and an AlTi-OSC (bottom two). (a) Grains on the surface of the Al-OSC, within an area of 1 × 1 μm^2. (b) Part of a microscopic crack, with a depth of about 100 nm, of the aluminum layer of the Al-OSC, within an area of 20× 20 μm^2. Cracks with such sizes were observable under an optical microscope. (c) Grains on the titanium surface of the Ti-OSC. (d) Part of a microscopic crack, with a depth of about 160 nm, of the titanium layer of the Ti-OSC. (e) Grains on the aluminum surface of the AlTi-OSC. (f) Surface morphology of the AlTi-OSC. No microscopic crack was observed on the AlTi-OSC.

On a nanoscale, these three devices had a lot of round grains on the surfaces, with root-mean-square (rms) roughnesses of 3.0 nm (Al-OSC), 2.4 nm (Ti-OSC) and 3.3 nm (AlTi-OSC). The average size of Ti grains is smaller than that of Al grains.

On the microscopic scale, both Al-OSC and Ti-OSC had pinholes, whereas the entire AlTi-OSC had no pinhole. The observed pinhole in the Al-OSC [*Figure 5*–42(b)] had a depth equal to the thickness of the aluminum cathode, whereas the pinhole in the Ti-OSC [*Figure 5*–42(d)] is deeper than the titanium cathode. These depths indicate that the pinhole on the Ti-OSC was caused by the bombardment of titanium clusters during the deposition of titanium at a relatively fast deposition rate, whereas the pinhole on the Al-OSC was presumably related with the surface energy of aluminum during the deposition.

On the contrary, no pinhole was observed on the entire AlTi-OSC [*Figure 5*–42(f)]. This microscopic difference was probably related with the well-known Al grain refinement effect of Ti. [165] Another interesting feature of the AlTi system is that cracks of oxide

scales on the surface of a titanium-aluminum alloy can be healed after a heat treatment. [166]

5.9.2. Interdiffusion blocker

We characterized the elemental depth profiles in three devices. Unlike other relevant reports in which metal cathodes were peeled off before tests, [77, 87] we retained the cathodes in order to examine the chemical information at cathode-organic interfaces. The Al-OSC had completely degraded in air in two months in air. The Ti-OSC had degraded to a stable low-performance stage resembling that shown in *Figure 5*–10. The AlTi-OSC had ceased its increase of performance in air, resembling that shown in *Figure 5*–12. The following results suggest that one of the functions of the titanium layer in the OSCs is a diffusion blocker between the aluminum (including LiF) layer and the organic layers.

5.9.2.1. TOF-SIMS cations

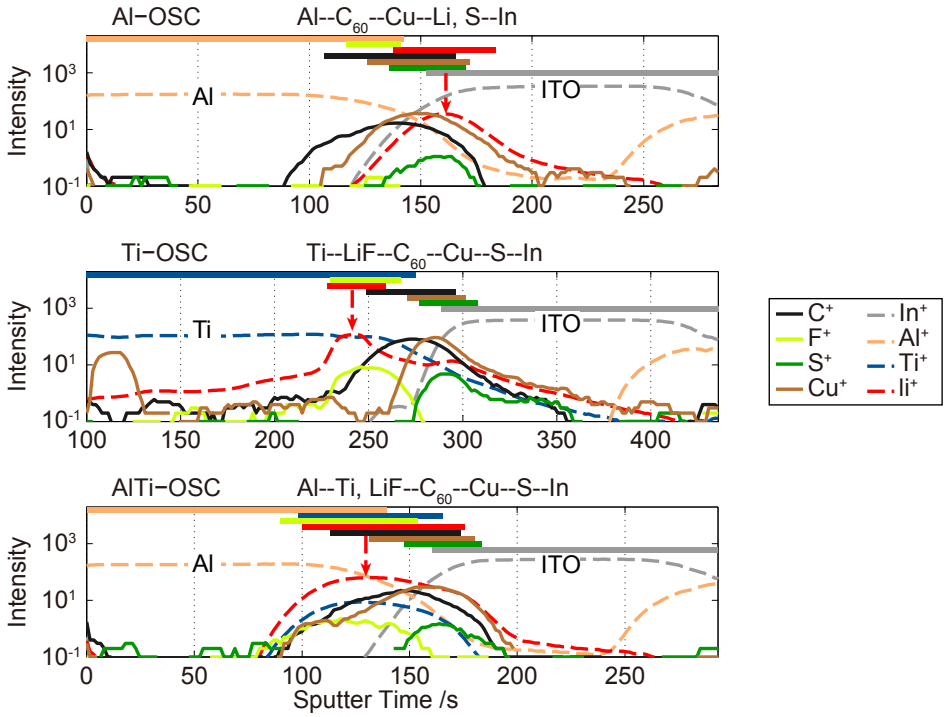

Figure 5–43 Depth profiles of electropositive ions sputtered from three devices: Al-OSC (top), Ti-OSC (middle) and AlTi-OSC (bottom). The intensities of In^+, Al^+, Ti^+, and Li^+ were divided by 100 for practical reason. The vertical layer sequence represented by each feature element was noted on the top of the related figures. Peak positions of Li were indicated by the vertical arrows. The color bars on the top of each figure represent regions cut at fifth of maximum intensity of the related cations.

The depth profiles of electropositive ions (cations) in these devices are shown in *Figure 5*–43. The profiles were broadened by the sputtering ions, as indicated by the seriously

overlapping profiles. Nevertheless, it is possible to identify positions of layers with related cations: ITO (In^+), PEDOT:PSS (S^+), CuPc (Cu^+), C60 (C^+ ahead of Cu^+), LiF (Li^+ and F^+), Al (Al^+) and Ti (Ti^+).

In the Al-OSC, Li diffused into the PEDOT:PSS layer, whereas F was hard to be detected, except a trace amount detected in the aluminum layer. The diffusion of Li was presumably a consequence of the reaction of LiF with Al, during which Li atoms were formed. [44] The dissociated Li atoms diffuse in the organic layers, [45] and further reacted with PSS^- in the PEDOT:PSS layer. The dissociation and diffusion of LiF may cause the reduction of V_{OC} of OSCs. [77]

On the contrary, Li and F were found to be located at the same position in the Ti-OSC and AlTi-OSC. One possible explanation is that LiF did not react with Ti, and the strong ionic bonding of LiF made it difficult for LiF to diffuse through the electrically neutral organic films.

5.9.2.2. TOF-SIMS anions

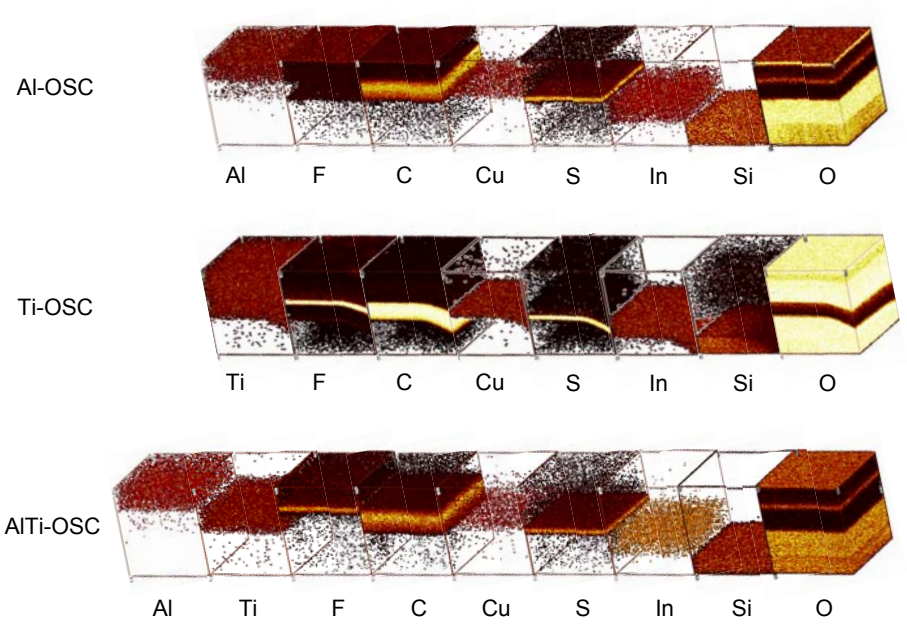

Figure 5–44 Three-dimensional distributions of anions in the Al-OSC (upper), in the Ti-OSC (middle) and in the AlTi-OSC (bottom).

We also detected the distribution of electronegative ions (anions) sputtered from these devices at different locations. The results are shown in *Figure 5*–44. The related feature anions of different layers were Al (Al^-), Ti (Ti^-), LiF (F^-), C_{60} (C^- ahead of Cu^-), CuPc (Cu^-), PEDOT:PSS (S^-) and ITO (In^-). The sputtered area on the Ti-OSC had a large pinhole, as indicated by the collectively tilted distributions of anions at the right-side edge. Another interesting indication from the 3-D element distributions is that oxygen was extraordinarily rich in the Ti layer of the Ti-OSC. It suggests that the oxygen resistance of titanium layer was too low to protect the inner organic layers.

Depth profiles of anions in the Al-OSC and in the AlTi-OSC are shown in *Figure 5*–45. The aluminum in the Al-OSC intermixes with the C_{60} layer, whereas the intermixing of Al and C_{60} in the AlTi-OSC is not significant. Consequently, we inferred that in the presence of titanium, the interdiffusion of aluminum and C_{60} is much reduced. It notes that titanium was found to be an effective diffusion blocker between aluminum and silicon in integrated circuit. [167] The self-diffusion of aluminum in Ti (α-form) is a vacancy-controlled diffusion and negligible at room temperature. [155]

Although titanium itself seemed to have diffused into the organic layer, the subsequently oxidized titanium does not block charge (electron) transport in devices. It notes that ETLs like CrO_x have also been reported to stop the interdiffusion of aluminum into the organic layers during deposition. [88]

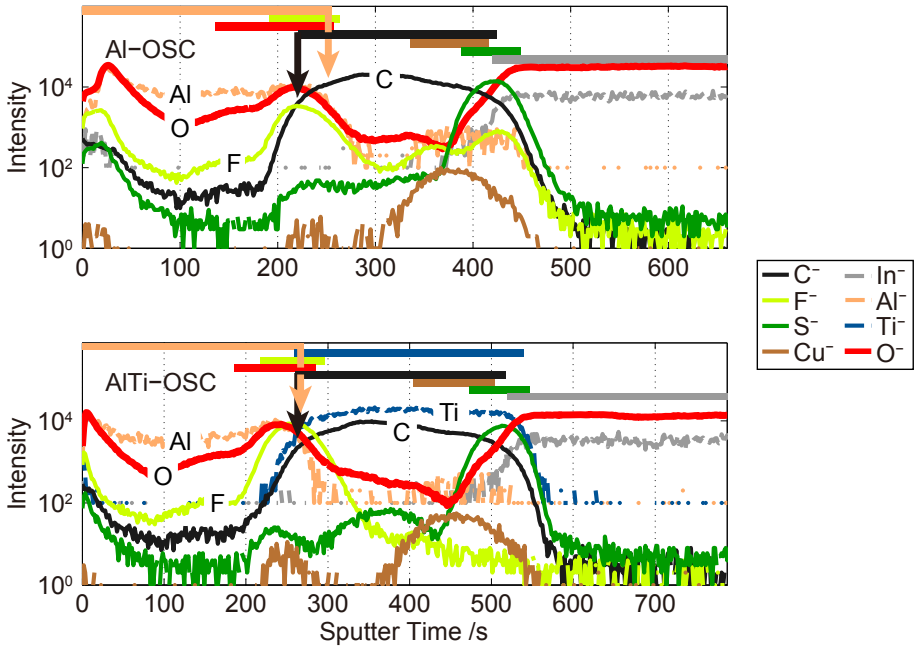

Figure 5–45 Depth profiles of anions sputtered from two devices: Al-OSC (top) and AlTi-OSC (bottom). Intensities of In^-, Al^-, and Ti^- were multiplied by 100 for practical reason. The color bars on the top of each figure represent regions cut at fifth of maximum intensities of the related anions. Edges of Al and C_{60} bars were indicated with the vertical arrows.

5.9.3. Sustained oxygen scavenger

Sensitivities of TOF-SIMS to different ions are varied. Generally, it is impossible to quantitatively analyze the content of an element merely using TOF-SIMS. However, it is possible to compare the intensities of one type of ion among different samples with some reference points where the content of this specific ion is invariant among these samples. Here we chose the outer surfaces of aluminum as the oxygen reference between the Al-OSC and AlTi-OSC. The degrees of oxidization of both surfaces should be identical, as they had been exposed in air under the same conditions for the same

period. Based on this postulate, we normalized the intensities of O^- in both devices to the peak oxygen intensities nearby the aluminum surfaces. The contents of aluminum in both devices were normalized in the same way.

To compare the vertical locations of peak intensities of O^- in both devices, we further realigned the sputter time axes with two reference points, one is the initial peak position of O^- and the other is the edge of the ITO layer. The realigned and normalized data are shown in *Figure 5*–46. The O^- intensities in ITO layers in both devices were at the same level, insuring the reliability of such data treatments.

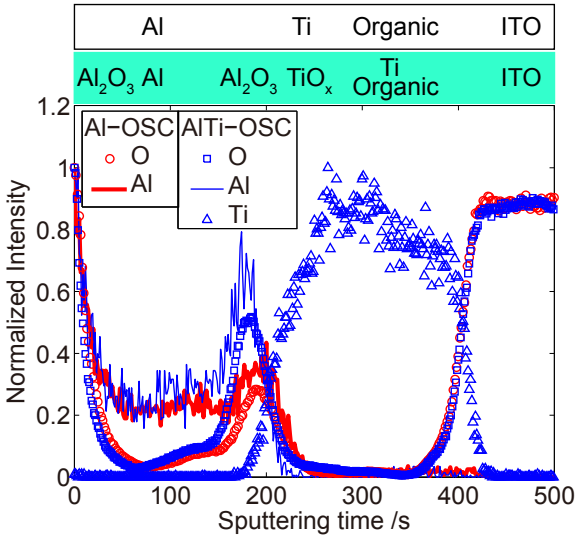

Figure 5–46 Distributions of oxygen and metal elements in the Al-OSC and in the AlTi-OSC. Both axes were realigned as explained in the text for the sake of quantitative comparison. The layer stacking according to deposition sequence and the actual layer stacking according to the tested anions are shown on the top.

According to *Figure 5*–46, three findings are inferred. First, oxygen in the Al-OSC is less than that in the AlTi-OSC. Second, peak position of oxygen in the AlTi-OSC locates in the aluminum layer. Third, titanium in the AlTi-OSC diffuses into organic layers.

The first and the second findings suggest that the aluminum layer, although located farther from the organic layers than the titanium layer, was preferentially oxidized by oxygen effused from the organic side. In normal cases, oxygen prefers to oxidize aluminum in a titanium-aluminum system. [154] The aluminum layer functioned as some kind of sacrificial anode, [168] sustaining the oxygen scavenging of titanium. The total reaction occurring at this metal interface was perhaps like that shown in scheme 5-2, with the titanium being partially oxidized to TiO_x. Such a reaction can also be inferred from the fact that aluminum tends to reduce TiO_2 during deposition in vacuum. [156] As a consequence, the partially oxidized Ti could continue to scavenge oxygen. More importantly, the bilayer system gets passivated during this process.

$$\mathrm{Ti} + \mathrm{Al} \xrightarrow{\mathrm{Air}} \mathrm{TiO_x} + \mathrm{Al_2O_3} \qquad 5\text{-}2$$

The third finding that the titanium mainly existed in the organic layers is presumably a consequence of the diffusion of titanium into organic layers during or after deposition. However, there is still another possibility that the titanium was sputtered into the organic layers during sputtering. In either case, the titanium layer acted as a preferential interdiffusion layer upon organic layers, ensuring that the intermixing between aluminum and organic layers was sufficiently suppressed.

The distributions of oxygen shown in *Figure 5*–46 also suggest that a metal oxides layer comprising Al_2O_3 and TiO_x was formed at the cathode interface of the AlTi-OSC. It notes that this oxides layer was probably composed of binary metal oxides, instead of ternary metal oxides ($Al_xTi_yO_z$). [156] The evolution of energy bands in a LiF-AlTi-OSC is proposed in *Figure 5*–47. The formed metal oxides layer was dense (Al_2O_3) and semiconducting (TiO_x), thereby dramatically slowing down further intrusion of air into organic layers, meanwhile not blocking the transport of electrons through this interface. As mentioned before, interdiffusion at this interface is suppressed as a consequence of the formation of Al_2O_3. [109]

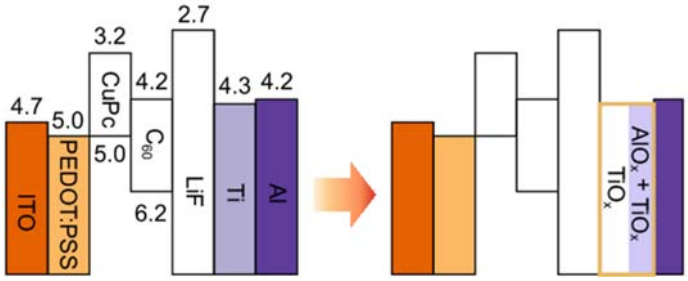

Figure 5–47 Proposed diagram showing evolution of energy levels in AlTi-OSCs when exposed to air. White columns represent band gaps. A dense, semiconducting oxide layer is formed at the interface of the cathode.

Actually, it has been known that aluminum acts as a sacrificial anode in the corrosion process of a bimetallic system of aluminum and another metal like titanium or chromium. [169] This feature suggests that aluminum-chromium cathodes, which protect inverted OSCs in vacuum, [157] might also protect conventional OSCs in air. However, the efficiency might be slightly compromised due to the mismatch between the work function of chromium and the electron affinity of fullerene. Besides, the stability might also be compromised due to the appreciable interdiffusion between chromium and aluminum at room temperature. [170] Related studies will help us to understand the stabilization mechanisms in OSCs deeper.

To summarize, aluminum and titanium form a special interface where aluminum enhances the resistance of titanium to oxygen, whereas titanium possibly enhances the corrosion resistance of aluminum to water. A graph illustrating these mechanisms is shown in Figure 5–48.

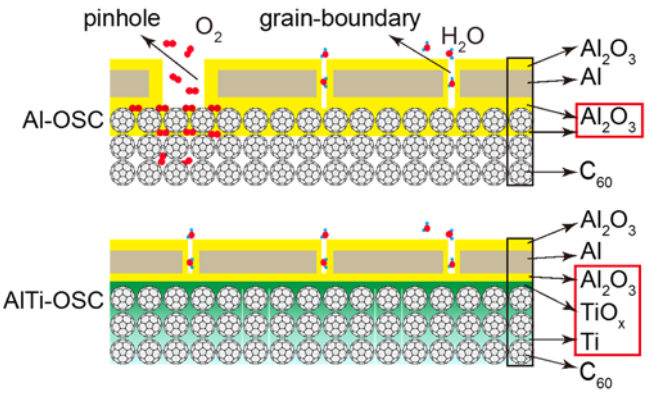

Figure 5–48 Sketch of the possible protection scenario illustrating the proposed stabilization mechanisms in the Ti-Al bilayer-cathode devices based on experimental results.

5.10. Summary

In this Chapter, the stability of small-molecular organic solar cells with different cathodes was discussed, including Al-OSCs with aluminum cathodes, Ti-OSCs with titanium cathodes, and AlTi-OSCs with aluminum-titanium bilayer cathodes. A half-shelf-life of a year has been achieved in the AlTi-OSCs. Effects of different buffer layers on the performance and stability of fabricated devices were also discussed. The stabilization mechanisms of the AlTi bilayer cathode were finally investigated.

We first discussed the performance and stability of unencapsulated Al-OSCs with different buffer layers stored on the shelf. P_{TOTAL} of a PEDOT:PSS-Al-OSC was less than 100 J cm^{-2} within its lifetime, whereas that of a MoO_3-Al-OSC was higher but still less than 200 J cm^{-2} within its lifetime. This means that MoO_3 improves the stability of Al-OSCs in air. Different ETLs including LiF, BCP and TiO_x were used to fabricate Al-OSCs. It notes that two nanometers of TiO_x prepared by oxidizing metal titanium in air did not improve the stability of fabricated Al-OSCs.

We then discussed the performance of unencapsulated Ti-OSCs with HTLs of PEDOT:PSS and ETLs of LiF. These devices degraded more slowly than Al-OSCs in air. One interesting feature phenomenon is that the Ti-OSCs did not permanently completely degrade over at least seven months. Instead, they were stabilized at a fluctuating state with about 20% of their initial performances in air. P_{TOTAL} of the Ti-OSC was 741 J cm^{-2} within 6.5 months.

The main topic of this chapter is AlTi-OSCs. The initial performance and shelf stability of these devices with different buffer layers were discussed. When PEDOT:PSS was used as the HTL, for devices without an ETL, or with an ETL of LiF (or BCP), P_{TOTAL}s were 1.6 kJ cm^{-2} within the initial 4.5 months, 4.9 kJ cm^{-2} within the initial 9 months (5.7 kJ cm^{-2} within

the initial 4.5 months), respectively. For a device with an ETL of BCP and an HTL of MoO_3, P_{TOTAL} was 2.7 kJ cm^{-2} within the initial 4 months.

We also optimized the deposition rate and thickness of the titanium layer in AlTi-OSCs. We found that an AlTi-OSC with 4 nm titanium deposited at 0.1 nm s^{-1} performed the best, both efficiently and durably in air.

To check the stability of these AlTi-OSCs in different envrionments, we carried out two accelerated degradation tests, including a weathering test and another over-humidity test. Under the weathering test, the stability of an air-exposed AlTi-OSC was found to be comparable to that of an encapsulated one. Performances of both cells decreased during the continuous irradiation but would be almost totally recovered in the following idle period. This suggests the self-encapsulation feature of AlTi-OSCs.

We finally examined the stabilization mechanisms of the AlTi bilayer cathodes with both surface observations and elemental depth analysis. We found that the ultrathin titanium layer could annihilate pinholes that were generally observed on either Al-OSCs or Ti-OSCs. By comparing the elemental depth profiles in devices with different cathodes, we proposed that the titanium layer not only blocked the interdiffusion between the cathode (including the ETL) and the organic layers, but also improved the resistance of the cathode to both oxidization and corrosion by forming a special sacrificing structure in which aluminum acted as a preferentially oxidized anode, sustaining the oxygen scavenging of the beneath titanium in air, while titanium acted as a corrosion barrier of aluminum.

Contents discussed in this chapter provided us with an effective and economical approach to prevent the degradation of the extensively studied aluminum-based OSCs. Zero degradation of organic photovoltaic devices exposed to air over at least 3 months can be realized by this means. The in-air long shelf lives of AlTi-OSCs were explained on the basis of some of the superb properties of the Ti-Al interface: (1) pinhole elimination, (2) interdiffusion blocker, and (3) sustainable oxygen scavenging. The Ti-Al bilayer cathode improved the stability of OSCs in air to a new level, and may find potential applications in other air-sensitive aluminum-containing semiconductor devices.[Manual chapter break]

Chapter 6. Conclusions

The aim of this work is the investigation of the stability of small-molecular organic solar cells based on CuPc and C_{60}. We have mainly discussed the following issues:

- Light-induced degradation of organic solar cells
- Modelling of the light-induced degradation of organic solar cells
- Aluminum-titanium bilayer cathode for stabilizing organic solar cells in air.

In chapter 2, we discussed materials, methods and characterization techniques used in this study. During our optimization processes we found that, for devices with cathodes fabricated in the bell-shape chamber, twice pre-annealing was indispensable to achieving a relatively high initial performances.

We found that among devices fabricated in one single batch, those stored in a dark box degraded relatively slowly than those stored under fluorescent lamps. The observed various degradation patterns summarized in Table 4 in Chapter 3 evidenced at least three processes in the photo-induced degradation of OSCs:

- Light independent extrinsic degradation;
- Light dependent reversible degradation;
- Short-wavelength light caused irreversible degradation.

We built several models to explain the various degradation curves of OSCs. One of the simplest but versatile models is based on the accelerated lateral diffusion of oxygen in the fullerene layer under light irradiation. When oxygen is considered as the major cause of the extrinsic degradation, intruding paths of oxygen from the aluminum layer should include not only microscopic pinholes, but also wide grain-boundaries. According to simulations, the light irradiation from fluorescent lamps increases the diffusion coefficient of oxygen in fullerene at least seven times.

To eliminate the intrusion of air from the cathode layer, we replaced the aluminum cathode with a novel titanium-aluminum bilayer cathode. Shelf lives of these bilayer-cathode devices are improved by at least three orders of magnitude compared to those of single-layer-cathode devices. Performances of these bilayer-cathode devices under weathering tests or in a high-humid ambience (RH > 90%) have also been probed. Both encapsulated and unencapsulated devices showed recoverable degradation under continuous irradiation. Finally, we probed the stabilization mechanisms behind the superior shelf stability of these bilayer-cathode devices. Based on investigations of

surface morphology and elemental depth profiles in different devices, we proposed the following stabilization roles played by the bilayer cathode:

- The titanium layer eliminates the microscopic pinholes in the cathode;
- The titanium layer hinders the interdiffusion of LiF and aluminum to organic layers;
- The aluminum layer improves the oxygen resistance of titanium, and the aluminum gets passivated in this process.

Besides, the titanium layer probably improves the water resistance of aluminum.

To conclude, we have studied the mechanisms and dynamics of the extrinsic degradation of small-molecular organic solar cells from various perspectives. To overcome the degradation, we have designed a bilayer cathode, which improves the shelf life of an unencapsulated OSC by at least three orders of magnitude. These findings will hopefully advance the understanding and development of organic solar cells.

References

[1] REN21, Renewables global status report (GSR) (2012)

[2] D. M. Chapin, C. S. Fuller, and G. L. Pearson, *J. Appl. Phys.*, 25, 676-677 (1954)

[3] C. F. Klingshirn: *Semiconductor Optics* (Springer Berlin Heidelberg, 2007) 3rd ed.

[4] M. A. Green, K. Emery, Y. Hishikawa, W. Warta, and E. D. Dunlop, *Prog. Photovoltaics*, 21, 1-11 (2013)

[5] D. C. Jordan and S. R. Kurtz, *Prog. Photovoltaics*, 21, 12-29 (2013)

[6] S. Momose, K. Yoshikawa, and D. Shuuichi: The 60th JSAP Spring Meeting, Kanagawa, Japan, 2013

[7] ASTM G173-03 Reference Spectra

[8] C. Kittel: *Introduction to Solid State Physics* (John Wiley & Sons, Inc., 2005) 8th ed.

[9] K. Seeger: *Semiconductor Physics* (Springer-Verlag Berlin Heidelberg, 2004) 9th ed., p. 37

[10] N. W. Ashcroft and N. D. Mermin: *Solid State Physics* (Harcourt College Publishers, US, 1976)

[11] T. Tsurumi, H. Hirayama, M. Vacha, and T. Taniyama: *Nanoscale Physics for Materials Science* (CRC Press, 2009), pp. 133–140

[12] G. Zhang, W. Li, B. Chu, L. Chen, F. Yan, J. Zhu, Y. Chen, and C. S. Lee, *Appl. Phys. Lett.*, 94, 143302 (2009)

[13] A. A. Bakulin, A. Rao, V. G. Pavelyev, P. H. M. van Loosdrecht, M. S. Pshenichnikov, D. Niedzialek, J. Cornil, D. Beljonne, and R. H. Friend, *Science*, 335, 1340-1344 (2012)

[14] C. F. Zhang, J. C. Zhang, Y. Hao, Z. H. Lin, and C. X. Zhu, *J. Appl. Phys.*, 110, 064504 (2011)

[15] L. G. De Arco, Y. Zhang, C. W. Schlenker, K. Ryu, M. E. Thompson, and C. W. Zhou, *Acs Nano*, 4, 2865-2873 (2010)

[16] J. H. Lambert, *Acta Helv. Phys. Math. Anat. Bot-Med.*, 3, 128 (1758)

[17] G. Yu, J. Gao, J. C. Hummelen, F. Wudl, and A. J. Heeger, *Science*, 270, 1789-1791 (1995)

[18] J. Xue, S. Uchida, B. P. Rand, and S. R. Forrest, *Appl. Phys. Lett.*, 84, 3013-3015 (2004)

[19] K. Ishibashi, Y. Kimura, and M. Niwano, *J. Appl. Phys.*, 103, 094507 (2008)

[20] A. Jain and A. Kapoor, *Sol. Energy Mater. Sol. Cells*, 81, 269-277 (2004)

[21] A. Jain and A. Kapoor, *Sol. Energy Mater. Sol. Cells*, 85, 391-396 (2005)

[22] J. C. Wang, X. C. Ren, S. Q. Shi, C. W. Leung, and P. K. L. Chan, *Org. Electron.*, 12, 880-885 (2011)

[23] P. Schilinsky, C. Waldauf, J. Hauch, and C. J. Brabec, *J. Appl. Phys.*, 95, 2816-2819 (2004)

[24] M. Grätzel, *Nature*, 414, 338-344 (2001)

[25] G. Chamberlain, *Solar Cells*, 8, 47-83 (1983)

[26] H. Spanggaard and F. C. Krebs, *Sol. Energy Mater. Sol. Cells*, 83, 125-146 (2004)

[27] A. Mishra and P. Bäuerle, *Angew. Chem. Int. Ed.*, 51, 2020-2067 (2012)

[28] F. Gutmann and L. E. Lyons: *Organic Semiconductors* (Wiley, New York, 1967), pp. 89, 105, 516, 595

[29] H. Meier and A. Haus, *Angew. Chem.*, 72, 631 (1960)

[30] K. Kudo and T. Moriizumi, *Jpn. J. Appl. Phys.*, 20, L553-L556 (1981)

[31] C. W. Tang, *Appl. Phys. Lett.*, 48, 183-185 (1986)

[32] M. G. Helander, Z. B. Wang, J. Qiu, M. T. Greiner, D. P. Puzzo, Z. W. Liu, and Z. H. Lu, *Science*, pp. 944–947 (2011)

[33] Y. Zhou, C. Fuentes-Hernandez, J. Shim, J. Meyer, A. J. Giordano, H. Li, P. Winget, T. Papadopoulos, H. Cheun, J. Kim, M. Fenoll, A. Dindar, W. Haske, E. Najafabadi, T. M. Khan, H. Sojoudi, S. Barlow, S. Graham, J.-L. Brédas, S. R. Marder, A. Kahn, and B. Kippelen, *Science*, 336, 327-332 (2012)

[34] Y. Zhou, H. Cheun, S. Choi, J. William J. Potscavage, C. Fuentes-Hernandez, and B. Kippelen, *Appl. Phys. Lett.*, 97, 153304 (2010)

[35] H. Jin, C. Tao, M. Velusamy, M. Aljada, Y. Zhang, M. Hambsch, P. L. Burn, and P. Meredith, *Adv. Mater.*, pp. 2572–2577 (2012)

[36] K.-S. Chen, J.-F. Salinas, H.-L. Yip, L. Huo, J. Hou, and A. K.-Y. Jen, *Energy Environ. Sci.*, 5, 9551-9557 (2012)

[37] M. W. Rowell, M. A. Topinka, M. McGehee, H.-J. Prall, G. Dennler, N. Sariciftci, L. Hu, and G. Gruner, *Appl. Phys. Lett.*, 88, 233506 (2006)

[38] Y. Xia and J. Ouyang, *ACS Appl. Mater. Interfaces*, 2, 474-483 (2010)

[39] G.-H. Kim, H.-K. Song, and J. Y. Kim, *Sol. Energy Mater. Sol. Cells*, 95, 1119-1122 (2011)

[40] M. Kröger, S. Hamwi, J. Meyer, T. Riedl, W. Kowalsky, and A. Kahn, *Org. Electron.*,

10, 932-938 (2009)

[41] R. D. JOHNSON, C. S. YANNONI, H. C. DORN, J. R. SALEM, and D. S. BETHUNE, *Science*, 255, 1235-1238 (1992)

[42] A. V. Hamza, J. Dykes, W. Mosley, L. Dinh, and M. Balooch, *Surf. Sci.*, 318, 368-378 (1994)

[43] A. K. Pandey, M. Aljada, M. Velusamy, P. L. Burn, and P. Meredith, *Adv. Mater.*, 24, 1055-1061 (2012)

[44] Z. T. Xie, W. H. Zhang, B. F. Ding, X. D. Gao, Y. T. You, Z. Y. Sun, X. M. Ding, and X. Y. Hou, *Appl. Phys. Lett.*, 94, 063302 (2009)

[45] R. C. Haddon, A. F. Hebard, M. J. Rosseinsky, D. W. Murphy, S. J. Duclos, K. B. Lyons, B. Miller, J. M. Rosamilia, R. M. Fleming, A. R. Kortan, S. H. Glarum, A. V. Makhija, A. J. Muller, R. H. Eick, S. M. Zahurak, R. Tycko, G. Dabbagh, and F. A. Thiel, *Nature*, 350, 320-322 (1991)

[46] C. Schmidt: in *Direct Encapsulation of OLED on CMOS*, eds. G. Gerlach and K.-J. Wolter (Springer Berlin / Heidelberg, 2012), Chap. 29 Direct Encapsulation of OLED on CMOS, pp. 586–589

[47] S. Karak, S. Pradhan, and A. Dhar, *Semicond. Sci. Technol.*, 26, 095020 (2011)

[48] M. C. Petty: *Molecular Electronics* (John Wiley & Sons, Ltd, 2007), Chap. 7. Thin Film Processing and Device Fabrication, pp. 241–285

[49] L. Schmidt-Mende, A. Fechtenkotter, K. Mullen, E. Moons, R. H. Friend, and J. D. MacKenzie, *Science*, 293, 1119-1122 (2001)

[50] R. Søndergaard, M. Helgesen, M. Jørgensen, and F. C. Krebs, *Adv. Energy Mater.*, 1, 68-71 (2011)

[51] D. L. Morel, A. K. Ghosh, T. Feng, E. L. Stogryn, P. E. Purwin, R. F. Shaw, and C. Fishman, *Appl. Phys. Lett.*, 32, 495-497 (1978)

[52] R. Lessmann, Z. Hong, S. Scholz, B. Maennig, M. K. Riede, and K. Leo, *Org. Electron.*, 11, 539-543 (2010)

[53] J. Wagner, M. Gruber, A. Hinderhofer, A. Wilke, B. Bröker, J. Frisch, P. Amsalem, A. Vollmer, A. Opitz, N. Koch, F. Schreiber, and W. Brütting, *Adv. Funct. Mater.*, 20, 4295-4303 (2010)

[54] A. J. Nozik, M. C. Beard, J. M. Luther, M. Law, R. J. Ellingson, and J. C. Johnson, *Chem. Rev.*, 110, 6873-6890 (2010)

[55] H. Najafov, B. Lee, Q. Zhou, L. C. Feldman, and V. Podzorov, *Nat. Mater.*, 9, 938-943 (2010)

[56] R. O. Loutfy and J. H. Sharp, *J. Chem. Phys.*, 71, 1211-1217 (1979)

[57] N. Minami, K. Sasaki, and K. Tsuda, *J. Appl. Phys.*, 54, 6764-6766 (1983)

[58] M. Hiramoto, H. Fujiwara, and M. Yokoyama, *Appl. Phys. Lett.*, 58, 1062-1064 (1991)

[59] N. S. Sariciftci, L. Smilowitz, A. J. Heeger, and F. Wudl, *Science*, 258, 1474-1476 (1992)

[60] N. Sariciftci, D. Braun, C. Zhang, V. Srdanov, A. Heeger, G. Stucky, and F. Wudl, *Appl. Phys. Lett.*, p. 585 (1993)

[61] J. C. Hummelen, B. W. Knight, F. LePeq, F. Wudl, J. Yao, and C. L. Wilkins, *J. Org. Chem.*, 60, 532-538 (1995)

[62] Y. He, H.-Y. Chen, J. Hou, and Y. Li, *J. Am. Chem. Soc.*, 132, 1377-1382 (2010)

[63] S. H. Park, A. Roy, S. Beaupre, S. Cho, N. Coates, J. S. Moon, D. Moses, M. Leclerc, K. Lee, and A. J. Heeger, *Nat. Photonics*, 3, 297-302 (2009)

[64] Y. Sun, G. C. Welch, W. L. Leong, C. J. Takacs, G. C. Bazan, and A. J. Heeger, *Nat. Mater.*, 11, 44-48 (2012)

[65] V. D. Mihailetchi, H. Xie, B. de Boer, L. J. A. Koster, and P. W. M. Blom, *Adv. Funct. Mater.*, 16, 699-708 (2006)

[66] G. Bottari, G. de la Torre, D. M. Guldi, and T. Torres, *Chem. Rev.*, 110, 6768-6816 (2010)

[67] W. Xie, Y. Zhao, J. Hou, and S. Liu, *Jpn. J. Appl. Phys.*, 42, 1466-1469 (2003)

[68] A. K. Ghosh and T. Feng, *J. Appl. Phys.*, 44, 2781-2788 (1973)

[69] A. W. Hains, Z. Liang, M. A. Woodhouse, and B. A. Gregg, *Chem. Rev.*, 110, 6689-6735 (2010)

[70] M. C. Scharber, D. Mühlbacher, M. Koppe, P. Denk, C. Waldauf, A. J. Heeger, and C. L. Brabec, *Adv. Mater.*, 18, 789-794 (2006)

[71] G. Chen, H. Sasabe, Z. Wang, X.-F. Wang, Z. Hong, Y. Yang, and J. Kido, *Adv. Mater.*, 24, 2768-2773 (2012)

[72] J. You, L. Dou, K. Yoshimura, T. Kato, K. Ohya, T. Moriarty, K. Emery, C.-C. Chen, J. Gao, G. Li, and Y. Yang, *Nat. Commun.*, 4, 1446 (2013)

[73] M. Jørgensen, K. Norrman, S. A. Gevorgyan, T. Tromholt, B. Andreasen, and F. C. Krebs, *Adv. Mater.*, 24, 580-612 (2012)

[74] M. O. Reese, S. A. Gevorgyan, M. Jørgensen, E. Bundgaard, S. R. Kurtz, D. S. Ginley, D. C. Olson, M. T. Lloyd, P. Morvillo, E. A. Katz, A. Elschner, O. Haillant, T. R. Currier, V. Shrotriya, M. Hermenau, M. Riede, K. R. Kirov, G. Trimmel, T. Rath, O. Inganäs, F. Zhang, M. Andersson, K. Tvingstedt, M. Lira-Cantu, D. Laird, C. McGuiness, S. J. Gowrisanker,

M. Pannone, M. Xiao, J. Hauch, R. Steim, D. M. DeLongchamp, R. Rösch, H. Hoppe, N. Espinosa, A. Urbina, G. Yaman-Uzunoglu, J.-B. Bonekamp, A. J. van Breemen, C. Girotto, E. Voroshazi, and F. C. Krebs, *Sol. Energy Mater. Sol. Cells*, 95, 1253-1267 (2011)

[75] D. E. Motaung, G. F. Malgas, and C. J. Arendse, *J. Mater. Sci.*, 46, 4942-4952 (2011)

[76] B. Ray and M. A. Alam, *Appl. Phys. Lett.*, 99, 0333031-0333033 (2011)

[77] S. O. Jeon and J. Y. Lee, *Sol. Energy Mater. Sol. Cells*, 101, 160-165 (2012)

[78] M. O. Reese, A. J. Morfa, M. S. White, N. Kopidakis, S. E. Shaheen, G. Rumbles, and D. S. Ginley, *Sol. Energy Mater. Sol. Cells*, 92, 746-752 (2008)

[79] H. Hoppe and N. S. Sariciftci, *J. Mater. Chem.*, 16, 45-61 (2006)

[80] M.-C. Chen, Y.-S. Chiou, J.-M. Chiu, A. Tedla, and Y. Tai, *J. Mater. Chem. A*, 1, 3680-3687 (2013)

[81] S. R. Ferreira, P. Lu, Y.-J. Lee, R. J. Davis, and J. W. P. Hsu, *J. Phys. Chem. C*, 115, 13471-13475 (2011)

[82] B. J. Worfolk, T. C. Hauger, K. D. Harris, D. A. Rider, J. A. M. Fordyce, S. Beaupré, M. Leclerc, and J. M. Buriak, *Adv. Energy Mater.*, 2, 361-368 (2012)

[83] J. You, C.-C. Chen, L. Dou, S. Murase, H.-S. Duan, S. A. Hawks, T. Xu, H. J. Son, L. Yu, G. Li, and Y. Yang, *Adv. Mater.*, 24, 5267-5272 (2012)

[84] F.-R. Fan and L. R. Faulkner, *J. Chem. Phys.*, 69, 3341-3349 (1978)

[85] M. Lira-Cantu, K. Norrman, J. W. Andreasen, and F. C. Krebs, *Chem. Mater.*, 18, 5684-5690 (2006)

[86] M. Wang, Q. Song, H. Wu, B. Ding, X. Gao, X. Sun, X. Ding, and X. Hou, *Org. Electron.*, 8, 445-449 (2007)

[87] B. Andreasen, D. M. Tanenbaum, M. Hermenau, E. Voroshazi, M. T. Lloyd, Y. Galagan, B. Zimmernann, S. Kudret, W. Maes, L. Lutsen, D. Vanderzande, U. Wuerfel, R. Andriessen, R. Roesch, H. Hoppe, G. Teran-Escobar, M. Lira-Cantu, A. Rivaton, G. Y. Uzunoglu, D. S. Germack, M. Hosel, H. F. Dam, M. Jorgensen, S. A. Gevorgyan, M. V. Madsen, E. Bundgaard, F. C. Krebs, and K. Norrman, *Phys. Chem. Chem. Phys.*, 14, 11780-11799 (2012)

[88] M. Wang, F. Xie, J. Du, Q. Tang, S. Zheng, Q. Miao, J. Chen, N. Zhao, and J. B. Xu, *Sol. Energy Mater. Sol. Cells*, 95, 3303-3310 (2011)

[89] M. H. Petersen, S. A. Gevorgyan, and F. C. Krebs, *Macromolecules*, 41, 8986-8994 (2008)

[90] K. Norrman, S. A. Gevorgyan, and F. C. Krebs, *ACS Appl. Mater. Interfaces*, 1, 102-112 (2009)

[91] M. Hermenau, M. Riede, K. Leo, S. A. Gevorgyan, F. C. Krebs, and K. Norrman, *Sol. Energy Mater. Sol. Cells*, 95, 1268-1277 (2011)

[92] M. Hermenau, S. Schubert, H. Klumbies, J. Fahlteich, L. Müller-Meskamp, K. Leo, and M. Riede, *Sol. Energy Mater. Sol. Cells*, 97, 102-108 (2012)

[93] J. U. Lee, J. W. Jung, J. W. Jo, and W. H. Jo, *J. Mater. Chem.*, 22, 24265-24283 (2012)

[94] C. C. Eloi, D. J. Robertson, A. Rao, P. Zhou, K.-A. Wang, and P. C. Eklund, *J. Mater. Res.*, 8, 3085-3089 (1993)

[95] K. Norrman and F. C. Krebs, *Sol. Energy Mater. Sol. Cells*, 90, 213-227 (2006)

[96] J. Fraxedas: *Molecular Organic Materials* (Cambridge University Press, UK, 2006)

[97] A. L. Thomas: *Phthalocyanine Research and Applications* (CRC Press, Florida, 1990)

[98] M. Hiramoto, H. Fujiwara, and M. Yokoyama, *J. Appl. Phys.*, 72, 3781-3787 (1992)

[99] K. Sakai and M. Hiramoto, *Mol. Cryst. Liq. Cryst.*, 491, 284-289 (2008)

[100] H. W. Kroto, J. R. Heath, S. C. O'Brien, R. F. Curl, and R. E. Smalley, *Nature*, 318, 162-163 (1985)

[101] M. Dresselhaus, G. Dresselhaus, and P. Eklund: *Science of Fullerenes and Carbon Nanotubes: Their Properties and Applications* (Academic Press, San Diego, CA, 1996)

[102] W. Krätschmer, K. Fostiropoulos, and D. R. Huffman, *Chem. Phys. Lett.*, 170, 167-170 (1990)

[103] D. S. Bethune, G. Meijer, W. C. Tang, H. J. Rosen, W. G. Golden, H. Seki, C. A. Brown, and M. S. de Vries, *Chem. Phys. Lett.*, 179, 181-186 (1991)

[104] S. Sapp, S. Luebben, Y. B. Losovyj, P. Jeppson, D. L. Schulz, and A. N. Caruso, *Appl. Phys. Lett.*, 88, 152107 (2006)

[105] C. J. Brabec, S. E. Shaheen, C. Winder, N. S. Sariciftci, and P. Denk, *Appl. Phys. Lett.*, 80, 1288-1290 (2002)

[106] R. Schlaf, B. A. Parkinson, P. A. Lee, K. W. Nebesny, G. Jabbour, B. Kippelen, N. Peyghambarian, and N. R. Armstrong, *J. Appl. Phys.*, 84, 6729-6736 (1998)

[107] J. Kim, J.-S. Kim, S.-W. Kwak, J.-S. Yu, Y. Jang, J. Jo, T.-M. Lee, and I. Kim, *Appl. Phys. Lett.*, 101, 213304 (2012)

[108] A. Dürr, F. Schreiber, M. Kelsch, H. Carstanjen, and H. Dosch, *Adv. Mater.*, 14, 961-963 (2002)

[109] S. Sellner, A. Gerlach, F. Schreiber, M. Kelsch, N. Kasper, H. Dosch, S. Meyer, J. Pflaum, M. Fischer, and B. Gompf, *Adv. Mater.*, 16, 1750-1753 (2004)

[110] R. Roesch, M. Seeland, M. Bärenklau, G. Gobsch, and H. Hoppe, *Sol. Energy Mater. Sol. Cells*, 111, 212-215 (2013)

[111] M. C. Petty: *Thin films Processing and device fabrication* (John Wiley & Sons, Ltd, 2007), pp. 241–287

[112] A. Liu, S. Zhao, S.-B. Rim, J. Wu, M. Könemann, P. Erk, and P. Peumans, *Adv. Mater.*, 20, 1065-1070 (2008)

[113] R. F. Salzman, J. Xue, B. P. Rand, A. Alexander, M. E. Thompson, and S. R. Forrest, *Org. Electron.*, 6, 242-246 (2005)

[114] H. J. Wagner, R. O. Loutfy, and C. K. Hsiao, *J. Mater. Sci.*, 17, 2781-2791 (1982)

[115] M. O. Reese, M. S. White, G. Rumbles, D. S. Ginley, and S. E. Shaheen, *Appl. Phys. Lett.*, 92, 053307 (2008)

[116] P. Peumans, S. Uchida, and S. R. Forrest, *Nature*, 425, 158-162 (2003)

[117] B. W. Guralnick, J. E. Seppala, and M. E. Mackay, *J. Polym. Sci. Part B Polym. Phys.*, 49, 772-780 (2011)

[118] J. William D. Callister: *Materials Science and Engineering: An Introduction Seventh Edition* (John Wiley & Sons, Inc., 2007)

[119] C. J. Brown, *J. Chem. Soc. A*, 0, 2488-2493 (1968)

[120] A. Hoshino, Y. Takenaka, and H. Miyaji, *Acta Crystallogr. Sect. B*, 59, 393-403 (2003)

[121] F. M. Smits, *The bell system technical journal*, 37, 711-718 (1958)

[122] A. Benninghoven, *Angew. Chem. Int. Ed. Engl.*, 33, 1023-1043 (1994)

[123] J. Brison, S. Muramoto, and D. G. Castner, *J. Phys. Chem. C*, 114, 5565-5573 (2010)

[124] T. Yamanari, T. Taima, J. Sakai, J. Tsukamoto, and Y. Yoshida, *Jpn. J. Appl. Phys.*, 49, 01AC02 (2010)

[125] S. Duclos, R. Haddon, S. Glarum, A. Hebard, and K. Lyons, *Solid State Commun.*, 80, 481-484 (1991)

[126] A. RAO, K. WANG, J. HOLDEN, Y. WANG, P. ZHOU, P. EKLUND, C. ELOI, and J. ROBERTSON, *J. Mater. Res.*, 8, 2277-2281 (1993)

[127] M. Jaime and M. Nuñez Regueiro, *Appl. Phys. A: Mater. Sci. Process.*, 60, 289-292 (1995)

[128] G. Kroll, P. Benning, Y. Chen, T. Ohno, J. Weaver, L. Chibante, and R. Smalley, *Chemical Physics Letters*, 181, 112-116 (1991)

[129] F. Padinger, T. Fromherz, P. Denk, C. J. Brabec, J. Zettner, T. Hierl, and N. S.

Sariciftci, *Synth. Met.*, 121, 1605-1606 (2001)

[130] M. Jorgensen, K. Norrman, and F. C. Krebs, *Sol. Energy Mater. Sol. Cells*, 92, 686-714 (2008)

[131] F. C. Krebs and K. Norrman, *Prog. Photovoltaics*, 15, 697-712 (2007)

[132] R. Taylor, J. P. Parsons, A. G. Avent, S. P. Rannard, T. J. Dennis, J. P. Hare, H. W. Kroto, and D. R. M. Walton, *Nature*, 351, 277-277 (1991)

[133] J. W. Arbogast, A. P. Darmanyan, C. S. Foote, F. N. Diederich, R. L. Whetten, Y. Rubin, M. M. Alvarez, and S. J. Anz, *J. Phys. Chem.*, 95, 11-12 (1991)

[134] C. Schweitzer and R. Schmidt, *Chem. Rev.*, 103, 1685-1758 (2003)

[135] X. Xi, W. J. Li, J. Q. Wu, J. J. Ji, Z. R. Shi, and G. H. Li, *Sol. Energy Mater. Sol. Cells*, 94, 2435-2441 (2010)

[136] F. C. Krebs, J. E. Carle, N. Cruys-Bagger, M. Andersen, M. R. Lilliedal, M. A. Hammond, and S. Hvidt, *Sol. Energy Mater. Sol. Cells*, 86, 499-516 (2005)

[137] V. Kazukauskas, A. Arlauskas, M. Pranaitis, R. Lessmann, M. Riede, and K. Leo, *Opt. Mater.*, 32, 1676-1680 (2010)

[138] B. C. Duck, B. Vaughan, N. Cooling, X. Zhou, J. L. Holdsworth, L. L. Wen, S. C. Rasmussen, P. C. Dastoor, and W. J. Belcher, *Sol. Energy Mater. Sol. Cells*, 114, 65-70 (2013)

[139] J. Crank: *The mathematics of diffusion 2nd edition* (Oxford University Press, 1975), pp. 2–4 and 87

[140] J. Grimblot and J. M. Eldridge, *J. Electrochem. Soc.*, 129, 2366-2368 (1982)

[141] B. Pevzner, A. Hebard, and M. Dresselhaus, *Phys. Rev. B*, 55, 16439-16449 (1997)

[142] H. Habuchi, S. Nitta, D. X. Han, and S. Nonomura, *J. Appl. Phys.*, 87, 8580-8588 (2000)

[143] E. A. Katz, D. Faiman, B. Mishori, Y. Shapira, A. I. Shames, S. Shtutina, and S. Goren, *J. Appl. Phys.*, 84, 3333-3337 (1998)

[144] C. H. Lee, G. Yu, B. Kraabel, D. Moses, and V. I. Srdanov, *Phys. Rev. B*, 49, 10572-10576 (1994)

[145] M. Tavakkoli, R. Ajeian, M. N. Badrabadi, S. S. Ardestani, S. M. H. Feiz, and K. E. Nasab, *Sol. Energy Mater. Sol. Cells*, 95, 1964-1969 (2011)

[146] H. Cao and K. Ishikawa, *Sol. Energy Mater. Sol. Cells*, 109, 215-219 (2013)

[147] S. Cho, K. Lee, and A. J. Heeger, *Adv. Mater.*, 21, 1941-1944 (2009)

[148] K. Lee, J. Y. Kim, S. H. Park, S. H. Kim, S. Cho, and A. J. Heeger, *Adv. Mater.*, 19,

2445-2449 (2007)

[149] J. Kim, S. Kim, H.-H. Lee, K. Lee, W. Ma, X. Gong, and A. Heeger, *Adv. Mater.*, 18, 572-576 (2006)

[150] H. Saarenpää, T. Niemi, A. Tukiainen, H. Lemmetyinen, and N. Tkachenko, *Sol. Energy Mater. Sol. Cells*, 94, 1379-1383 (2010)

[151] T. R. Ohno, Y. Chen, S. E. Harvey, G. H. Kroll, P. J. Benning, J. H. Weaver, L. P. F. Chibante, and R. E. Smalley, *Phys. Rev. B*, 47, 2389-2393 (1993)

[152] W. H. Wang and W. K. Wang, *J. Appl. Phys.*, 79, 149-152 (1996)

[153] Q. Sun, Q. Wang, P. Jena, and Y. Kawazoe, *J. Am. Chem. Soc.*, 127, 14582-14583 (2005)

[154] C. Leyens: in *Titanium and Titanium Alloys. Fundamentals and Applications*, eds. C. Leyens and M. Peters (Wiley-VCH, Weinheim, 2003), pp. 189, 199 and 213

[155] G. Lütjering and J. C. Williams: *Titanium* (Springer, Berlin, 2007) 2nd ed., pp. 45–46 and 51

[156] L. Dake and R. Lad, *Surf. Sci.*, 289, 297-306 (1993)

[157] B. Zimmermann, U. Würfel, and M. Niggemann, *Sol. Energy Mater. Sol. Cells*, 93, 491-496 (2009)

[158] N.-K. Persson, H. Arwin, and O. Inganas, *J. Appl. Phys.*, 97, 034503 (2005)

[159] L. A. A. Pettersson, L. S. Roman, and O. Inganas, *J. Appl. Phys.*, 86, 487-496 (1999)

[160] F. Monestier, J.-J. Simon, P. Torchio, L. Escoubas, B. Ratier, W. Hojeij, B. Lucas, A. Moliton, M. Cathelinaud, C. Defranoux, and F. Flory, *Appl. Opt.*, 47, C251-C256 (2008)

[161] Y. Sun, C. J. Takacs, S. R. Cowan, J. H. Seo, X. Gong, A. Roy, and A. J. Heeger, *Adv. Mater.*, 23, 2226-2230 (2011)

[162] T. Tromholt, A. Manor, E. A. Katz, and F. C. Krebs, *Nanotechnology*, 22, 225401 (2011)

[163] C. C. Chang, D. B. Fraser, M. J. Grieco, T. T. Sheng, S. E. Haszko, R. E. Kerwin, R. B. Marcus, and A. K. Sinha, *J. Electrochem. Soc.*, 125, 787-792 (1978)

[164] The realtime indoor RH in the lab was recorded and found to be 20% less than the outdoor RH. http://www.jma.go.jp/jma/indexe.html

[165] M. Easton and D. StJohn, *Metall. Mater. Trans. A*, 30, 1613-1623 (1999)

[166] M. Schmitz-Niederau and M. Schutze, *Oxid. Met.*, 52, 215, 241-276 (1999)

[167] M. M. Farahani, T. E. Turner, and J. J. Barnes, *J. Electrochem. Soc.*, 134, 2835-2845 (1987)

[168] M. Bounoughaz, E. Salhi, K. Benzine, E. Ghali, and F. Dalard, *J. Mater. Sci.*, 38, 1139-1145 (2003)

[169] F. King: *Aluminum and its alloys* (Ellis Horwood, Chichester [West Sussex], United Kingdom, 1987), p. 165

[170] R. Agarwala, S. Murarka, and M. Anand, *Acta Metall.*, 12, 871-874 (1964)

Appendix

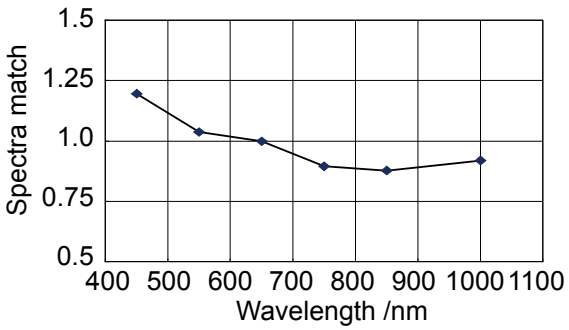

Supporting figure 1 Spectra difference between the simulated solar light from AM 1.5G. (Source: operation manual of HAL-C100 solar simulator)

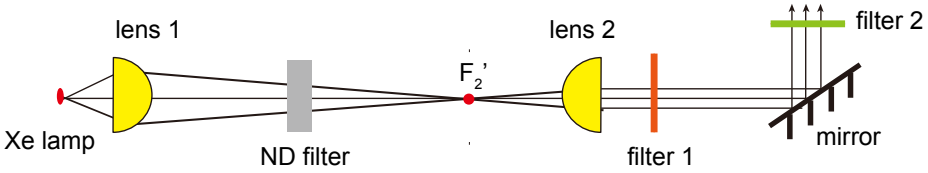

Supporting figure 2 Optical diagram of the Xe light source. The image of the Xe lamp formed by lens 1 was adjusted to the focus point of lens 2. Two IR-cutoff filters were used. The spectra are shown in Figure 2–21.

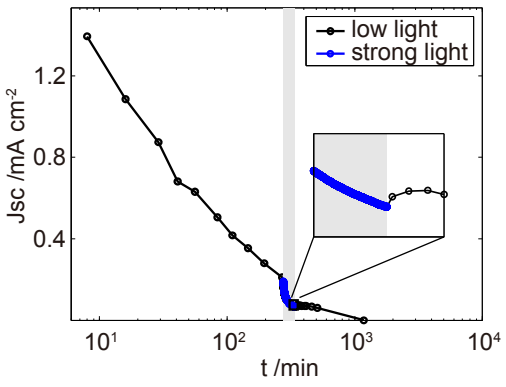

Supporting figure 3 Performance of an OSC-E experiencing a short period of continuous strong light irradiation (gray patch). The slight recovery zoomed in the inset resembles a simulation (blue curve on the right of Figure 4–4).

Publications

Cao, H., Tanaka M. & Ishikawa, K., Stabilization mechanisms of aluminum-titanium bilayer cathodes in organic solar cells. In preparation

Cao, H. & Ishikawa, K., Lateral oxygen diffusion dominated extrinsic degradation of small molecular organic solar cells, *Sol. Energy Mater. Sol. Cells*, 2013, 109, 215-219

Cao, H., Takezoe, H. & Ishikawa, K., Titanium–Aluminum Bilayer Cathode for Small-Molecular Organic Solar Cells with Prolonged Life upon Exposure to Air, *Jpn. J. Appl. Phys.,* 2013, 52, 040202

Academic talks

Huanqi Cao, Low light induced reversible degradation of unencapsulated small molecular organic solar cells. (oral) Tokyo Tech and KHU Joint Symposium on Advanced Display Materials, July 2012, Kyung Hee University, Yongin, Korea;

Huanqi Cao, Hideo Takezoe and Ken Ishikawa, Preventing the degradation of unencapsulated organic solar cells: self-encapsulated cathode. (oral) The 60th JSAP Spring Meeting, March 2013, Kanagawa, Japan;

Huanqi Cao and Ken Ishikawa, Accelerated degradation of organic solar cells: synergistic effect of oxygen and light. (poster), The 60th JSAP Spring Meeting, March 2013, Kanagawa, Japan.

Acknowledgements

First, I want to thank my supervisor Prof. Ken Ishikawa for making it possible for me to spend these precious three years at Tokyo Institute of Technology (Japan). It has been an honor to be his PhD student. I am extremely grateful to him for imparting me scholarly knowledge and how to communicate effectively with others. He has been actively interested in my work and has always been available to advise me. Whenever troubles appeared, I have consistently believed I would not be drowned in the science ocean, because I knew he was ahead of me like a lighthouse guiding me, even at the most self-doubt moments.

I also thank Prof. Hideo Takezoe, currently in Germany, for allowing me to join this laboratory and giving me instructive lectures on advanced science and technology, for offering me the chance to attend academic workshops, and for continuously urging me to find scientific originality.

I hope to express my great gratitude to Prof. Takehiko Mori, for introducing me to the laboratory three years ago and supplying the titanium material. I also hope to thank Prof. Martin Vacha for giving me enlightening lectures on organic optoelectronics.

Many thanks to Dr. Fumito Araoka, assistant professor, for imparting me plenty of useful experimental skills that substantially speeded up the research. I hope to thank Hiromi Takahashi for helping me deal with various application forms, saving a lot of research time.

I am particularly indebted to laboratory colleagues for assisting me in life and in study. The accomplishment of this thesis would have been much postponed without those people who taught me how to use and maintain laboratory equipment, optimized fabrication procedures and purified evaporation materials. Life in laboratory would have been much less interesting without many active lab fellows like Kazuhiro Isobe, Satoshi Aya and Masanori Yokoyama, et al.

Note that the deposition rate of aluminum using EB gun was optimized by Masaki Tanaka. Unlike other devices, the device used in Figure 2–24 was fabricated by Tomomi Ueno.

I also thank Prof. Masaaki Kakimoto for allowing me to use AFM. Dr. Akira Genseki measured TOF-SIMS. Xinhao Liu and Dr. Alexey Eremin introduced Matlab to me, using which I could have plotted these beautiful figures and simulated the models.

Many other Japanese people have also shared their love with me, consciously or unconsciously. I also appreciate friends from many other countries, especially these coming from my home country, with whom I have spent many beautiful days in Japan.

I express my very great appreciation to my family for their love and tacit encouragements.

Last but not least, I acknowledge the China Scholarship Council (CSC) for financially supporting my study in Japan. I also thank professors and faculty at Jilin University (China) for their amicable helps during the scholarship applications.

Huanqi Cao

August 2013